ALMA MATER STUDIORUM
UNIVERSITÀ DEGLI STUDI DI BOLOGNA

Dipartimento di Fisica e Astronomia

Dottorato di ricerca in Astronomia
Ciclo XXIX

Tesi di Dottorato

The origin and fate of the multiphase circumgalactic medium of disc galaxies using high-resolution hydrodynamical simulations

CANDIDATO:
Lucia Armillotta

RELATORE:
Prof. Filippo Fraternali

CO-RELATORE:
Dr. Federico Marinacci

COORDINATORE:
Prof. Francesco Rosario Ferraro

Esame finale anno 2016

Settore concorsuale: 02/C1 – Astronomia, Astrofisica, Fisica della Terra e dei Pianeti
Settore scientifico-disciplinare: FIS/05 – Astronomia e Astrofisica

Contents

Chapter 1

Introduction

In recent years, sensitive observations have revealed the presence of multiphase gas in the halo regions of low-redshift disc galaxies. This multiphase halo gas, also called *circumgalactic medium* (CGM), is explained by the existence of flows of gas towards and away from galaxies, showing a strong connection between discs of star-forming galaxies and their baryon-rich intergalactic surroundings. Thus, the study of the gaseous haloes is of fundamental importance to understand how galaxies evolve in their environment.

In this Introduction, we list the main observational properties of the gaseous haloes of nearby disc galaxies and of the Milky Way (Sec. 1.1) and we illustrate the main theoretical ideas concerning their origin (Sec. 1.2). Finally, in Sec. 1.3, we discuss the requirement of star-forming galaxies to accrete fresh gas to sustain their star formation at the current observed rates. Throughout this Thesis, we distinguish three different ranges of temperature:

- *cool gas*: gas at $T < 10^5$ K, both neutral and ionized (see Sec. 1.1.1 & 1.1.2);
- *warm gas*: gas at $10^5 \leq T \leq 10^6$ K (see Sec. 1.1.3);
- *hot gas*: gas at $T > 10^6$ K (see Sec. 1.1.4);

Hereafter, we use without distinction the terms *halo gas* and *circumgalactic medium*

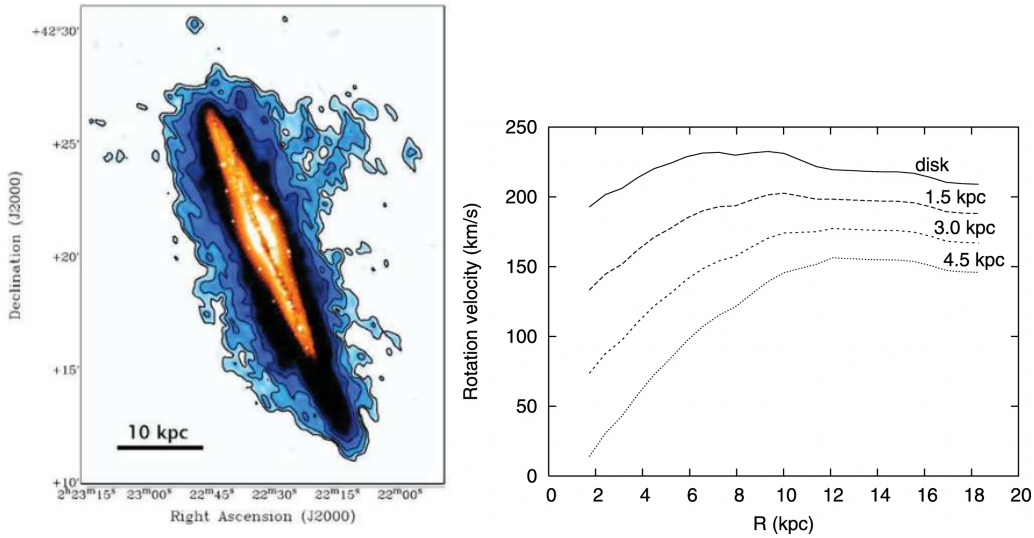

Figure 1.1: Extra-planar gas in the edge-on nearby galaxy NGC 891 (adapted from Oosterloo, Fraternali & Sancisi, 2007). *Left panel*: total HI map (blue) overlaid on the optical image (orange). Contours are at 0.1, 0.2, 0.5, 1×10^{20} cm^{-2} in HI column density. *Right panel*: HI rotation curves, the dotted/dashed lines show the rotation curves at different heights from the disc, while the solid line shows the rotation curve in the plane.

to refer to the gaseous environments surrounding low-redshift disc galaxies out to the virial radius ($\sim$ 230 kpc for the Milky Way). Instead, we use the term *extra-planar gas* to refer to gas close to the galactic disc (within a few kpc above it), mainly observed through HI and Hα emission.

1.1 Halo gas in disc galaxies

1.1.1 Cold neutral gas

The cold neutral phase is composed by gas at temperature $\lesssim 10^4$ K and it is mainly detected through the 21-cm emission line of the neutral hydrogen (HI). Thick layers of extra-planar neutral gas have been revealed around the Milky Way and several nearby spiral galaxies (Sancisi et al., 2008). HI observations of edge-on galaxies, where the halo emission can be easily separated from disc emission, have shown that $\sim 10 - 25$ % of the HI content associated to these galaxies is generally located at distances from a few to $\sim$ 10 kpc from the galactic plane (e.g. Swaters, Sancisi & van der Hulst, 1997; Matthews & Wood, 2003). Fig. 1.1 shows the HI emission map of the outstanding case of NGC 891. The extra-planar layer of this galaxy comprises $\sim$ 30% of the total HI mass (Oosterloo, Fraternali & Sancisi, 2007).

Overall, the extra-planar HI kinematics is quite regular: it rotates more slowly than the neutral gas component within the thin disc and its rotational velocity decreases with increasing height above the galactic plane. A vertical velocity gradient

of $\sim 15 - 30\,\mathrm{km\,s^{-1}\,kpc^{-1}}$ has been measured in a significant number of spiral galaxies, including the Milky Way (e.g. Fraternali et al., 2002; Heald et al., 2007; Oosterloo, Fraternali & Sancisi, 2007; Zschaechner et al., 2011). The right panel of Fig. 1.1 shows the HI rotation curves derived at different heights from the disc of NGC 891. The extra-planar HI also shows the presence of non-circular motions and in particular a possible large-scale radial inflow (Fraternali et al., 2001). Most of this gas is thought to be produced by the so-called 'galactic fountain', i.e. gas ejected from the disc by stellar feedback (Bregman, 1980; Houck & Bregman, 1990), that travels through the halo and eventually falls back to the disc in a time-scale of $\sim 80 - 100$ Myr.

In the Milky Way, deep and high-resolution observations has allowed to reveal extra-planar HI in the form of anomalous clouds, the so-called 'High-Velocity Clouds' (HVCs) (e.g. Muller, Oort & Raimond, 1963; Wakker, 1991; Wakker & van Woerden, 1997). HVCs are defined as HI clouds whose velocities in the local standard of rest deviate by more than $\sim 90\,\mathrm{km\,s^{-1}}$ from the speed predicted by a differentially rotating thin disc (Wakker, 1991). The top panel of Fig. 1.2 shows the all-sky map of the HVCs around the Milky Way. The extended structures indicate the high-velocity complexes. Each complex is composed by clouds of different sizes, related by the same spatial and kinematic proximity (Hsu et al., 2011; Putman, Peek & Joung, 2012). Beyond the largest HVCs, there is a large amount of small clouds called 'compact HVCs'. The sky at negative latitudes is dominated by the HVC Magellanic Stream (MS) and its leading arm (Complexes WE and WD in the top panel of Fig. 1.2). These structures originated from the interaction between two satellite dwarf galaxies, Large Magellanic Cloud (LMC, visible in Fig. 1.2) and Small Magellanic Cloud (SMC), and the Milky Way.

The knowledge of the distances of the HVCs is very important to derive their physical properties and, in particular, their masses. The best method to estimate the distance of a HVC is to use halo stars of known distances in the direction of the cloud and search for absorption lines at the velocity of the HVC in the star's spectrum. The presence or absence of absorption lines indicates that the cloud is in front of or behind the star. Recent works have revealed that the HVCs are located at typical distances $\lesssim 10$ kpc from the Sun (e.g Wakker et al., 2007; Thom et al., 2008), except the MS, situated in a range of distances of $\sim 50 - 200$ kpc (Putman, Peek & Joung, 2012). Their metallicities are subsolar, between 0.1 and 0.4 $\mathrm{Z_\odot}$ (Wakker, 2001), which supports the idea of an extragalactic origin for these clouds. The HI masses of the HVCs complexes are in the range of $10^5 - 5 \times 10^6\,\mathrm{M_\odot}$ (Putman, Peek & Joung, 2012), except for Complex C with a mass of $\sim 10^7\,\mathrm{M_\odot}$ (Wakker et al., 2007).

In nearby galaxies, HI halo clouds are very hard to detect in HI emission because of their low column densities. For instance, the typical HI column density, N_{HI}, in

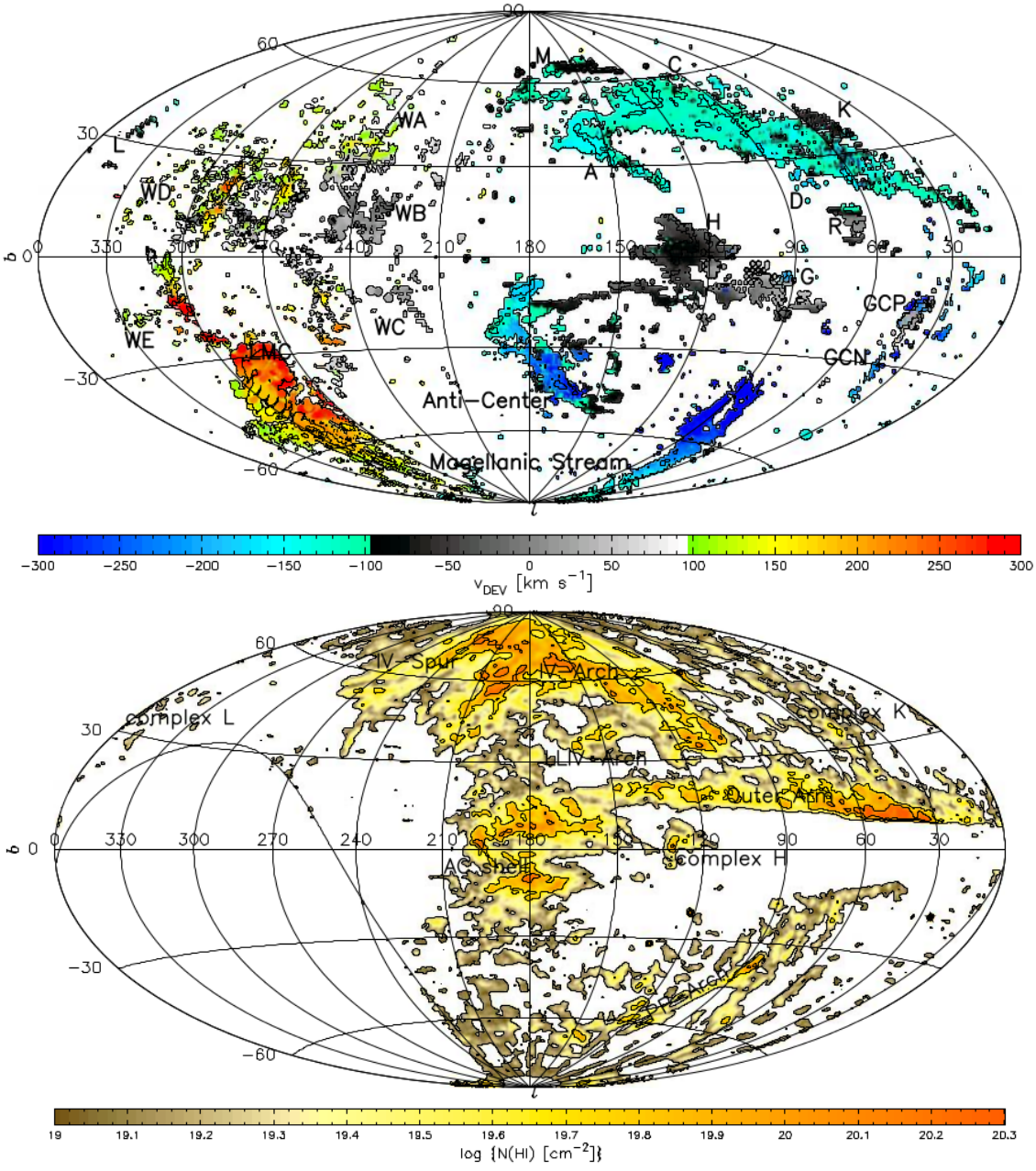

Figure 1.2: Aitoff projection all-sky map of the HVCs (*top panel*) and the IVCs (*bottom panel*) of the Milky Way (from van Woerden et al., 2004). *Top panel*: contours are at 2 and 20×10^{18} cm^{-2} in HI column density, while colors show deviation velocities, v_{DEV}, which is the difference between the observed velocity in the local standard of rest and the highest line-of-sight velocity predicted by a rotating disc model (Wakker, 1991). *Bottom panel*: contours are at 1, 5 and 12×10^{19} cm^{-2} in HI column density.

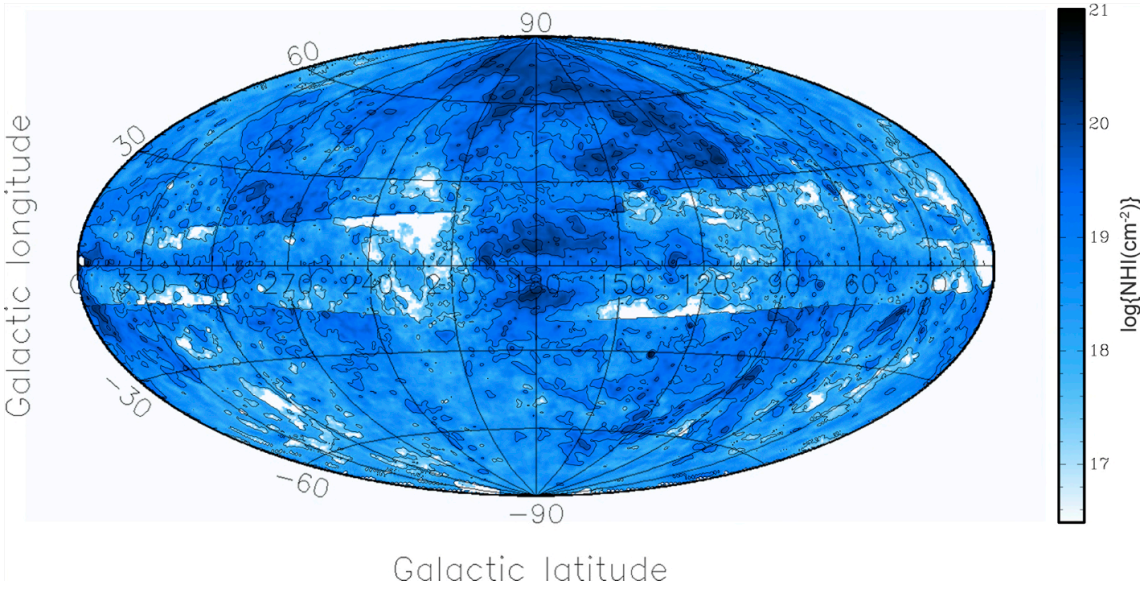

Figure 1.3: Aitoff projection all-sky map of the HI halo of the Milky Way including both HVCs and IVCs (from Marasco & Fraternali, 2011). This HI map was obtained from the LAB Survey after removing the disk emission, the Magellanic Clouds, the Magellanic Stream and the Outer Arm (HI warp of the Milky Way's disc). Contours are at 0.5, 10, 50 and 120×10^{18} cm^{-2} in HI column density.

the disc is $\sim 10^{21}$ cm^{-2}, while in the halo (extra-planar) region is $\sim 10^{19-20}$ cm^{-2}. High-resolution observations of nearby galaxies often have a sensitivity of $\sim 10^{20}$ cm^{-2}, which is close to the maximum HI column density of the Milky-Way's HVCs. However, two galaxies have been mapped out to column densities of $\sim 10^{18}$ cm^{-2}, they are M 31 (Thilker et al., 2004) and NGC 891 (Oosterloo, Fraternali & Sancisi, 2007). These galaxies show clouds with features similar to the HVCs in our Galaxy. In M 31, HI clouds are located out to distances $\gtrsim$ 50 kpc from the disc (Lewis et al., 2013), with masses that range from few times 10^4 to 6×10^5 M$_\odot$ (Westmeier, Braun & Thilker, 2005). However, most of them are likely associated with the tidal interaction between M 31 and its massive satellite galaxy M 33 (Westmeier, Brüns & Kerp, 2008).

In addition to the HVCs, in the Milky Way, HI observations have identified a population of cold clouds at the disc-halo interface, the so-called 'Intermediate-Velocity Clouds' (IVCs). They are distinguished from the HVCs both for their velocities, that, in the local standard of rest deviate by $35-90$ km s^{-1} from the speed predicted by a differentially rotating thin disc, and for their solar-like metallicity, probing a possible internal origin (Wakker, 2001; van Woerden et al., 2004). The IVCs are located within $\sim 1-2$ kpc from the Galactic disc, with masses in the range of $0.5 - 8 \times 10^5$ M$_\odot$ (Putman, Peek & Joung, 2012). The bottom panel of Fig. 1.2 shows an all-sky view of these clouds around the Milky Way. A large number of small and discrete HI clouds with mass of ~ 50 M$_\odot$ have been identified in the lower

halo of our Galaxy, between 4 and 8 kpc from the Galactic centre (Lockman, 2002; Ford, Lockman & McClure-Griffiths, 2010). These clouds extend to about 1 kpc above the disc and show kinematic features similar to the more massive IVCs (Saul et al., 2012).

Finally, Marasco & Fraternali (2011) showed that the IVCs and, to some extent the HVCs, are the local (Solar neighborhood) counterparts of a more diffuse medium that constitutes the extra-planar HI layer of the Milky Way. This layer is analogous to that found in external galaxies (see Fig. 1.1). To extract its properties, they used the Leiden-Argentine-Bonn HI survey (LAB, Kalberla et al., 2005) and kinematically separated the extra-planar emission from the disc emission, also excluding the MS. They found that the extra-planar HI covers the entire sky (see Fig. 1.3). Its total mass is of $\sim 3 \times 10^8$ $M_\odot$ (10% of the total HI mass) and it shows a vertical rotational gradient of ~ 15 km s^{-1} kpc^{-1}.

1.1.2 Cold ionized gas

Extra-planar cold ionized gas ($T \sim 10^{4-5}$ K) has been observed through Hα emission lines and absorption lines of low/intermediate ionization elements against background quasi-stellar objects (QSO).

Hα emission has been detected around several nearby edge-on spiral galaxies. This emission is usually concentrated in layers, called diffuse ionized gas (DIG) layers, extending up to ~ 5 kpc from disc (Hoopes, Walterbos & Rand, 1999; Collins & Rand, 2001). Several pieces of evidence indicate that these layers could be the ionized counterpart of the extra-planar HI. Their extent scales with the galaxy's SFR (Rossa & Dettmar, 2003), pointing to an internal origin of the extra-planar ionized gas. Moreover, the Hα kinematics is consistent with that of the extra-planar HI, showing both a rotation lag, with a vertical gradient of $\sim 15 - 25$ km s^{-1}, similar to that observed in HI (Heald et al., 2006, 2007), and non-circular motions (Fraternali, Oosterloo & Sancisi, 2004). Therefore, the DIG layers are likely the result of extra-planar HI photoionized by stellar radiation of the disc, and, as for the neutral phase, most of this gas could be produced by galactic fountains.

In the Milky Way, the Hα emission observed within $\sim 1 - 2$ kpc from the Galactic plane is known as the 'Reynolds' layer' (Reynolds, 1991). This gas can be considered the counterpart of the HI gas observed at the disc-halo interface in our Galaxy (see Sec. 1.1.1). Moreover, high-velocity Hα emission is also detected on top or near HI HVCs (Putman, Peek & Joung, 2012). In some cases, as the MS, simple photoionization by stellar radiation is not sufficient to explain the particularly bright Hα emission (e.g., Putman et al., 2003) that must be contributed by collisional ionization mechanisms, due to the interaction between HI clouds and the surrounding hot gas phase (e.g., Bland-Hawthorn et al., 2007).

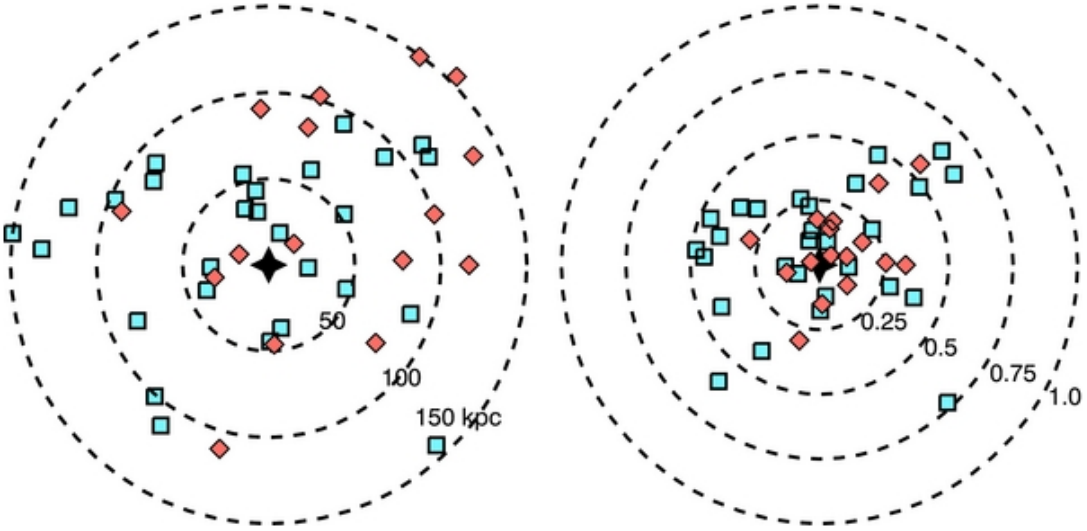

Figure 1.4: Distribution of Lyα absorptions on the sky with respect to the target galaxies (shifted to the center) (from Tumlinson et al., 2013). Star-forming galaxies are shown in blue, while passive galaxies are shown in red. *Left panel*: the radial coordinate is the physical distance projected on the sky (impact parameter) between each galaxy and its associated Lyα detection. *Right panel*: the radial coordinate is the ratio between the impact parameter and the virial radius of each galaxy, $R_{\rm vir}$.

Besides the DIG, galaxies appear to be surrounded by a much more extended cold ionized circumgalactic medium (CGM). Both in the Milky Way and in other spiral galaxies, absorption line observations have allowed to detect lower column densities but at similar temperatures as the Hα emission. In the Milky Way, absorption lines of different low/intermediate ionization elements (e.g. SiII, SiIII, CII, CIII, OI, MgII), probing weakly ionized material, show a covering fraction close to $70-90\%$ of the sky (Savage et al., 2003; Shull et al., 2009; Lehner et al., 2012). Some of these features are detected against halo stars showing that they are located within ~ 15 kpc from the Sun. In several cases, as for the Hα emission, they are the ionized component of the HI HVCs (e.g., Lehner & Howk, 2011).

Recently, the COS-Halos survey has constrained the physical properties of the CGM in nearby galaxies, both star-forming and passive, (Werk et al., 2012; Tumlinson et al., 2013), detecting gas through absorption lines against background QSO spectra for a sample of galaxies in the low-redshift ($0.1 < z < 0.35$) Universe. The picture that has emerged is that almost all galaxies, regardless of their morphological type, are surrounded by a cold and predominantly ionized gas component. Both Lyα absorbers and low/intermediate ionization elements (CII, CIII, MgII, SiII, SiIII) have shown strong column densities out to impact parameters of 150 kpc from the galaxies and, for the star-forming galaxies, a covering fraction close to 100 % (see Fig. 1.4, Tumlinson et al., 2013; Werk et al., 2013). Werk et al. (2013) estimated a total mass of cold gas (neutral + ionized) larger than 10^9 $M_\odot$ within 150 kpc (limit

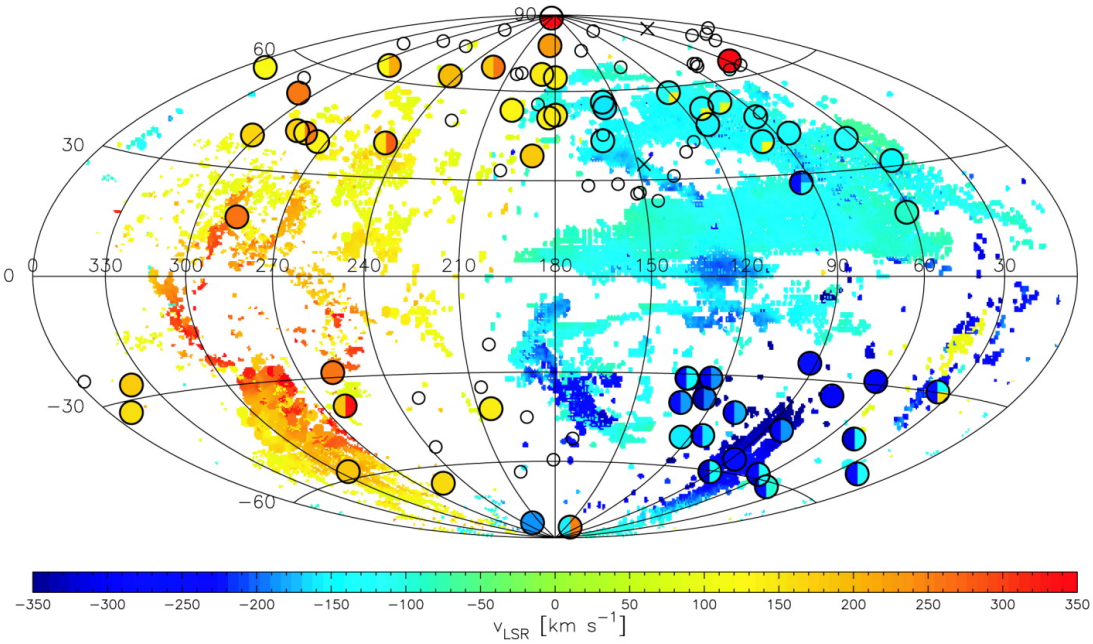

Figure 1.5: Milky Way: all-sky map of the high-velocity OVI absorptions (large filled circles) overlapping the distribution of the HI HVCs (from Sembach et al., 2003). The color of each circle indicates velocity on the same color scale used for the HI emission. If more than one OVI detection is present, the circle is split in more sections and the velocities are color-coded in each section of the circle. Small open circles indicate non-detections. The two crosses indicate the locations of two stellar sight lines in the sample.

of the survey) from galaxies. This value is approximately an order of magnitude higher than the mass estimated for cold gas in the Milky Way (estimated to be of the order of $10^8\,M_\odot$, Shull et al., 2009). This may be due to uncertainties in the distances - and then in the masses - of the Milky Way features.

1.1.3 Warm gas

In the low-redshift CGM, a warmer gas phase ($T \sim 10^{5-6}$ K) has been detected through OVI absorptions in QSO spectra. These features have a covering fraction of $\sim 70 - 80\,\%$ within 200-400 kpc from galaxies (Wakker & Savage, 2009; Prochaska et al., 2011). Tumlinson et al. (2011), through the COS-Halos survey, found that the amount of OVI around star-forming galaxies is larger than around galaxies with little or no star formation, suggesting that the lack of a warm gas halo could be related to the quenching of the star formation. As a consequence, only star-forming galaxies are surrounded by a large amount of both cold and warm gas (Tumlinson et al., 2011; Werk et al., 2013).

OVI absorbers have also been observed around the Milky Way. However, in our Galaxy constraining the distances of these absorbers is hard. Fig. 1.5 shows OVI

detections overlapping the HI map of the HVCs. It appears that the majority of the OVI absorptions are in the spatial and kinematic vicinity of the HI complexes. Two absorptions in Fig. 1.5 have been detected towards halo stars, indicating that they are located within $\sim$ 15 kpc from the Sun (e.g., Sembach et al., 2003). Overall, a covering fraction larger than 60% on the sky has been found for our Galaxy (Sembach et al., 2003). Ionization models (e.g. CLOUDY, Ferland et al., 1998), that reproduce the observed ionized gas for all lines of sight, found that, while low/intermediate ionization elements largely represent material photoionized by stellar radiation from the disc, high ionization elements represent collisionally ionized material, due to the interaction between cold clouds and the hot corona of the Milky Way (e.g. Sembach et al., 2003; Fox et al., 2010). Marasco, Marinacci & Fraternali (2013) reproduced the observational finding of most of the cold/warm absorbers around the Milky Way through a model in which both warm and cold absorbers mainly originate from the interaction between cold fountain clouds and the hot medium.

1.1.4 Hot gas

On the basis of a combination of Big Bang nucleosynthesis theory and observations of the cosmic microwave background, it has been found that galaxies are missing a large fraction of the baryons that should be associated to their dark matter halos. It is widely accepted that most of the warm-hot component of these missing baryons resides in the haloes around galaxies (e.g., Komatsu et al., 2009; Shull, Smith & Danforth, 2012). Thus, spiral galaxies, like our own Milky Way, should be embedded in hot gas atmospheres at virial temperature ($T \gtrsim 10^6$ K), the so-called 'coronae', extending out to hundreds of kpc from the galaxy centers (e.g., Fukugita & Peebles, 2006).

Unfortunately, the X-ray surface brightness of these coronae is close to the detection limit of the current generation of instruments (Bregman, 2007). As a consequence, to date, haloes of hot gas have only been observed around some massive spiral galaxies (see Fig. 1.6). In the giant spirals NGC 1961, NGC 6753, UGC 12591 and NGC 266, X-ray emission has been detected beyond 50 kpc from the center, indicating the presence of extended structures of hot gas (Dai et al., 2012; Bogdán et al., 2013; Anderson, Churazov & Bregman, 2016). The mass of these coronae is comparable with the disc baryonic mass ($\sim 10^{11}$ M$_\odot$), accounting for $10-50$% of the missing baryons associated to those galaxies. Recent estimates, obtained by combining observations of OVI absorbers around star-forming galaxies by the COS-Halos survey (see Sec. 1.1.3) with the OVII and OVIII absorptions associated with our Galaxy in a single model of corona, constrained the coronal gas mass of a Milky Way-like galaxy to $1-2\times10^{11}$ M$_\odot$ (Faerman, Sternberg & McKee, 2016). In agreement with theoretical expectations (see Sec. 1.2.1), the metallicity of these coronae is quite low, close to 0.1 Z$_\odot$ (Bogdán et al., 2013; Hodges-Kluck & Bregman, 2013).

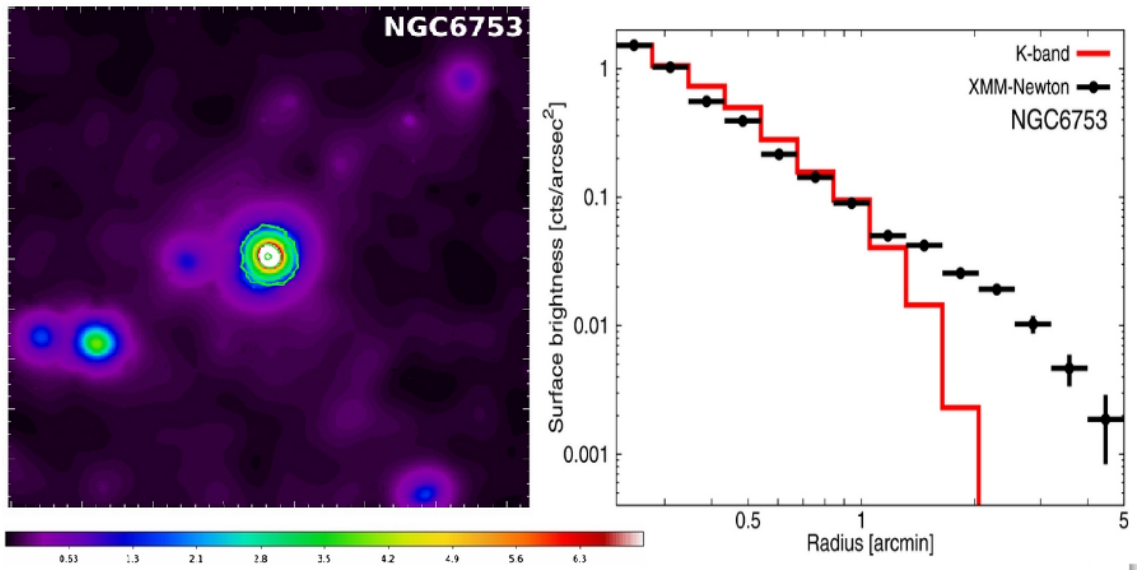

Figure 1.6: Hot corona in NGC 6753 (adapted from Bogdán et al., 2013). *Left panel*: X-ray surface brightness image based on the combined XMM-Newton EPIC data sets. The size length of the image is 10', which corresponds to 126.7 kpc at the distance of the galaxy. The image reveals large-scale extended emission surrounding the galaxy originating from the hot X-ray emitting gas. *Right panel*: X-ray surface brightness profile in the 0.3–2 keV band obtained from the combined data of XMM-Newton EPIC PN and EPIC MOS cameras. The K-band profile is also plotted, normalized to match the level of X-ray emission in the innermost bin. The excess of emission beyond $\sim$ 1.5 arcmin (20 kpc) cannot be produced by disc (stellar) emission.

In the Milky Way, the existence of a hot corona was originally hypothesized by Spitzer (1956) as the medium that provides pressure confinement to the High-Velocity Clouds. Most of the evidence that we have is indirect and comes from the head-tail structure of several HVCs (Putman, Saul & Mets, 2011), the rotation measure of pulsars in the Large Magellanic Cloud (Anderson & Bregman, 2010) and ram pressure stripping of dwarf galaxies in the Local Group (Grcevich & Putman, 2009; Gatto et al., 2013; Salem et al., 2015). Hot medium around the Galactic disc was detected and characterized through OVII and OVIII emission lines in the soft X-ray background and OVII and OVIII absorption lines in quasar spectra. The mass inferred from these detections is $\sim 4 \times 10^{10}\,M_\odot$ within 250 kpc, a value comparable with the disc stellar mass of our Galaxy, but $\sim$ 6 times smaller than the mass of the missing baryons associated with it (Miller & Bregman, 2015). The coronal metallicity of the Milky Way is not well constrained, but studies through both Far Ultraviolet absorption spectra and emission/absorption lines of OVII and OVIII estimate a value between 0.1 and 0.3 $Z_\odot$ (Sembach et al., 2003; Miller & Bregman, 2015).

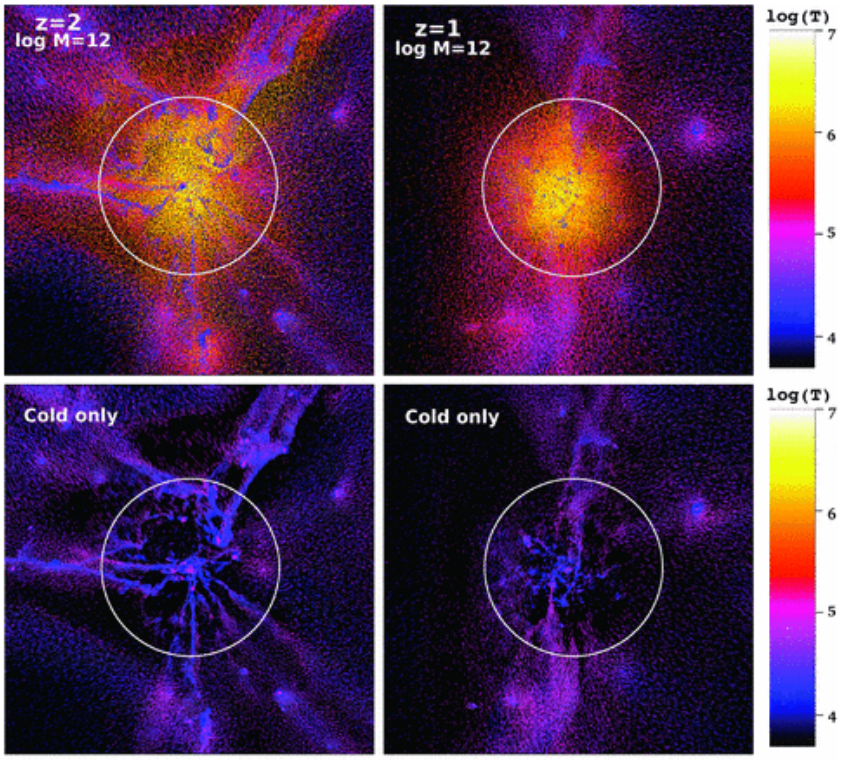

Figure 1.7: Temperature snapshots of a cosmological ΛCDM simulation of a Milky Way galaxy from (Kereš et al., 2009). The box region is 1 h^{-1} Mpc (comoving) on a side and 1 h^{-1} Mpc (comoving) in projected depth. *Left panels* show the galaxy at $z = 2$ ($M_{\rm vir} = 1.1 \times 10^{12}\,{\rm M}_{\odot}$), *right panels* show the galaxy at $z = 1$ ($M_{\rm vir} = 1.2 \times 10^{12}\,{\rm M}_{\odot}$). *Upper panels* show all the gas particles, *lower panels* show only the gas with $T < 10^5$ K but with the same colour scale (indicated on the right-hand side). The circles indicate the virial radius.

1.2 Origin of the halo gas

The origin of the multiphase halo gas is currently uncertain because the processes that regulate its formation and evolution are difficult to constrain both theoretically and observationally. Several scenarios have been proposed but the debate is still open. In the following section, we show the main processes that are currently thought to be at work.

1.2.1 Accretion from IGM

Classical models of galaxy formation predict that galaxies form from the collapse of overdense regions of matter: baryonic matter collapses in dark-matter potential wells and it is heated by continuous shocks until it forms an isotropic and spherical halo in hydrostatic equilibrium at virial temperature (White & Rees, 1978; White & Frenk, 1991).

Recently, cosmological ΛCDM simulations and analytic models have revised this classical picture. They showed that gas accretion from the IGM can occur in two modes: the *cold mode* accretion occurs through gas flows along overdense dark matter filaments that reach the central galaxy without being shock-heated to the virial temperature (see Fig. 1.7); in the *hot mode* accretion instead the gas is shock-heated to the virial temperature and forms a hot and rarefied corona around the galaxy (see Sec. 1.1.4) (e.g., Birnboim & Dekel, 2003; Dekel & Birnboim, 2006). *Cold mode* accretion is similar to what proposed by Binney (1977) and it is expected to dominate the global growth of all galaxies at high redshifts ($z \gtrsim 2$) and the growth of low-mass star-forming galaxies in the low-redshift Universe. Indeed, virial shocks can not form in low mass haloes because of the short cooling times of the gas. *Hot mode* accretion dominates the growth of galaxies with dynamical mass $M_{\rm vir} \gtrsim 2-3\times10^{11}\,{\rm M}_{\odot}$ or baryonic mass $M_{\rm bar} \gtrsim 2-3\times10^{10}\,{\rm M}_{\odot}$ at low redshift ($z<1$) (Kereš et al., 2009). As shown in Fig. 1.7, filamentary structures of *cold mode* accretion exist even above the threshold mass at $z=1$ and directly feed the central galaxy, but progressively decrease at lower redshifts. The transition redshift and the mass threshold are still uncertain and depend on the type of hydrodynamic solvers of the simulations (e.g., Nelson et al., 2013).

Accretion on the Milky Way, which has a virial mass of $M_{\rm vir}\sim2\times10^{12}\,{\rm M}_{\odot}$ (e.g., Li & White, 2008; Reid et al., 2009), is expected to be currently dominated by *hot mode* accretion. As a consequence, most of the accreted gas does not directly connect to the disc. Because of strong shocks, cold filaments dissipate their own kinetic energy and contribute to heating of the surrounding hot medium. Cosmological simulations of Milky Way-like galaxies find that the temperature of these filaments lies in the range of $10^{4.5-5.5}$ K (Joung et al., 2012). Observationally, these filamentary structures could be represented by the diffuse ionized gas, both cold and warm, detected through absorption lines of ions (see Sec. 1.1.2 and 1.1.3). The outer parts of the filaments are instead heated to higher temperatures, $T\gtrsim10^{6}$ K, becoming part of the hot and diffuse corona. The same simulations show that the densest parts of the *cold mode* filaments could survive the journey through the corona and infall on the disc (Fernández, Joung & Putman, 2012; Joung et al., 2012). Such filaments are currently not revealed in HI emission (see Sec. 1.1.1), although this may be due to the fact that these observations do not have enough sensitivity.

1.2.2 Satellite Accretion

Part of the multiphase halo surrounding spiral galaxies could be composed by gas lost from gas-rich dwarf galaxy satellites during their own motion through the host galaxy's corona (Putman et al., 2003; Grcevich & Putman, 2009). High-resolution N-body+SPH simulations show that dwarf galaxies lose their own gas mainly because of ram pressure stripping exerted by the coronal medium, although tidal stripping,

due to tidal force by the host galaxy, can also play an important role (Mayer et al., 2006). ΛCMD models predict that galaxies experience a small number a major mergers at high redshift, and an almost continuous infall of dwarf galaxies (e.g., Lacey & Cole, 1993). Indeed, ΛCMD simulations shows that 40% of Milky Way galaxies host a bright satellite ($L \sim 10^9 L_\odot$, e.g. LMC) within their virial radius and this result is consistent with the SDSS observations (Tollerud et al., 2011; Putman, Peek & Joung, 2012).

In the Milky Way's halo, the Magellanic System (Stream + Bridge) has been produced by tidal interaction between the two satellite galaxies LMC and SMC and their subsequent interaction with the Milky Way (see Sec. 1.1.1). The total gas mass of this complex is $\sim 2 \times 10^9\,\mathrm{M}_\odot$, of which 25% is composed by HI (more than $\sim 30-50\%$ of the HI mass of our Galaxy, Brüns et al., 2005), while 75% is composed by ionized gas, both cold and warm (Fox et al., 2014). During its own trip toward the galactic disc, a fraction of cold neutral gas stripped from satellites mixes with the hot medium creating warmer gas at intermediate temperatures. Observationally, this could explain the spatial and kinematic proximity between ion absorptions and the main HI complexes in the Milky Way (see Sec. 1.1.2 and 1.1.3).

1.2.3 Feedback

Central black holes and disc stars emit into the CGM a fraction of gas metal-enriched by stellar processes, respectively through AGN and stellar feedback (supernovae explosions and stellar winds). These processes can provide a significant amount of gas and energy in the haloes of galaxies.

Feedback driven by AGN or powerful starbursts can have triggered gas outflows in Milky Way-like galaxies at redshift $z > 1$. Recent cosmological simulations that study the nature and origin of CGM, incorporate these feedback prescriptions, needed to reproduce the number density of observed galaxies (e.g., Benson et al., 2003). They show that most of the observed cold/warm absorbers in the haloes of galaxies is due to gas that was ejected from galaxies through large-scale galactic outflows with velocity between 200 $\mathrm{km\,s^{-1}}$ and 1000 $\mathrm{km\,s^{-1}}$ (e.g., Stinson et al., 2012; Joung et al., 2012; Ford et al., 2013). In this range, higher-velocity gas escaped the galaxy's halo, while lower-velocity gas contributes to enrich the halo out to virial radii (see Sec. 1.1.2 and 1.1.3). This halo gas may eventually fall back onto the star-forming disc. The idea that powerful outflows ejected a large amount of material into the haloes of galaxies is confirmed by the recent findings that galaxies seem to be missing more than half of the metals that the disc stars have produced during their evolution (Zahid et al., 2012; Peeples et al., 2014). Galactic outflows have been effectively detected through multi-wavelength observations: they are composed by hot plasma at temperature of 10^{7-8} K observed in X-rays (well measured in M 82, e.g., Strickland & Heckman, 2007), ionized and neutral material observed at opti-

cal and near-UV wavelengths (e.g., Martin et al., 2012), and even molecular gas at temperature of 10^{1-3} K observed at radio wavelengths (e.g., Bolatto et al., 2013).

In Milky Way galaxies at low redshift, galactic fountains are the main feedback mechanism (Shapiro & Field, 1976; Bregman, 1980). Galactic fountains differ from large-scale galactic winds: they are driven by the blowout of superbubbles and affect the whole galactic disc, unlike AGN and starburst phenomena that occur in inner regions of galaxies. The classical theory predicts that galactic fountains are composed by ionized gas ($T \gtrsim 10^4$ K) travelling through the galactic halo out to a few kpc above the plane. This gas cools very quickly during its orbit and, given that its ejection velocity is typically much lower than the escape velocity from galaxy, falls back onto the disc in the form of cold dense clouds and filaments (e.g., Houck & Bregman, 1990; Melioli et al., 2008). As mentioned in Sec. 1.1.1, galactic fountains explain the origin of most of extra-planar gas at the disc-corona interface. In the Milky Way, the disc-like metallicity of the IVCs is consistent with a fountain origin. Moreover, the large population of small disc-halo clouds can be related to star-formation activity in the Galactic disc (Ford, Lockman & McClure-Griffiths, 2010). In Chapter 2, we show that the most prominent Galactic HVC, Complex C, can also originate from galactic fountain clouds ejected from the Milky Way's disc.

1.3 Gas accretion and feeding of star formation

A long standing problem in the evolution of star-forming galaxies like the Milky Way is how they keep accreting gas from the environment to feed their star formation. The star formation rate of these galaxies has mildly declined throughout their life times ($\sim$ 10 Gigayears) (e.g., Aumer & Binney, 2009; Fraternali & Tomassetti, 2012). In addition, it appears that HI content of these galaxies has remained approximately unchanged throughout the Hubble time (e.g., Bauermeister, Blitz & Ma, 2010; Zafar et al., 2013). Typically, the mass of gas contained in the thin disc can sustain the process of star formation only for one to a few gigayears (Kennicutt, 1983; Saintonge et al., 2013) and thus, at any given cosmic epoch, spiral galaxies need some supply of external gas to be brought into the disc, at a rate of $\sim 1\,\mathrm{M}_\odot\,\mathrm{yr}^{-1}$, to compensate the conversion of gas into stars (e.g., Sancisi et al., 2008). This gas needs to be metal poor in order to fulfill chemical evolution models of spiral galaxies (e.g., Pagel, 2009; Matteucci, 2012) and to explain the observed metallicity gradients (e.g., Cavichia et al., 2014; Pezzulli & Fraternali, 2016).

For decades, HVCs have been considered as good candidates for accreting cold and low-metallicity material onto the Milky Way, but the most recent estimates indicate that the accretion rate is merely $0.08\,\mathrm{M}_\odot\,\mathrm{yr}^{-1}$ (Putman, Peek & Joung, 2012), more than an order of magnitude lower than the Galactic star formation rate ($1-3\ \mathrm{M}_\odot\,\mathrm{yr}^{-1}$, Chomiuk & Povich, 2011). The situation does not change in nearby

galaxies where the amount of cold gas accretion from HVCs and minor mergers seems to account for at most $\sim$ 10% of the star formation requirement (Sancisi et al., 2008; Di Teodoro & Fraternali, 2014).

An alternative possibility is that gas accretion occurs mostly as ionized gas. As discussed in Sec. 1.1.2 and 1.1.3, the ionized gas phase extends beyond the HI dense component in the CGM. For the Milky Way, Shull et al. (2009) and Lehner & Howk (2011) estimated an accretion rate of ionized material onto the disc slightly lower respect to the star formation rate ($\lesssim 1\,M_\odot\,yr^{-1}$). However, these estimates are uncertain due to the unknown distances of most detections. Moreover, in order to be available for star-formation, ionized gas must survive its own trip through the coronal medium without being destroyed before reaching the star-forming disc. Several simulations of the survival of cold halo clouds moving in a hot medium were performed in the last years, showing that the survival timescales are relatively short ($\lesssim$ 100 Myr, e.g., Bland-Hawthorn et al., 2007; Heitsch & Putman, 2009; Kwak, Henley & Shelton, 2011). In Chapter 5, we explore the physical conditions that allow the survival of cold (ionized+neutral) gas in hot galactic coronae for hundreds of Myr.

As discussed in Sec. 1.1.4, cosmological coronae seem to contain a significant reservoir of gas that could be accreted by star-forming galaxies to sustain star formation at the current observed rates. However, the hot and rarefied gas needs to be cooled in order to make it available for star formation. Then, in this case, the accretion time is set by the cooling time of the gas shocked to the virial temperature. For a Milky Way galaxy, with $T_{\rm vir} = 2\times10^6$ K (e.g., Fukugita & Peebles, 2006; Miller & Bregman, 2015), the cooling time is $t_{\rm cool} \simeq (3k_{\rm B}T_{\rm vir})/(n_{\rm e}\Lambda(T_{\rm vir})) \sim 2.7$ Gyr, where $k_{\rm B}$ is the Boltzmann constant, $n_{\rm e} = 5.4\times10^{-4}$ cm^{-3} is roughly the coronal electronic density close to the disc (e.g., Anderson & Bregman, 2010) and $\Lambda(T_{\rm vir}) = 1.8\times10^{-23}$ erg cm^3 s^{-2} is the cooling rate at metallicity 0.1 $Z_\odot$. The spontaneous cooling time of a Milky Way corona appears very long and how gas cooling and accretion takes place in these hot coronae is still a matter of debate.

An hypothesis put forward to explain how the coronal gas might cool and collapse onto the disc was that the development of thermal instabilities in the corona could lead to the formation of cold clouds (Maller & Bullock, 2004; Kaufmann et al., 2006). However, later studies demonstrated that, in galaxies similar to the Milky Way, thermal instabilities are damped by the combined effect of heat conduction and buoyancy: cold clouds smaller than 10 kpc can form only farther than 100 kpc from the disc (Binney, Nipoti & Fraternali, 2009; Nipoti & Posti, 2013), in contradiction with the distances determined for HVCs ($\lesssim$ 10 kpc). Finally, both adaptive mesh refinement cosmological simulations of Milky Way-like galaxies and smoothed particle hydrodynamical simulations with an appropriate treatment of phase mixing show that spontaneous cooling through formation of thermal instabilities in the corona

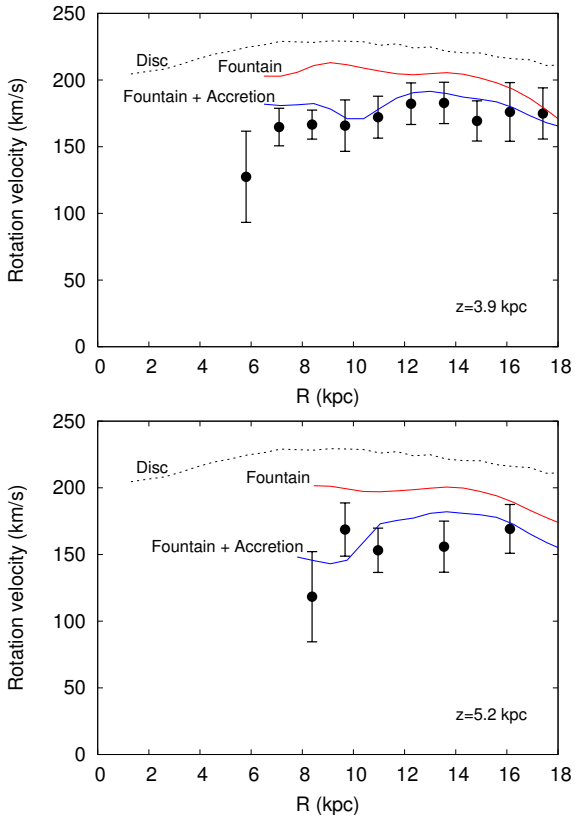

Figure 1.8: HI rotation curves of NGC 891 (points with error bars) at z = 3.9 kpc (*top panel*) and z = 5.2 kpc (*bottom panel*) above the plane. In both panels, the dotted line represents the rotation curve of the disc and it is shown to point out that the rotational velocity decreases with increasing distance from the plane. The red line shows the prediction of a simple ballistic fountain model (from Fraternali & Binney, 2006), the blue line indicates the prediction of the fountain model including accretion of gas from the corona (from Fraternali & Binney, 2008).

should not occur (Joung et al., 2012; Hobbs et al., 2013). As seen in Sec. 1.2.1, Fernández, Joung & Putman (2012) and Joung et al. (2012) found that non-linear perturbations, such as the *cold mode* filaments at $T \lesssim 10^{5.5}$ K, are needed to explain the formation of cold clouds in the hot corona. However, whether this cold gas coming from filaments can travel several tens of kpc without shattering remains unclear. Therefore, the question of how the galactic corona can cool and feed the star-forming disc is still open.

1.3.1 Disc-corona interface

As discussed in Sec. 1.1.1 and 1.2.3, most of the cold gas at disc-corona interface is thought to be composed by galactic fountain clouds, which orbit over the disc through the coronal medium.

Fraternali & Binney (2006) built a dynamical model of fountain clouds that follow ballistic trajectories into the galactic halo and applied it to the extra-planar HI observations of two nearby galaxies, NGC 891 and NGC 2403. This model is able to reproduce the observed HI vertical distribution of the extra-planar gas, but there are inconsistencies between the predicted and the observed kinematics. In particular, the model underestimates the vertical velocity gradient (see Sec. 1.1.1 for details): the observed HI rotational velocities are lower than the theoretical expectations. Fig. 1.8 illustrates the case of NGC 891. The two plots show the HI rotation curves (black points with error bars) at 3.9 kpc (left panel) and 5.2 kpc (right panel) above the plane. In both plots the dotted black line indicates the rotation curve in the plane, the red line shows the rotational velocity predicted by a simple ballistic fountain model, while the blue line shows the result of a fountain model that includes accretion of gas from the ambient medium (Fraternali & Binney, 2008). The latter model fits the data points very well, therefore, it appears that the extra-planar HI kinematics can be explained by assuming that the fountain clouds lose angular momentum by accreting material at lower rotational velocities from the ambient medium. The main free parameter in this model is the accretion rate of the clouds. Fraternali & Binney (2008) found that the global accretion rates required to reproduce the observed HI data-cubes of NGC 891 and NGC 2403 are very close to their respective current star formation rates. Therefore, accretion driven by galactic fountain clouds seems to be a viable mechanism for star-forming galaxies to get the right amount of gas needed to sustain star formation.

In order to investigate the physical phenomenon that drives the interaction between the hot corona and the cold fountain clouds, Marinacci et al. (2010, 2011) carried out 2D hydrodynamical simulations of a cold ($T = 10^4$ K) and disc-like metallicity cloud travelling through the hot ($T = 2 \times 10^6$ K) corona of the Milky Way. They found that the motion produces Kelvin-Helmholtz instabilities at the interface between the two fluids. The cold gas, stripped from the cloud, mixes efficiently in the turbulent wake behind the cloud. This mixing reduces dramatically the cooling time of the hot gas, triggering the condensation and the accretion of a fraction of coronal material onto the disc. Fig. 1.9 sketches this process. Moreover, the relative motion between the two fluids produces another important effect, that is the transfer of momentum between the cloud and the corona. The efficiency of momentum transfer strongly depends on their relative velocity. Marinacci et al. (2011) found that the hot corona stops absorbing momentum when the relative velocity between the cloud and the ambient medium drops below a threshold velocity $v_{\rm th} \simeq 75$ km s^{-1}. At lower velocities, condensation immediately regains the momentum given to the hot corona. This result suggests that the corona must rotate, but with a velocity lower than that of the disc. Indeed, only a lower velocity of the corona can explain the loss of angular momentum of the cold gas during the

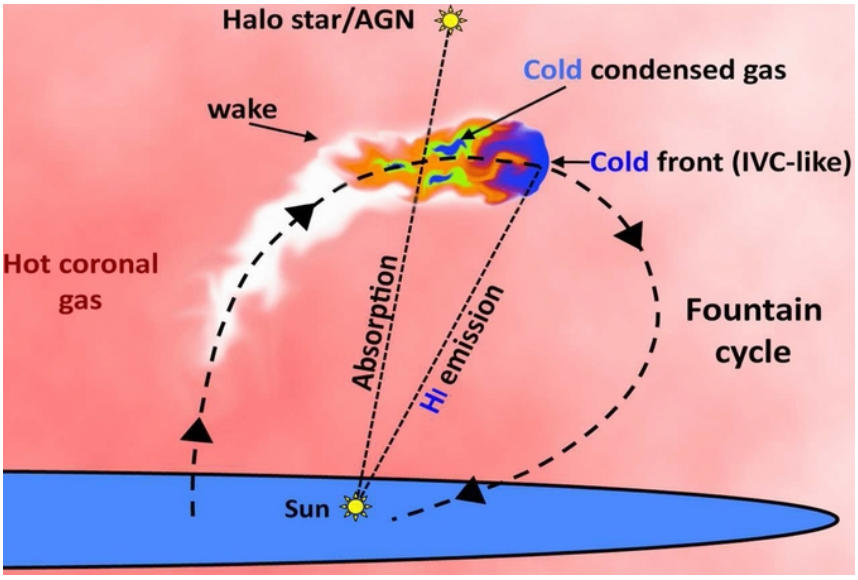

Figure 1.9: Schematic picture of a galactic fountain cloud (from Fraternali et al., 2013). Once ejected form the disc by stellar feedback, the cold and metal-rich cloud travels through the hot galactic corona and interacts with it. The interaction creates a turbulent wake behind the cloud where the hot and metal-poor coronal gas mixes with the cold gas stripped from the cloud. This mixing triggers the cooling of a portion of coronal material and produces a decrease of the cold gas angular momentum. An observer looking toward a background source intercepting the wake detects both HI emission and absorption lines of turbulent cold/warm ionized material. An observer looking toward the cold front detects HI emission.

coronal accretion phase and, then, the vertical velocity gradient measured for the extra-planar HI.

Marasco, Fraternali & Binney (2012) used the dynamical model of Fraternali & Binney (2008) to fit the kinematics of the extra-planar HI of the Milky Way. They found that the model reproduces the HI emission of the IVCs, thus confirming their disc origin, and provides a current accretion rate of coronal gas onto the disc of $\sim 2\ M_{\odot}\,yr^{-1}$, in agreement with the accretion required to sustain the star formation rate in the Milky Way. Marasco, Marinacci & Fraternali (2013) extended this model by including the results of hydrodynamical simulations to investigate whether the cold/warm absorption features, observed in the Milky Way's halo (see Sec. 1.1.2 & 1.1.3), are consistent with being produced by the coronal condensation in the turbulent wake behind the fountain clouds (see Fig. 1.9). The new model is able to reproduce positions and velocities of the most of the warm absorbers observed in the Galactic halo.

In conclusion, observations, dynamical models and hydrodynamical simulations suggest that accretion driven by galactic fountain clouds can be a viable mechanism for star-forming galaxies to sustain their star formation at the current observed rates.

This feedback-driven cooling of the galactic corona may have important implications for the evolution of star-forming galaxies, as we discuss in Chapter 4.

1.4 This thesis

In the previous sections, we have highlighted that the galactic haloes constitute a large reservoir of gas that plays an important role in the evolution of galaxies. The aim of this Thesis is to study, through high-resolution hydrodynamical simulations, the nature of these galactic haloes and, in particular, the physical phenomena driving the interaction and the mixing between the different gas phases. The final goal is to obtain a clearer picture of the interplay between galaxies and their surrounding environment.

In Chapter 2, we focus on the origin of Complex C, the most prominent HVC of the Milky Way, with very low metallicity. By combining a dynamical model of galactic fountain (Marasco, Fraternali & Binney, 2012) with high-resolution hydrodynamical simulations, we find that the Complex C was produced by the ejection of disc material that acted as a seed for cooling of a large portion of Galactic corona.

In Chapter 3, we describe the main numerical features of the ATHENA code (Stone et al., 2008), which we used to perform our hydrodynamical simulations presented in Chapters 4 and 5. To make ATHENA suitable for our purposes, we have modified it by introducing a more complete module for radiative cooling/heating that supports multiple gas metallicities and an algorithm for isotropic thermal conduction.

In Chapter 4, we widen the work done by Marinacci et al. (2010) (see Sec. 1.3.1). Until now, the interaction between the cold fountain clouds and the hot coronal medium had been studied only under conditions representative of our Milky Way. Here, we perform high-resolution hydrodynamical simulations of the cloud-corona interaction in haloes with different coronal temperatures, to probe a wide range of galaxy virial masses. These new simulations include the presence of thermal conduction, absent in the calculations performed so far.

In Chapter 5, we analyze under what physical conditions large amounts of cold gas can survive in the outer hot corona (see Sec. 1.1.2 and 1.1.3). We assume that the observed cold/warm ionized gas is associated with the interaction and mixing between the hot coronal medium and cold neutral gas.

Finally, a summary of the main results of this work is presented in Chapter 6.

Chapter 2

The origin of the High-Velocity Cloud Complex C[†]

2.1 Introduction

High-Velocity Clouds (HVCs) are cold gas complexes having velocities incompatible with their being part of the Galactic disc. Their origin has been a matter of debate for the last fifty years. Two competing scenarios have been proposed suggesting origins either external or internal to the Milky Way's disc (Wakker & van Woerden, 1997). The external origin was originally put forward by Oort (1970) who interpreted them as left-overs from the formation of our Galaxy. The internal hypothesis postulated that HVCs were clouds condensing in the Galactic halo from gas previously ejected from the disc by supernova explosions, through a galactic fountain (Bregman, 1980). In this latter case, the clouds should be at distances of a few kpc from the Galactic plane and have roughly the same metallicities as the disc material. The measurement of distances and metallicities of the HVCs became then crucial to distinguish between the two different scenarios.

Metallicities have been measured for most complexes and they have often been

[†]Some of the results of this Chapter have been published in Fraternali, Marasco, Armillotta, & Marinacci (2015).

found to be below the Solar value, typically between 0.1 and 0.4 Solar (e.g., Wakker, 2001). Moreover, recent works have found that most HVCs are generally located within about 10 kpc from the Galactic plane (Wakker et al., 2007; Thom et al., 2008). Overall, the relatively low metallicity was considered evidence for an extra-galactic origin although the actual source of the HVC material remained a mystery. Various mechanisms have been proposed such as thermal instabilities in the Galactic corona (Kaufmann et al., 2006), gas stripping from satellites (Olano, 2008) and gas condensation in cosmological filaments (Fernández, Joung & Putman, 2012).

Here, we focus on the most prominent and best studied of all HVCs, Complex C. Wakker et al. (1999), first, measured the metallicity of this HVC to be significantly below the Solar value, $Z \lesssim 0.1$ $Z_\odot$. This very low value allowed to interpret Complex C as metal-poor gas coming from the intergalactic medium and falling onto the Milky Way's disc. However, more recent works, based on observations along more than one line of sight (unlike Wakker et al., 1999), found that Complex C is not characterized by a single metallicity. Gibson et al. (2001) and Collins, Shull & Giroux (2003) measured the metallicity of Complex C to to lie in the range between 0.1 $Z_\odot$ and 0.45 $Z_\odot$, showing that some regions within this cloud are significantly contaminated by metal-enriched gas. These new measurements have suggested a new scenario, according to which Complex C is composed by a mixture of infalling metal-poor gas and metal-rich Galactic fountain material (Collins, Shull & Giroux, 2003). Moreover, the wide range of observed metallicities indicates that this mixture is not homogeneous but some regions within it are more well-mixed than others (Gibson et al., 2001).

Further evidence for a metal enrichment of Complex C by Galactic material comes from abundance ratios of different elements. The significant enrichment of α-elements (e.g. O, Si, S) relative to N and Fe suggests that the bulk of metals in Complex C were produced by massive stars and injected into the surrounding medium through Type II supernovae (Collins, Shull & Giroux, 2003). Moreover, Collins, Shull & Giroux (2007) found a dependence between metallicity and HI column density: lower metallicities along the line of sight correspond to higher HI column densities. According to those authors, this weak (2σ) anti-correlation could confirm the idea that Complex C originates from infalling extra-galactic gas that mixes with fountain material during its fall onto the Galactic disc. Indeed, mixing with metal-rich material should occur more efficiently in the outer and less dense regions of the complex, while the inner and denser regions remain intact and metal-poor.

In this Chapter, we combine the two competing scenarios concerning the formation of Complex C and present a new model, according to which Complex C was produced by the ejection of disc material, via supernova feedback, that has triggered the cooling of a large portion of hot coronal gas. In our model, contrary to the idea

of Collins, Shull & Giroux (2007), the seed of Complex C originates from the Galactic disc, not from infalling material. The Chapter is organized as follow. In Sec. 2.2 we introduce the approaches (dynamical model and high-resolution hydrodynamical simulations) used to model Complex C. In Sec. 2.3 we present the results of the model and their comparison with the observations. In Sec. 2.4 we discuss the initial conditions of the hydrodynamical simulations. In Sec. 2.5 we summarize the main results and discuss their implication for the evolution of the Milky Way.

2.2 Method

The method that we used to model the formation and evolution of Complex C consists of a combination of a dynamical model of galactic fountain and high-resolution hydrodynamical simulations of disc clouds travelling through the Galactic corona. Our aim was to explore the space of physical parameters that can reproduce the observed features of Complex C (e.g., position, velocity, distance and metallicity). Carrying out this work by using only hydrodynamical simulations is extremely expensive from a computational point of view. Therefore, the combination of high-resolution hydrodynamical simulations and a fountain dynamical model was the only viable approach.

2.2.1 Dynamical model

We used a galactic fountain model, in which gas clouds, ejected from the disc by stellar feedback, travel through the Galactic halo interacting and mixing with the the Galactic corona (see Marasco, Fraternali & Binney, 2012). As explained in Chapter 1, for typical conditions of the Milky Way disc-corona interface, this mixing dramatically reduces the cooling time of the corona causing its condensation into cloudlets that are then pulled down to the disc by gravity (Marinacci et al., 2010). A dynamical model of this kind produces an excellent fit to the all-sky extra-planar HI emission of the Milky Way (Marasco, Fraternali & Binney, 2012). A crucial modification that we made to this model is to assume that stellar feedback preferentially ejects material in the regions of the spiral arms. We adopted a four-arm spiral pattern model (Steiman-Cameron, Wolfire & Hollenbach, 2010) and an arm width (FWHM) of 1 kpc. We assumed a pattern speed of $25\,\mathrm{km\,s^{-1}}$ (Gerhard, 2011), which implies that the Sun is located roughly at the co-rotation radius, assuming $R = 8.5$ kpc and $v = 220\,\mathrm{km\,s^{-1}}$ (see Fig. 2.1).

In our dynamical model, the fountain clouds are ejected perpendicular to the disc with a given kick velocity and assumed to be co-rotating with the Galactic disc at the moment of the ejection. The orbits of the fountain clouds were integrated in a standard axi-symmetric Galactic potential (Model II in Binney & Tremaine, 2008),

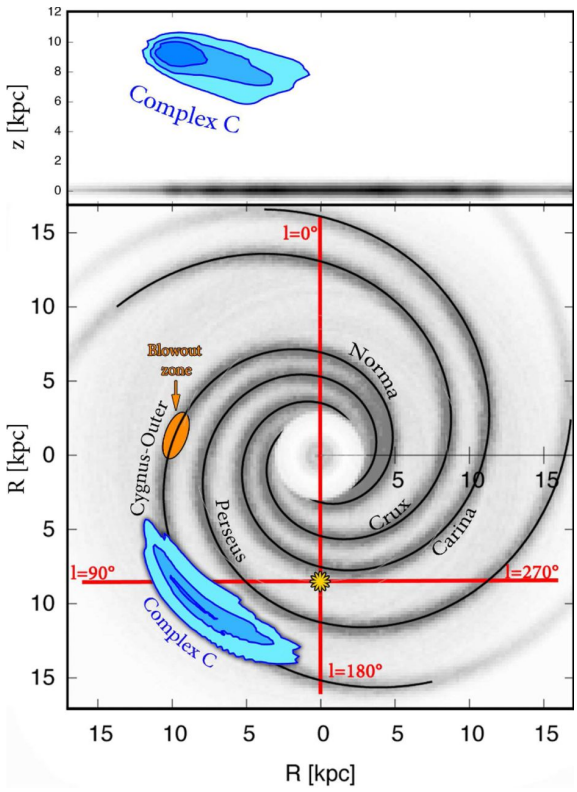

Figure 2.1: Two views of the HVC Complex C as resulting from our dynamical model (see text). *Top panel*: edge-on projection seen from the anticentre. *Bottom panel*: face-on view. The two panels are on the same scale. Contours are obtained from our galactic fountain model and correspond to HI column densities of 1, 2 and 3×10^{19} cm^{-2}. The spiral arms, the position of the Sun and the location of the ejection (orange ellipse) of the seed material are shown.

starting from initial conditions that can be varied to fit the data. In our model we also took into account two important hydrodynamical effects that can influence the ballistic orbit of the clouds: coronal ram pressure and condensation of coronal material (Marinacci et al., 2011).

The first effect can be parametrized by the drag time, $t_{\rm drag}$, time at which the relative velocity between cloud and corona, v, halves due to ram pressure exerted by the Galactic corona. The deceleration of the fountain cloud due to ram pressure can indeed be parametrized as (Fraternali & Binney, 2008):

$$\dot{\mathbf{v}}(R,z) = -\frac{v(R,z)^2}{v_0 t_{\rm drag}} \frac{\mathbf{v}(R,z)}{v(R,z)} , \tag{2.1}$$

where v_0 the ejection velocity of the cloud relative to the coronal gas. $v(R,z)$ is computed during the cloud's orbit at each time-step of the integration, assuming

that the rotation velocity of the corona is:

$$v_{\phi,\mathrm{cor}}(R,z) = \sqrt{R\frac{\partial\Phi(R,z)}{\partial R}} - v_{\mathrm{lag}} \,. \tag{2.2}$$

The first term on the right-hand-side of eq. 2.2 is the 'circular velocity' at R and z with $\Phi(R,z)$ potential of the Galaxy, while $v_{\mathrm{lag}} = 75\,\mathrm{km\,s^{-1}}$ is the rotation velocity of the corona around the Galactic centre relative to the local circular velocity (Marinacci et al., 2011). Finally, in eq. 2.1:

$$t_{\mathrm{drag}} = \frac{M_{\mathrm{cl}}}{v_0 \pi R_{\mathrm{cl}}^2 \rho_{\mathrm{cor}}} \,, \tag{2.3}$$

with $\rho_{\mathrm{cor}} \sim 10^{-27}$ g/cm^{-3} the coronal density and R_{cl} the cloud radius, obtainable from the mass cloud, M_{cl}, by imposing pressure equilibrium between cloud and corona (see Sec. 2.2.2 for details). We fixed the drag time by making assumptions on the initial mass. We supposed that Complex C is made up of tens of clouds with masses of $\sim 10^5\,\mathrm{M}_\odot$ that are shredded and disrupted by turbulence during their motion giving rise to the observed power-law mass function (Hsu et al., 2011), and estimated a drag time of ~ 380 Myr. However, we found that different initial masses and thus different drag times yield very similar final results. Indeed, the drag time has only a weak dependence on the cloud mass ($t_{\mathrm{drag}} \propto M_{\mathrm{cl}}^{1/3}$).

The second hydrodynamical effect present in our model is condensation of coronal material. This condensation occurs in the cloud's turbulent wake (see Fig. 2.3) and it has a non-negligible effect in the kinematics of the cold phase. Indeed, the slower rotational speed of the cold coronal gas with respect to the cloud involves an overall decrease of the rotational velocity of the cold gas. The deceleration of the cold gas was modelled as (Fraternali & Binney, 2008):

$$\dot{\mathbf{v}}(R,z) = -\frac{\dot{M}_{\mathrm{cold}}(t)}{M_{\mathrm{cold}}(t)}\, v(R,z)\, \frac{\mathbf{v}(R,z)}{v(R,z)} \,, \tag{2.4}$$

with

$$M_{\mathrm{cold}}(t) = \alpha(t)\, M_{\mathrm{cold}}(t=0) \,, \tag{2.5}$$

where $\alpha(t)$ is a time-dependent function, describing the evolution of the cold gas mass M_{cold} with time. In eq. 2.5, cold gas means both fountain gas and gas condensed out from the corona through cooling in the cloud's wake. We used a ninth grade polynomial as functional form of $\alpha(t)$. The polynomial coefficients were obtained by fitting the results of the hydrodynamical simulation (see Sec. 2.2.2).

The dynamical model contains six free parameters: the initial velocity of the ejection, the location along the spiral arm, the size of the ejection zone, the look-back time, the duration of the ejection process and the 'delay time', a parameter

$T_{\rm cor}$ (K)	$n_{\rm cor}$ ($\rm cm^{-3}$)	$Z_{\rm cor}$ ($\rm Z_\odot$)	$T_{\rm cl}$ (K)	$n_{\rm cl}$ ($\rm cm^{-3}$)	$Z_{\rm cl}$ ($\rm Z_\odot$)	$M_{\rm cl}$ ($\rm M_\odot$)	$v_{\rm cl}$ ($\rm km\,s^{-1}$)
2×10^6	10^{-3}	0.1	10^4	0.2	0.8	10^5	180

Table 2.2: Initial parameters of our fiducial simulation: coronal temperature $T_{\rm cor}$, coronal density $n_{\rm cor}$, coronal metallicity $Z_{\rm cor}$, cloud temperature $T_{\rm cl}$, cloud density $n_{\rm cl}$, cloud metallicity $Z_{\rm cl}$, initial cloud mass $M_{\rm cl}$ and initial cloud velocity $v_{\rm cl}$.

related to condensation, better explained in Sec. 2.2.2. The main observational constraint of our model is the LAB 21-cm all-sky survey of the Milky Way (Kalberla et al., 2005), which provides detailed information about HI column densities as a function of position in the sky and velocity along the line of sight. A mask of Complex C was created by isolating its HI emission channel by channel in the velocity range $-200 < v_{\rm Hel} < -75\,\rm km\,s^{-1}$ (Fig. 2.4, blue shading). The output of our fountain model is a mock observation in the form of a pseudo-datacube containing the simulated HI emission from fountain clouds for different choices of our six free parameters. The fit to the observations was performed in two steps: at first, we used a downhill simplex method to find the best-fit values; then, we ran a Monte Carlo Markov Chain (MCMC) to estimate the error-bars on our parameters.

2.2.2 Hydrodynamical simulation

To determine the condensation properties of the coronal gas we ran a series of hydrodynamical simulations of fountain clouds travelling through the Galactic corona. The resolution required to accurately characterize the condensation process is 2×2 pc (Marinacci et al., 2010), thus we could not simulate the whole Galactic disc.

All simulations were performed in a two-dimensional cartesian geometry with the ECHO++ code, which uses a fixed, non-adaptive grid with an higher upwind integration scheme. This code is based on the algorithm design of the ECHO (Eulerian Conservative High Order) code originally developed by Del Zanna et al. (2007), translated into C++ by Marinacci (PhD thesis, 2011), to which we refer for a full description. In this Section, we only show our fiducial simulation, used to describe the evolution of the cold gas mass in the dynamical model. In Sec. 2.4, we discuss why we chose such a simulation as fiducial simulation of our problem.

The parameters that set the initial conditions of the simulation are listed in Tab. 2.2. We considered a cold ($T_{\rm cl} = 10^4$ K) cloud travelling through a hot medium with an initial velocity $v_{\rm cl} = 180\,\rm km\,s^{-1}$. The coronal temperature is $T_{\rm cor} = 2 \times 10^6$ K, roughly the coronal temperature of the Milky Way (Fukugita & Peebles, 2006; Miller & Bregman, 2015), while the coronal metallicity is $Z_{\rm cor} = 0.1\ \rm Z_\odot$, according to the values estimated by X-ray observations of hot halos around external spiral galaxies (Hodges-Kluck & Bregman, 2013; Bogdán et al., 2013). Gravitational acceleration

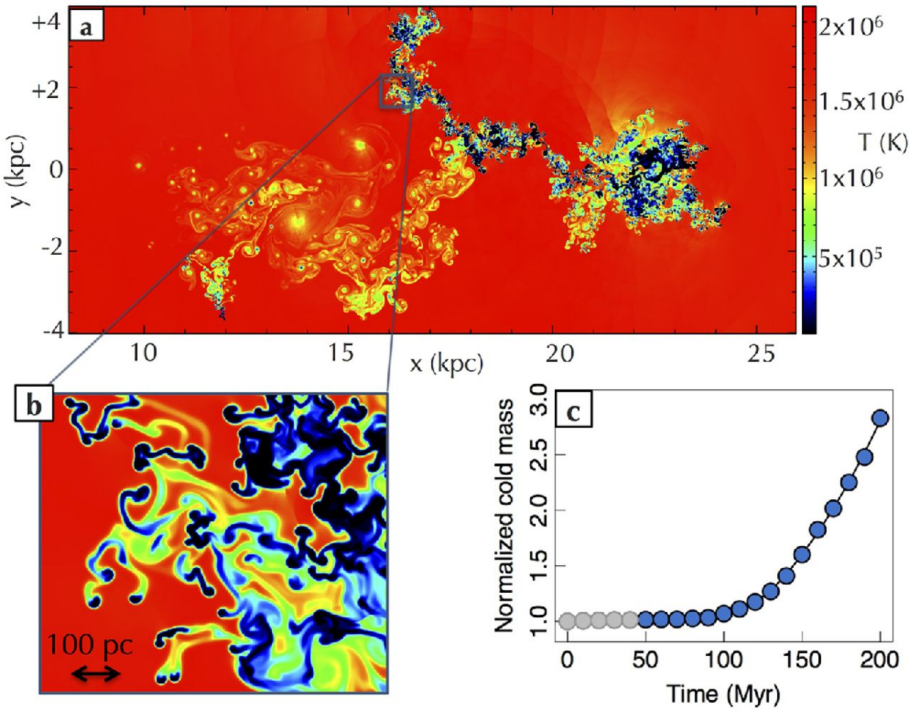

Figure 2.3: Hydrodynamical simulations of a galactic fountain cloud travelling through the Galactic corona. The simulation starts (at $x = 0$) as a round cloud at nearly solar metallicity, moving from left to right with respect to the hot metal-poor gas of the Galactic corona. (a) Temperature map after 175 Myr; the cold (blue) gas in the upper snapshot is made up both by cloud gas and by gas condensing from the corona, see close-up (b). (c) Mass of cold ($T < 10^{4.2}$ K) gas as a function of time normalized to the initial mass of the cloud; the condensation curve (blue line) was obtained by fitting a ninth grade polynomial to the points; the evolution before $t_{\rm delay} = 46$ Myr is determined by the unrealistic initial configuration of the cloud and has been excluded (see text).

and subsequent coronal density variation were neglected, thus we used a uniform density through the whole computational grid. The total number density of the coronal gas was fixed to $n_{\rm cor} = 10^{-3}$ cm^{-3}, in agreement with the average electron density $\langle n_{\rm e} \rangle = 5 \times 10^{-4}$ cm^{-3} within 50 kpc from the Galactic disc (Anderson & Bregman, 2011). The cloud number density ($n_{\rm cl} = 0.2$ cm^{-3}) was obtained by imposing pressure equilibrium between cloud and corona. Finally, we adopted a near-solar cloud metallicity, $Z_{\rm cl} = 0.8$ Z$_\odot$, which is typical metallicity of the Galactic ISM at $R \sim 9-10$ kpc (Esteban et al., 2013), where $9-10$ kpc indicates the Galactic radius of the ejection region, as obtained from the dynamical model (see Sec. 2.3). In Sec. 2.2.1, we said that our dynamical model assumes that Complex C is made up of tens of clouds with masses of $\sim 10^5$ M$_\odot$. In this simulation, we only considered a single cloud with mass $M_{\rm cl} = 10^5$ M$_\odot$.

The simulation ran for 200 Myr during which the cloud is torn apart by Kelvin-Helmhotz instabilities and produces a long turbulent wake where disc and coronal

material mix efficiently. In Fig. 2.3-a, we show a temperature snapshot after 175 Myr. The hot and metal-poor gas of the Milky Way's corona would normally have a cooling time exceeding 2 Gyr. However, the mixing between cold and metal-rich material reduces this time by orders of magnitude and condensation occurs in the cloud's wake (see cold knots in Fig. 2.3-b). Fig. 2.3-c shows the evolution of the cold gas at $T < 10^{4.2}$ K normalized to the initial cloud mass with time: the cold gas mass increases with time because more and more coronal gas cools down in the turbulent wake. After 200 Myr the amount of condensation is more than twice the initial mass of the cloud. We fitted a ninth grade polynomial, $\alpha(t)$ (see eq. 2.1), to the points of Fig. 2.3-c and used this condensation curve to describe the accretion from the corona in the clouds of our galactic fountain model. Since our dynamical model aims to reproduce the HI emission of Complex C, we considered only gas at $T < 10^{4.2}$ K in our simulation, indeed at $T > 10^{4.2}$ K the abundance of HI with respect to the total hydrogen is less than 50% under the assumption of collisional ionization equilibrium (CIE, Sutherland & Dopita, 1993). Condition of CIE was also assumed to calculate the gas radiative cooling during the simulation. The values of cooling rates were taken from Sutherland & Dopita (1993) (see also Sec. 3.4.1).

Our simulation starts from the unrealistic configuration of a round cloud, which limits the contact surface between cloud and corona and slows down their interaction. We introduced a delay time, $t_{\rm delay}$, that allows us to exclude the initial few tens of Myr of the simulation (Marasco, Fraternali & Binney, 2012). After this time, the cold gas, stripped from the cloud, mixes efficiently with the coronal gas and the condensation process can start. Therefore, the starting time of our dynamical model corresponds to $t = t_{\rm delay}$ in the simulation. We point out that the mass of cold gas increases with time (monotonic trend as a function of time), then, the larger is $t_{\rm delay}$, the larger is the amount of cold coronal gas accreted by the fountain cloud. We used $t_{\rm delay}$ to parametrize the effect of condensation in the dynamical model. The parameter $t_{\rm delay}$ is fitted to the data along with the other five parameters of the dynamical model (see Sec. 2.2.1). In this way, we could incorporate into the dynamical model the exact trend of the condensation in the simulation instead of using a simplified function as done in Marasco, Fraternali & Binney (2012).

2.3 Results

In this Section we present the results of our dynamical fountain model, in which we included the parametrization of the temporal evolution of the cold gas mass inferred by our fiducial simulation. In the dynamical model, for each set of parameters we build a mock HI data-cube that can be directly compared with the HI data of Complex C.

We found that Complex C was produced by a superbubble blowout occurred

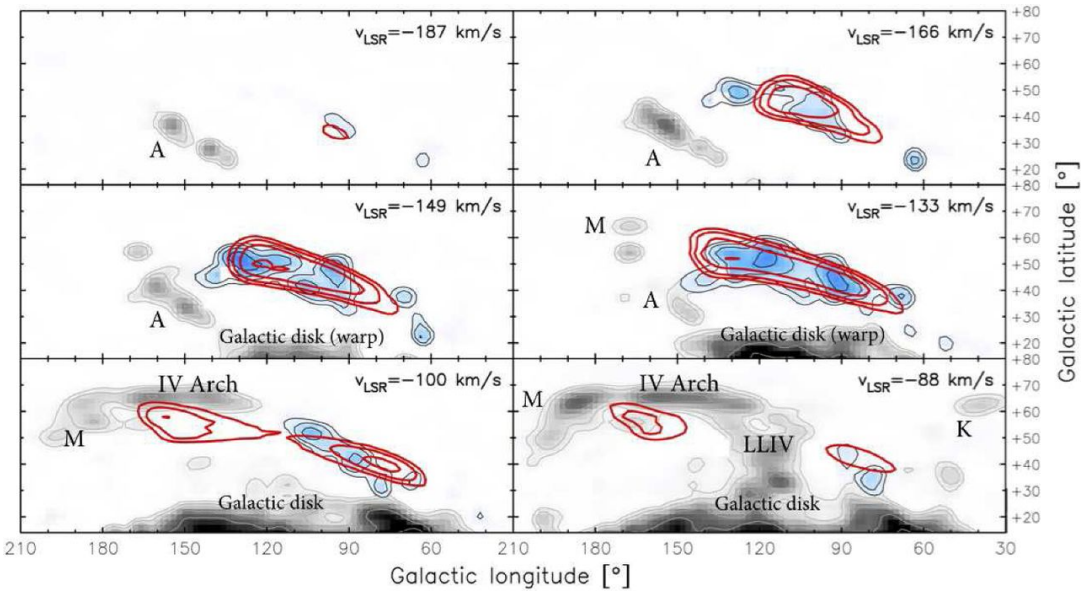

Figure 2.4: Six representative channel velocity maps taken from the HI LAB survey in the region of Complex C. We marked the emission of Complex C with blue shade and black contours to distinguish it from emission due to other sources in that same area (grey shade and contours). The red contours show the HI emission predicted by our model. Both model and data are smoothed to 4° of angular resolution. Note that our model interestingly predicts some emission at low velocities (around $90\,\mathrm{km\,s^{-1}}$), where there is HI detected although it is not usually associated to Complex C. Contour levels are at 0.04, 0.08, 0.16, 0.32, 0.64 and 1.28 K. In this projection, the ejection of seed material took place at about $l = 45°$ and $b = 0°$.

in the (Norma)-Cygnus-Outer spiral arm about 150 million years ago (Fig. 2.1). The best fit to the observations is obtained by ejecting material from this arm at $R = 9.5$ kpc from the Galactic centre (13.3 kpc from the Sun) in a region ~ 3 kpc wide around longitude $l = 45°$. Fig. 2.1 sketches the ejection area along the Cygnus-Outer spiral arm and the current location of Complex C. The quality of the fit to the observations can be appreciated in Fig. 2.4 where we show six representative channel maps from the LAB survey in the region of Complex C (blue shade with black contours) overlaid with the emission predicted by our galactic fountain model (red contours). We can note a remarkable agreement in location, velocity and shape between model and data. We have marked the emission from the disc of the Milky Way, the Galactic warp, the HVC complexes A, M and K, and the IV arch, a prominent intermediate-velocity cloud located at $d < 3.5$ kpc from us with Solar metallicity (Richter et al., 2001), and completely unrelated to Complex C.

In Table 2.5, we summarize the physical properties of Complex C as derived from our dynamical/hydrodynamical model. The material has been ejected vertically at $v_0 \sim 210\,\mathrm{km\,s^{-1}}$ as the result of the blowout of one or more superbubbles. The ejection took place 150 Myr ago, lasted $\sim$ 50 Myr and ejected $3.4 \times 10^6\,\mathrm{M_\odot}$ of

	v_0 ($\mathrm{km\,s^{-1}}$)	R_0 (kpc)	$\delta_{\rm arm}$ (kpc)	t_0 (Myr)
Best-fit	211	9.5	2.9	150
MCMC $2-\sigma$ level	203 - 216	9.4 - 9.6	2.6 - 3.7	145 - 152

	$\Delta_{\rm t}$ (Myr)	$t_{\rm delay}$ (Myr)	$M_{\rm HI}$(seed) ($10^6\,\mathrm{M_\odot}$)	$M_{\rm HI}$(final) ($10^6\,\mathrm{M_\odot}$)
Best-fit	53	46	3.4	6.8
MCMC $2-\sigma$ level	49 - 56	43 - 52	3.0 - 3.8	6.2 - 7.5

Table 2.5: v_0: initial ejection velocity of the disc material; R_0 and $\delta_{\rm arm}$: Galactic radius and size of the ejection region (blowout) along the arm; t_0 and $\Delta_{\rm t}$: look-back time and duration of the ejection; $t_{\rm delay}$: delay time in the hydrodynamical simulation (see the text and Fig. 2.3). $M_{\rm HI}$: HI mass of the seed (disc) material and total current mass of Complex C after the condensation of coronal gas.

hydrogen from the disc plane. The ejected gas acted as a seed for the condensation of the galactic corona bringing the total HI mass budget of the system to $\sim 7\times10^6\,\mathrm{M_\odot}$, in agreement with the estimated mass of Complex C (Wakker et al., 2007). Presently, Complex C is a structure that is 15 kpc in length, and stretches from close to the ejection zone up to a maximum distance from the plane of $\sim$ 10 kpc (Fig. 2.1). The average positions are R = 12.9 kpc and z = 8.4 kpc. The distance from the location of the ejection is due to a combination of the typical trajectory of fountain clouds, which tend to move the gas outwards, the differential rotation of the disc and the pattern speed of the arms. The location and the elongation are remarkably similar to the outcome of hydrodynamical simulations of superbubble blowout in our Galaxy (Melioli et al., 2008).

We compared the predictions of our model to an independent observational constraint, the distance of Complex C. In the literature, there are several limits to the distance of Complex C obtained from detections and non-detections of metal absorption lines against halo stars. The average distance from the Sun is 10 ± 2.5 kpc (Thom et al., 2008) with a mild gradient along the cloud. In Fig. 2.6 we show the distance limits as a function of Galactic longitude (data points with error bars, Wakker et al., 2007; Thom et al., 2008) compared to the average location of the gas in our dynamical model (black curve with gray band). In our model, the section of Complex C closer to us is that further away from the Galactic disc, at higher l and b, and this is consistent with all the distance determinations. This agreement is highly significant: given that the distance information has not been used in the fit to the HI data, this result represents an independent confirmation of our model.

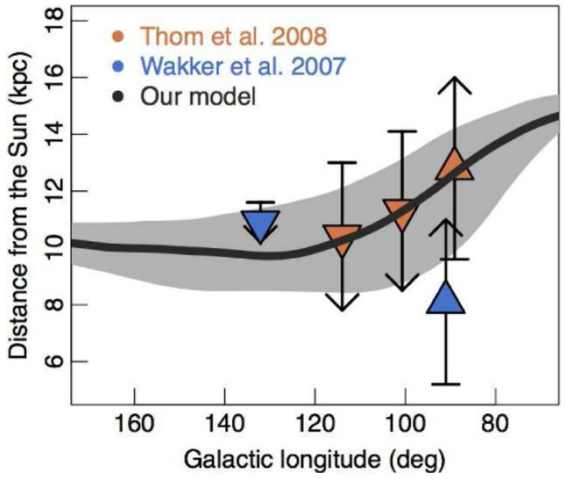

Figure 2.6: Average distance from the Sun of Complex C predicted by our dynamical model as a function of Galactic longitude (black curve), compared with distance determinations from the literature (Wakker et al., 2007; Thom et al., 2008). The grey bands show the 16 and 84 percentiles.

2.3.1 The metallicity of Complex C

An other important observational constraint, which can be compared to our theoretical expectations, is the metallicity of Complex C. As mentioned in Sec. 5.1, the discovery of the low metallicity of Complex C ruled out the hypothesis, proposed by Bregman (1980), according to which Complex C is composed by metal-rich disc gas, ejected from the disc by supernova explosions. Despite recent findings showed metal-enrichment in some regions of Complex (see Sec. 2.1), the overall low metallicity of Complex C has always been considered as evidence for its extragalactic origin. Our model combines the two competing scenarios concerning the origin of Complex C. It suggests that Complex C was produced from the ejection of metal-rich disc material (galactic origin) that has triggered the cooling of a fraction of the metal-poor corona (extragalactic origin). We investigated if our solution may provide a good explanation to the 'low-metallicity' problem of Complex C.

Our fiducial simulation of Complex C (Sec. 2.2.2 and Fig. 2.3) predicts that a mass of gas larger than the initial mass of the cloud condenses from the corona with time, bringing the mass-average metallicity of cold gas to $Z \sim 0.27$ $Z_\odot$ after 200 Myr. The top panel of Fig. 2.7 shows the metallicity map in logarithm scale, obtained from the simulation, after 175 Myr. The map highlights the presence of a clear metallicity gradient along the x-direction, which is the direction of the cloud motion. Regions situated in the head of the mixture, where the gas lost from the cloud is not yet well mixed with the coronal gas, are more metal-rich than the regions situated in the wake, where the bulk of the mixture is composed by coronal gas. The central panels of Fig. 2.7 show a magnifications of a portion of the wake

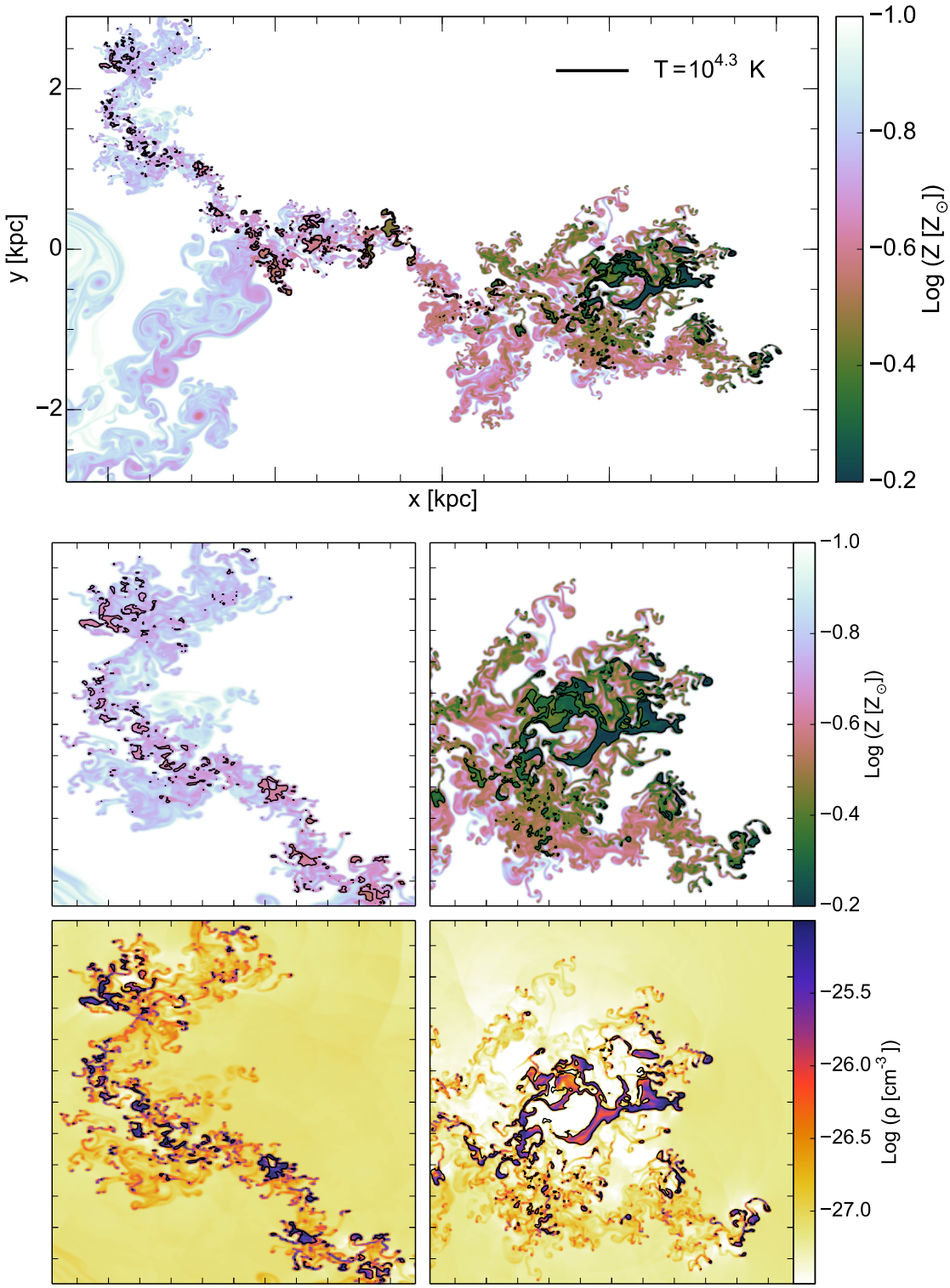

Figure 2.7: *Top panel*: Metallicity distribution on grid of our fiducial simulation after 175 Myr. *Central panels*: metallicity map zoom of a portion of wake (*left panel*) and head (*right panel*) of the mixture. *Bottom panels*: mass density map zoom of the same portion of wake (*left panel*) and head (*right panel*) as the *central panels*. The black contours enclose cold gas at $T < 10^{4.3}$ K.

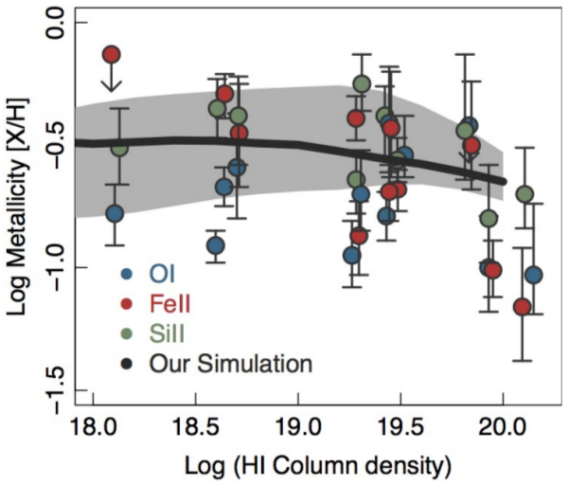

Figure 2.8: Abundances of oxygen, iron and silicon as a function of HI column density (Collins, Shull & Giroux, 2007) compared to the prediction of our hydrodynamical simulation (black curve). The grey bands show the 16 and 84 percentiles.

(left panel) and the head (right panel) of the mixture. The black contours indicate the cold regions at $T < 10^{4.3}$ K (we explain below why we assumed this threshold temperature). The metallicity of the cold gas ranges from $Z \sim 0.8$ $Z_\odot$ (Log [$Z/Z_\odot$] $= -0.2$) in the cloud's fragments not mixed with the coronal gas to $Z \sim 0.2$ $Z_\odot$ (Log [$Z/Z_\odot$] $= -0.7$) in the well-mixed regions of the wake.

Fig. 2.8 shows the comparison between the predictions of our simulation and the observed abundances of Complex C as seen in three most reliable ions, OI, SiII, FeII, as a function of the HI column density (Collins, Shull & Giroux, 2007). We analysed the simulation snapshots between 150 and 200 Myr, where we considered that, in our dynamical model, the ejection time corresponds to $t = t_{\rm delay} \sim 50$ Myr in our fiducial simulation and the travel time of the fountain clouds ranges between 100 and 150 Myr (see Tab. 2.5). Moreover, we accounted only for the gas at $T < 10^{4.3}$ K because, at larger temperatures the above mentioned ions are nearly absent since their abundances with respect to their own atomic species are lower than 10% (Sutherland & Dopita, 1993). We estimated the HI column densities and abundances along random vertical lines across the simulation boxes. The predicted metallicities encompass most of the observed data points and also reproduce the faint negative slope at high HI column densities. Our assumption of 0.1 $Z_\odot$ for the coronal gas implies that our metallicities cannot go below this value and, as a consequence, our model does not reproduce the data points at the lowest metallicities.

In Sec. 2.1, we mentioned that, according to Collins, Shull & Giroux (2007), high column densities correspond to the inner parts of infalling extra-galactic filaments, which mix with Galactic material and accrete metals in their outer parts. Here, we see that our study suggests an alternative explanation. The bottom panels of

Fig. 2.7 show the density distribution on grid of a portion of wake (left panel) and head (right panel) of the mixture, the same regions showed in the metallicity maps (central panels). Again, the black contours indicate the cold regions at $T < 10^{4.3}$ K. We note that the cold and metal-poor knots in the wake are denser than the cloud's fragments in the head: $\rho > 10^{-25.5}$ g/cm^{-3} in metal-poor regions, while $10^{-25.5} \leq \rho \leq 10^{-26.5}$ g/cm^{-3} in the metal-rich head. The cold knots are indeed the well-condensed inner part of the wake, kept out from mixing that occurs in the outer regions. Instead, the cloud's fragments in the head have just begun the mixing with the rarefied coronal material and this has appreciably decreased their density. This anti-correlation between density and metallicity could explain the faint negative slope at high HI column density in Fig. 2.8.

We conclude that our model reconciles the hypothesis of a (partial) disc origin of Complex C with the low observed metallicity. It is important to stress that, as for the distance, the metallicity has not been used in the fit to the HI data, it is in fact determined by the amount of condensation required to reproduce the HI kinematics.

2.4 Technical Discussion

Our fiducial simulation, described in Sec. 2.2.2, was performed without the presence a gravitational field. In this Section, we justify our choice to neglect gravity.

In Fig. 2.9, we present temperature snapshots of a two-dimensional simulation of cloud-corona interaction including the vertical gravitational field of the Galaxy. This simulation was performed taking into account the results of our dynamical model. We assumed that the bottom side of the computational grid ($z = 0$ kpc) corresponds to the Galactic plane, where the z-axis is the direction perpendicular to the plane, and the azimuthal motion of the cloud occurs along the x-axis. The cloud is ejected from the Galactic plane with vertical velocity $v_{z,\rm cl} = 210\,\mathrm{km\,s^{-1}}$, which is the best-fit ejection velocity (see Tab. 2.5), and azimuthal velocity $v_{x,\rm cl} = 75\,\mathrm{km\,s^{-1}}$, which is roughly the relative rotation velocity between Galactic corona and disc at Galactic radius $R \sim 9.5$ kpc (Marinacci et al., 2011; Hodges-Kluck, Miller & Bregman, 2016). Except for the velocity, all the initial parameters of this simulations are the same as those listed in Tab. 2.2. The hot gas is in hydrostatic equilibrium with the vertical gravitational field of the Milky Way at $R \sim 9.5$ kpc, derived from the gravitational potential in Binney & Tremaine (2008), the same one we used to integrate the cloud's orbit in our dynamical model. The density of the hot gas at the bottom side of the computational grid is $n_{\rm cor} = 10^{-3}$ cm^{-3}. The simulation ran for 125 Myr, which is the average orbital time of the clouds in our dynamical model (see Tab. 2.5).

Fig. 2.9 shows that the initial cloud is nearly intact after 105 Myr and the turbulent wake is mainly composed by gas at temperature slightly lower than the coronal temperature. At the end of the simulation, the amount of condensation is less

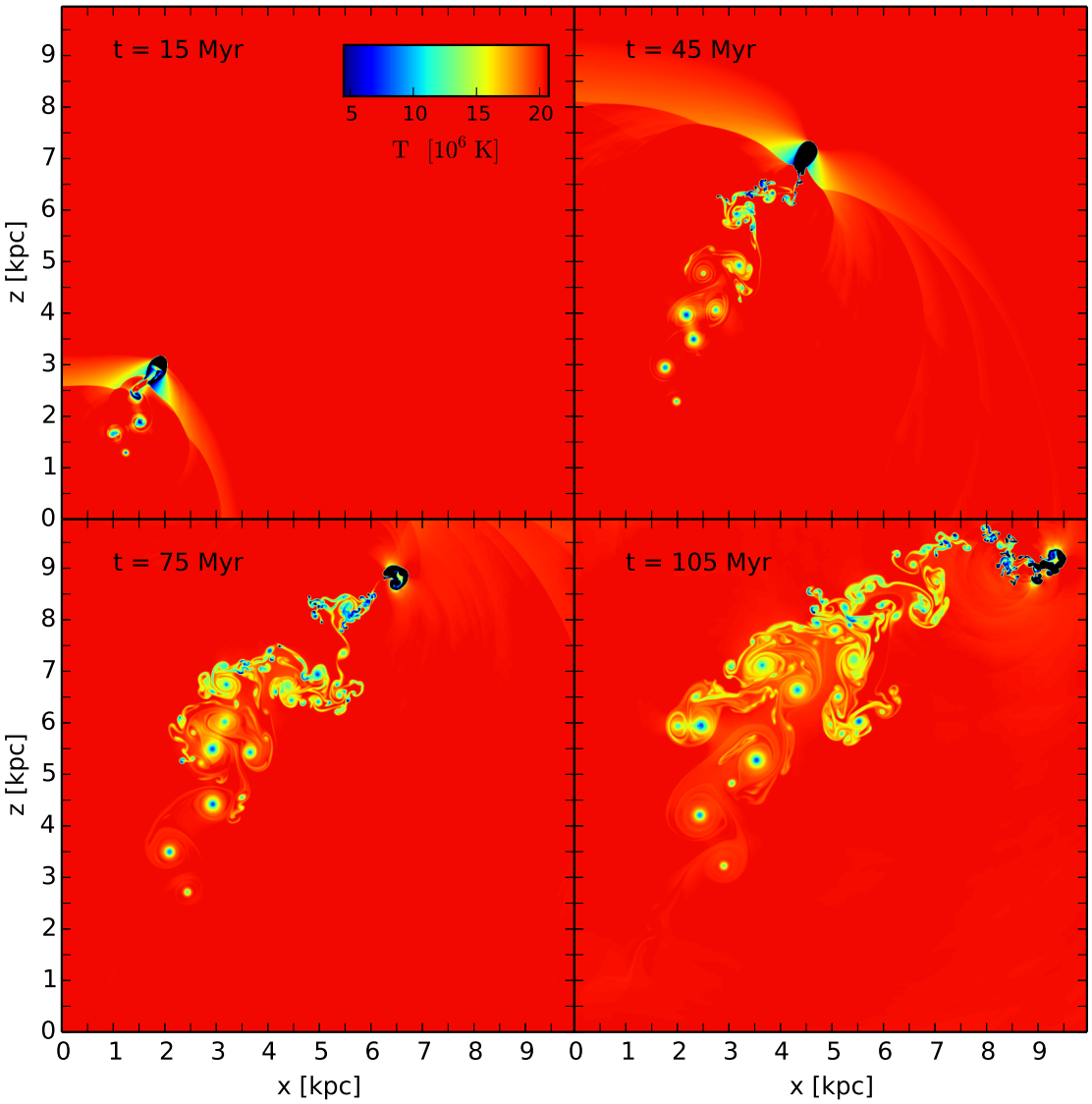

Figure 2.9: Temperature snapshots of a simulation including gravity. The initial parameters are the same as in Tab. 2.2, except the x and z initial velocity components, which are respectively $75\,\mathrm{km\,s^{-1}}$ and $210\,\mathrm{km\,s^{-1}}$. The time at which the snapshots have been taken is indicated in each panel.

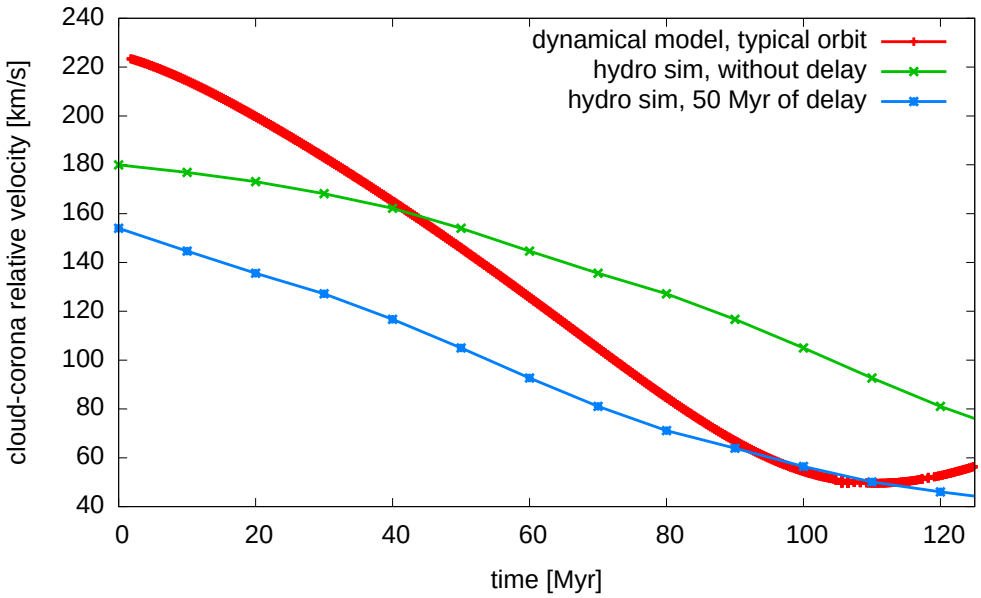

Figure 2.10: Evolution of the cloud-corona relative velocity with time as predicted by the dynamical model (red curve), the fiducial simulation (green curve) and the fiducial simulation excluding the initial 50 Myr (blue curve). 125 Myr indicates the average orbital time of the clouds in our dynamical model.

than 3% of the initial cloud mass, indicating that the cloud loses its own gas slowly and the mixture temperature is not low enough to trigger condensation in a short time-scale. This effect is due to two main factors: the unrealistic spherical shape of the cloud, that hinders the cloud-corona interaction (see Sec.2.2.2), and the initial supersonic velocity of the cloud ($v_{\rm cl} \equiv \sqrt{v_{z,\rm cl}^2 + v_{x,\rm cl}^2} \sim 220\,{\rm km\,s^{-1}}$, $c_{\rm s} \sim 200\,{\rm km\,s^{-1}}$ at $T_{\rm cor} = 2 \times 10^6$ K). As visible in the top panels of Fig. 2.9, when the cloud velocity exceeds the sound speed of the hot gas, a bow shock develops around the cloud, which compact the cloud along the motion direction, preventing its ablation and interaction with the coronal medium (see also Scannapieco & Brüggen, 2015). This effect, combined with the spherical shape of the cloud, further inhibits inhibits significant mixing until to $\sim 75 - 100$ Myr.

It appear that this kind of simulation does not allow us to accurately determine the condensation properties of the corona. Of the two reasons that we identified above for the behaviour of the cloud, i.e. supersonic velocity and round shape, the first one is realistic event, while the second one is an artefact. However, clouds with irregular shape are hard to setup in simulations. An alternative would be to model the whole superbubble blowout but high-resolution simulations of superbubble explosion with a fixed-grid code as ECHO++ are very expensive from a computational point of view. For this reason, in our fiducial simulations we decided to keep the spherical shape for the initial cloud and to study its interaction with the corona in

the absence of gravitational force and at subsonic velocity. We chose relative velocities with respect to the corona compatible with those determined by our dynamical model. Indeed, using similar velocities is crucial because condensation depends on the relative velocity between cloud and corona (Marinacci et al., 2010, 2011). Below, we demonstrate the agreement between the velocities predicted by the model and the velocities of the cloud during our fiducial simulation.

Fig. 2.10 shows the evolution of the cloud-corona relative velocity with time as predicted by our dynamical model (red curve) and our fiducial simulation (green curve and blue curve). Gravity decelerates the cloud motion in the dynamical model, contributing to a faster decreases of the velocity with respect to the simulation, where the cloud motion is driven only by coronal ram pressure and condensation. In the figure, the blue curve was obtained by considering our assumption that the ejection time in the dynamical model corresponds to $t = t_{\rm delay}$ in the simulation (see Sec. 2.2.2 and Tab. 2.5). Instead, the green curve was obtained by considering that the ejection time corresponds to the initial time of the simulation, without accounting for the delay (see Sec. 2.2.2). In the dynamical model, the average velocity during the orbital time is $\sim 120\,{\rm km\,s^{-1}}$, a value comparable with the average velocity of $\sim 100\,{\rm km\,s^{-1}}$ of the simulation starting to $t = t_{\rm delay}$. Moreover, the final velocities are roughly similar, around $50 - 60\,{\rm km\,s^{-1}}$. This comparison justifies our choice of initial velocity of $180\,{\rm km\,s^{-1}}$ for the simulated cloud.

2.5 Discussion and Conclusions

From our dynamical model and the hydrodynamical simulations, we conclude that the most massive and metal-poor Galactic HVC, Complex C, originated from an ejection of material from the Milky Way's disc. This material has travelled through the halo region, mixing with the hot gas from the Galactic corona and triggering its condensation. An important achievement of our work has been to reproduce the distance and the metallicity of Complex C, this latter considered the main signature of its extra-galactic origin. Moreover, the fact that the seed of Complex C originated in the star-forming disc explains the observed over-abundance of α-elements with respect to N and Fe (see. Sec. 2.1).

The source of the gas ejection must have been a prominent star forming region in the Cygnus-Outer arm at $l = 45°$, $b \sim 0°$ and at $d \sim 13.3$ kpc from us. The exact region cannot be easily recognized today as dust extinction along the line of sight prevents us from seeing young open clusters in that area. The development and blowout of a superbubble around a stellar association is the likely cause of the ejection (Mac Low, McCray & Norman, 1989). We estimated an ejected hydrogen mass of $3.4 \times 10^6\,{\rm M_\odot}$ at a velocity of $\sim 210\,{\rm km\,s^{-1}}$. When correcting for He content, this corresponds to a total kinetic energy of 2×10^{54} erg, which can be achieved by

$\sim 10^4$ supernovae assuming an efficiency of 20%. This would require the formation of $1 - 2 \times 10^6\,\mathrm{M}_\odot$ (depending on the IMF) of stars in 50 Myr in a region of a few kpc^2. The inferred star-formation rate density is $\Sigma_{\mathrm{SFR}} \sim 0.01\,\mathrm{M}_\odot\,\mathrm{yr}^{-1}\mathrm{kpc}^{-2}$, quite typical for a star-forming region in the Galactic disc.

A well known recent (30 Myr old) superbubble in the Milky Way is that in Ophiucus, located at $R \sim 4$ kpc from the Galactic centre and currently ejecting material up to 3.5 kpc from the plane (Pidopryhora, Lockman & Shields, 2007). We have used our galactic fountain model to estimate the ejection velocity of this material and found a value of $\sim 200\,\mathrm{km\,s}^{-1}$, as required for complex C. HI holes observed in the ISM of external galaxies are thought to be the remnants of superbubble blowouts. The kinetic energies associated with these holes are in the range $1 \times 10^{53} - 1 \times 10^{55}$ erg (e.g., Boomsma et al., 2008). Thus, the ejection of the seed gas that caused the condensation of complex C is energetically plausible.

Gas accretion from the circumgalactic corona is a viable source to sustain the star formation in our Galaxy (see Sec. 1.3). However, the hot coronal gas needs to cool down to become available for star formation. Linear perturbation analysis suggests that the combination of buoyancy and thermal conduction can efficiently suppress the growth of thermal instabilities (Binney, Nipoti & Fraternali, 2009) and only non-linear perturbations are possible to explain HVC formation (Joung et al., 2012). The present model offers an elegant solution to this problem as the seeds for these instabilities are provided by the Galactic disc itself and the non-linearity of the flow is achieved by the development of turbulence. In this respect, HVCs should be regarded as the extreme manifestation of the galactic fountain phenomenon that is known to explain the origin of the IVCs and the extra-planar gas in the Milky Way (Marasco, Fraternali & Binney, 2012). Moreover, material at intermediate temperature ($10^4 < T < 10^6$ K) produced by the interaction between the cold gas and the corona in the turbulent mixture (see Fig. 2.3-a) is consistent with the detection of cold/warm ionized gas in the halo of our Galaxy (e.g., Sembach et al., 2003; Lehner & Howk, 2011; Marasco, Marinacci & Fraternali, 2013).

We estimated that Complex C will merge with the Galactic disc in ~ 150 Myr, implying an overall orbital time of ~ 300 Myr. By considering the most efficient scenario, in which the mass of condensed gas steadily increases as a power law up to 350 Myr (300 Myr $+\,t_{\mathrm{delay}}$, see Fig. 2.3-c), we calculated the amount of cold gas accreted by complex C and inferred an upper limit of $M_{\mathrm{accr}} = 0.25\,\mathrm{M}_\odot\,\mathrm{yr}^{-1}$, after correcting for the He content. This value is still well below what is needed to replace the gas consumed by star formation ($\sim 1 - 3$ M$_\odot$, Chomiuk & Povich, 2011), thus confirming a scenario where most of coronal gas cooling is triggered by galactic fountains at the intermediate-velocity regime (Marasco, Fraternali & Binney, 2012). During the rare occasions when the ejection of material is extremely powerful, when the ejection velocities are larger than $\sim 150\,\mathrm{km\,s}^{-1}$, the gas will

most likely appear in the high-velocity range. A long travel time through the halo will cause the condensation of a larger fraction of the corona and the metallicity will reach values between those of the disc and the corona, becoming nearly equal to coronal one in the well-mixed regions. Our guess is that several complexes (e.g., Complex K and Complex L) can be explained in this way. Indeed, this scheme is able to explain another well-known HVC, the Smith Cloud. Marasco & Fraternali (2016) applied the same Galactic fountain model to the Smith Cloud, showing that it can originate from powerful gas ejection from the Galactic disc. Those authors found that the orbital time is less than 50 Myr, explaining in this way that the high metallicity of this HVC (Fox et al., 2016) is due to its brief interaction with the Galactic corona.

We conclude that supernova-driven cooling of the lower corona is a general mechanism for accretion of low-metallicity gas in disc galaxies as required by chemical evolution models. As we show in Chapter 4, this phenomenon can explain why, at the present time, only star-forming galaxies acquire gas from their environment, while early-type galaxies have lost their ability to do so despite being surrounded by massive gas reservoirs (Thom et al., 2012).

Chapter 3

Implementation of new physics modules in the ATHENA hydrodynamic code

3.1 Introduction

Hydrodynamical simulations of Chapter 4 and Chapter 5 were performed by using ATHENA (Stone et al., 2008), a grid-based, parallel and multidimensional hydrodynamic code. The code implements algorithms that are built on high-order Godunov methods (Godunov, 1959), based on conservative finite-volume discretization, to integrate numerically the Euler equations (Sec. 3.2).

Godunov methods have become the standard *de-facto* for grid-based hydrodynamical codes thanks to their ideal properties of shock capturing and handling of contact and rotational discontinuities. Indeed, essentially all the hydrodynamic codes widely used in astrophysical applications are based on these integration techniques. Those range from fixed grid codes, as ATHENA, to codes using adaptive mesh refinement (AMR) to improve the accuracy locally, as ENZO (Bryan & Norman, 1997), RAMSES (Fromang, Hennebelle & Teyssier, 2006) and PLUTO (Mignone et al., 2007), or moving-mesh (pseudo-)lagrangian grids (such as AREPO Springel, 2010). We chose to use a fixed-grid code as ATHENA, rather than an AMR code. In fact, from a hydrodynamical point of view, our work focuses on the study

of turbulent mixing that occurs at the interface between different gas phases. This study requires to evolve all gas phases with the same spatial resolution, and the computational advantages of improving the resolution locally with an AMR technique are minimal compared to the increased complexity of use of such a code. Finally, ATHENA is an accurate and adaptable code, easy to modify to include additional physics modules (see Sec. 3.4 and 3.5).

This Chapter is organized as follow. In Sec. 3.2, we introduce the system of Euler equations. In Sec. 3.3, we briefly describe the main structural features of ATHENA. In Sec. 3.4 and Sec. 3.5, we explain, respectively, the details of our implementation of radiative processes (cooling and heating) and thermal conduction in ATHENA. Finally, in Sec. 3.5, we illustrate the analytic theory of thermal conduction (in order to better understand the computational choices made for its implementation) and we show some tests to check the accuracy of thermal conduction algorithm.

3.2 Euler equations

Euler equations can be used to describe the dynamics of astrophysical gas systems, where pression is isotropic and local thermodynamical equilibrium holds, under the assumption that the fluid is collisional. These equations consist in a set of conservation laws, that can be written in conservative form as:

$$\frac{\partial \rho}{\partial t} + \nabla \cdot (\rho \mathbf{v}) = 0\,, \tag{3.1}$$

$$\frac{\partial \rho \mathbf{v}}{\partial t} + \nabla \cdot (\rho\, \mathbf{v} \otimes \mathbf{v} + \mathbf{P}) = 0\,, \tag{3.2}$$

$$\frac{\partial e}{\partial t} + \nabla \cdot [(e + P)\mathbf{v}] = 0\,, \tag{3.3}$$

which represent, respectively, conservation law of mass, momentum and energy. In the previous equations, ρ is the mass density, $\mathbf{v}$ the velocity vector, $\boldsymbol{P}$ is a diagonal tensor with components P, the gas pressure, and e the total gas energy per unit volume. In the case of an ideal fluid (that we treated in this thesis) it is possible to express the volumetric total energy as:

$$e = \frac{P}{\gamma - 1} + \frac{1}{2}\rho ||\mathbf{v}||^2\,, \tag{3.4}$$

where the first term on the right-hand side represents the volumetric internal energy, the second term the volumetric kinetic energy of the fluid. γ, assumed constant, is the adiabatic index, fixed to 5/3 in this work.

Euler equations can be rearranged into a compact form, used to describe the

temporal evolution of the fluid. They can be written in cartesian coordinates as:

$$\frac{\partial \mathbf{U}}{\partial t} + \frac{\partial \mathbf{F}(\mathbf{U})}{\partial x} + \frac{\partial \mathbf{G}(\mathbf{U})}{\partial y} + \frac{\partial \mathbf{H}(\mathbf{U})}{\partial z} = 0\,, \tag{3.5}$$

where $\mathbf{U} = (\rho, \rho v_x, \rho v_y, \rho v_z, e)$ is the vector of conserved variables, $\mathbf{F}(\mathbf{U}) = [\rho v_x, \rho v_x^2 + P, \rho v_x v_y, \rho v_x v_z, (e+P)v_x]$, $\mathbf{G}(\mathbf{U}) = [\rho v_y, \rho v_y v_x, \rho v_y^2 + P, \rho v_y v_z, (e+P)v_y]$ and $\mathbf{H}(\mathbf{U}) = [\rho v_z, \rho v_z v_x, \rho v_z v_y, \rho v_z^2 + P, (e+P)v_z]$ are the vectors of fluxes in the x-, y- and z-directions respectively.

Equation 3.5 can also be written in the following linearized form:

$$\frac{\partial \mathbf{U}}{\partial t} + \frac{\partial \mathbf{F}(\mathbf{U})}{\partial \mathbf{U}}\frac{\partial \mathbf{U}}{\partial x} + \frac{\partial \mathbf{G}(\mathbf{U})}{\partial \mathbf{U}}\frac{\partial \mathbf{U}}{\partial y} + \frac{\partial \mathbf{H}(\mathbf{U})}{\partial \mathbf{U}}\frac{\partial \mathbf{U}}{\partial z} = 0\,, \tag{3.6}$$

with $\partial\mathbf{F}(\mathbf{U})/\partial\mathbf{U}$, $\partial\mathbf{G}(\mathbf{U})/\partial\mathbf{U}$ and $\partial\mathbf{H}(\mathbf{U})/\partial\mathbf{U}$ three Jacobian matrices of the flux vectors $\mathbf{F}$, $\mathbf{G}$ and $\mathbf{H}$. These matrices are diagonalizable and all their eigenvalues are real. For this reason, the Euler equations are an hyperbolic system of conservation laws. Without entering the mathematical details, it can be shown that the Euler equations can also be linearized in the primitive variables $\mathbf{W} = (\rho, v_x, v_y, v_z, P)$, assuming the same hyperbolic form as eq. 3.6, but losing the conservative structure.

Given the hyperbolic character of the Euler equations, each Jacobian matrix, above mentioned, admits three distinct eigenvalues, also called characteristic speeds of the system, $v_i + c_\mathrm{s}$, v_i (of multiplicity 3), $v_i - c_\mathrm{s}$, where c_s is the sound speed and v_i is the velocity of the fluid along the spatial direction i (respectively x y or z when the matrix to solve is $\partial\mathbf{F}(\mathbf{U})/\partial\mathbf{U}$, $\partial\mathbf{G}(\mathbf{U})/\partial\mathbf{U}$ and $\partial\mathbf{H}(\mathbf{U})/\partial\mathbf{U}$). Moreover, since each matrix is diagonalizable, it admits a complete basis of eigenvectors, with respect to which Equation 3.6 can be rewritten in the *characteristic* variables, becoming a system of decoupled wave equations, whose propagation speed is given by the eigenvalues of the matrix. However, for non linear equations, as the Euler equations, the Jacobian matrices are not constant: the interaction among the waves is not given by a simple superposition but leads to discontinuous solutions, shock waves and tangential discontinuities, that propagate with their own velocity.

The hyperbolic nature of the system of Euler equations is the foundation of most numerical schemes that solve the Euler equations in hydrodynamic codes. For instance, in ATHENA, spatial reconstruction algorithms (see Sec. 3.3.1) involve the *characheristic* decomposition of the Euler equations in the primitive variables. Moreover, the eigenstructure of the Euler equations is used to solve the Riemann problem (see Sec. 3.3.2). Therefore, to overcoming of discontinuities due to the non-linearity of the Euler system and subsequent problems of numerical instability is the first challenge of any hydrodynamic code.

3.3 Structure of ATHENA

All the simulations presented in the next chapters were performed with the numerical code ATHENA. In the following, we briefly present its basic features, by showing the integration method to solve the system of equations 3.5 and how ATHENA deals with discontinuous solutions related to the non-linearity of the Euler equations. This Section is not intended to be an exhaustive description of the code, and a complete characterization can be found in Stone et al. (2008).

ATHENA integrates Euler equations on a regular, three-dimensional Cartesian grid. The continuous spatial coordinates, x, y and z, are discretized in N_x, N_y and N_z cells within a finite computational domain of size L_x, L_y and L_z in each direction, respectively. The grid is uniform and the size of each cell in the x-, y- and z-directions are $\Delta x = L_x/N_x$, $\Delta y = L_z/N_z$ and $\Delta z = L_z/N_z$, respectively. Indices i, j and k denote the spatial position, x_i, y_j and z_k, where each cell is centered.

ATHENA works by integrating the system of equations 3.5 over the finite volume of each grid cell and over a discrete time-step Δt, after application of the divergence theorem:

$$\begin{aligned}\mathbf{U}^{n+1}_{i,j,k} = \mathbf{U}^{n}_{i,j,k} &- \frac{\Delta t}{\Delta x}\left(\mathbf{F}^{n+1/2}_{i+1/2,j,k} - \mathbf{F}^{n+1/2}_{i-1/2,j,k}\right) \\ &- \frac{\Delta t}{\Delta y}\left(\mathbf{G}^{n+1/2}_{i,j+1/2,k} - \mathbf{G}^{n+1/2}_{i,j-1/2,k}\right) \\ &- \frac{\Delta t}{\Delta z}\left(\mathbf{H}^{n+1/2}_{i,j,k+1/2} - \mathbf{H}^{n+1/2}_{i,j,k-1/2}\right)\end{aligned} \tag{3.7}$$

where

$$\mathbf{U}^{n}_{i,j,k} = \frac{1}{\Delta x \Delta y \Delta z}\int_{z_{k-1/2}}^{z_{k+1/2}}\int_{y_{j-1/2}}^{y_{j+1/2}}\int_{x_{i-1/2}}^{x_{i+1/2}} \mathbf{U}(x,y,z,t^n)\,dx\,dy\,dz \tag{3.8}$$

indicates the vector of the volume-averaged conservative variables, while

$$\mathbf{F}^{n+1/2}_{i-1/2,j,k} = \frac{1}{\Delta y \Delta z \Delta t}\int_{t_n}^{t_{n+1}}\int_{z_{k-1/2}}^{z_{k+1/2}}\int_{y_{j-1/2}}^{y_{j+1/2}} \mathbf{F}(x_{i-1/2},y,z,t)\,dy\,dz\,dt \tag{3.9}$$

$$\mathbf{G}^{n+1/2}_{i,j-1/2,k} = \frac{1}{\Delta x \Delta z \Delta t}\int_{t_n}^{t_{n+1}}\int_{z_{k-1/2}}^{z_{k+1/2}}\int_{x_{i-1/2}}^{x_{i+1/2}} \mathbf{G}(x,y_{j-1/2},z,t)\,dx\,dz\,dt \tag{3.10}$$

$$\mathbf{H}^{n+1/2}_{i,j,k-1/2} = \frac{1}{\Delta x \Delta y \Delta t}\int_{t_n}^{t_{n+1}}\int_{y_{j-1/2}}^{y_{j+1/2}}\int_{x_{i-1/2}}^{x_{i+1/2}} \mathbf{H}(x,y,z_{k-1/2},t)\,dx\,dy\,dz \tag{3.11}$$

indicate the vectors of the time- and area-averaged fluxes. The half-integer subscript denotes the edge of each computational cell. Then, $x_{i-1/2}$ denotes the interface between the cells centered at x_{i-1} and x_i. The half-integer superscript denotes the

fluxes averaged on the time-step Δt. The maximum stable allowed time-step Δt is fixed by the CFL (Courant-Friedrics-Lewy) condition, which reads:

$$\Delta t = C_0 \min\left(\frac{\Delta x}{|v^n_{x,i,j,k}| + c^n_{\mathrm{s,i,j,k}}}, \frac{\Delta y}{|v^n_{y,i,j,k}| + c^n_{\mathrm{s,i,j,k}}}, \frac{\Delta z}{|v^n_{z,i,j,k}| + c^n_{\mathrm{s,i,j,k}}}\right) \tag{3.12}$$

where $C_0 < 1$ is a numerical constant and the minimum is taken over all grid cells. At each computational time $t = t^n$, $v^n_{x,i,j,k}$, $v^n_{y,i,j,k}$, $v^n_{z,i,j,k}$ denote the flow velocity along the x-, y- and z- directions, while $c^n_{\mathrm{s,i,j,k}}$ denotes the sound speed.

Solving eq. 3.7 requires accurate and stable approximations for the time- and area-averaged fluxes (eq. 3.9, 3.10, 3.11). The operations performed by ATHENA to evolve the conservative variable from time-step n to time-step $n+1$ are listed below:

- Starting from $\mathbf{U}^n_{i,j,k}$, the volume-averaged conservative variables at the time n, the left and right states of the conserved variables are computed at each interface. For example, at the interface $x_{i-1/2}$, the left and right states of $\mathbf{U}^n_{i,j,k}$ are denoted as $\mathbf{U}^n_{\mathbf{L},i-1/2,j,k}$ and $\mathbf{U}^n_{\mathbf{R},i-1/2,j,k}$, respectively. Spatial 1D reconstruction algorithms at first, second and third order of accuracy are implemented in ATHENA (see Stone et al., 2008, for details and Sec. 3.3.1). For our simulations, we used the third-order reconstruction scheme, called *Piecewise Parabolic Reconstruction* (Colella & Woodward, 1984).

- The left and right states of the conserved variables at each interface define a Riemann problem for the Euler equations. The local Riemann problem at cell interfaces is solved with an approximated Riemann solver in order to derive the inter-cell fluxes (see Sec. 3.3.2). The fluxes at the interfaces $x_{i-1/2}$, $y_{j-1/2}$, $z_{k-1/2}$ are respectively:

$$\mathbf{F}^n_{\mathrm{i-1/2,j,k}} = \mathbf{F}(\mathbf{U}^n_{\mathbf{L},i-1/2,j,k}, \mathbf{U}^n_{\mathbf{R},i-1/2,j,k}) \tag{3.13}$$

$$\mathbf{G}^n_{\mathrm{i,j-1/2,k}} = \mathbf{G}(\mathbf{U}^n_{\mathbf{L},i,j-1/2,k}, \mathbf{U}^n_{\mathbf{R},i,j-1/2,k}) \tag{3.14}$$

$$\mathbf{H}^n_{\mathrm{i,j,k-1/2}} = \mathbf{H}(\mathbf{U}^n_{\mathbf{L},i,j,k-1/2}, \mathbf{U}^n_{\mathbf{R},i,j,k-1/2}) \tag{3.15}$$

- Given the inter-cell fluxes along each spatial direction, the left and right states of the conserved variables at each interface are evolved by $\Delta t/2$. For example, at the interface $x_{i-1/2}$, the left and right states of the conserved variable are:

$$\begin{aligned}\mathbf{U}^{n+1/2}_{\mathbf{L},i-1/2,j,k} = \mathbf{U}^n_{\mathbf{L},i-1/2,j,k} &- \frac{\Delta t}{2\Delta y}\left(\mathbf{G}^n_{i-1,j+1/2,k} - \mathbf{G}^n_{i-1,j-1/2,k}\right) \\ &- \frac{\Delta t}{2\Delta z}\left(\mathbf{H}^n_{i-1,j,k+1/2} - \mathbf{H}^n_{i-1,j,k-1/2}\right)\end{aligned} \tag{3.16}$$

$$\begin{aligned}\mathbf{U}^{n+1/2}_{\mathbf{R},i-1/2,j,k} = \mathbf{U}^{n}_{\mathbf{R},i-1/2,j,k} &- \frac{\Delta t}{2\Delta y}\left(\mathbf{G}^{n}_{i,j+1/2,k} - \mathbf{G}^{n}_{i,j-1/2,k}\right) \\ &- \frac{\Delta t}{2\Delta z}\left(\mathbf{H}^{n}_{i,j,k+1/2} - \mathbf{H}^{n}_{i,j,k-1/2}\right)\end{aligned} \tag{3.17}$$

- Starting from the left and right states at $n+1/2$, the new fluxes at cell interfaces are computed by solving again the Riemann problem locally. The new fluxes at the interfaces $x_{i-1/2}$, $y_{j-1/2}$, $z_{k-1/2}$ are respectively:

$$\mathbf{F}^{n+1/2}_{\mathrm{i-1/2,j,k}} = \mathbf{F}(\mathbf{U}^{n+1/2}_{\mathbf{L},i-1/2,j,k}, \mathbf{U}^{n+1/2}_{\mathbf{R},i-1/2,j,k}) \tag{3.18}$$

$$\mathbf{G}^{n+1/2}_{\mathrm{i,j-1/2,k}} = \mathbf{G}(\mathbf{U}^{n+1/2}_{\mathbf{L},i,j-1/2,k}, \mathbf{U}^{n+1/2}_{\mathbf{R},i,j-1/2,k}) \tag{3.19}$$

$$\mathbf{H}^{n+1/2}_{\mathrm{i,j,k-1/2}} = \mathbf{H}(\mathbf{U}^{n+1/2}_{\mathbf{L},i,j,k-1/2}, \mathbf{U}^{n+1/2}_{\mathbf{R},i,j,k-1/2}) \tag{3.20}$$

- Conservative variables, $\mathbf{U}^{n+1}_{i,j,k}$, are updated by using Equation 3.7.

3.3.1 Reconstruction method

Discretization of the conserved variables within each cell involves loss of information about the behaviour of the thermodynamic quantities within regions below the resolution of the grid cell. The aim of a reconstruction method is to interpolate the values of the conserved variables within each cell, in order to provide a good estimate for the left and right states of the conserved variables at the interface between two adjacent cells.

First-order Godunov methods assume a constant distribution of each conserved variable within each cell. However, this procedure is too diffusive and, as mentioned above, leads to loss of information within the cell. In order to increase the spatial accuracy of the Riemann problem (see Sec. 3.3.2), higher-order reconstruction methods have been developed. ATHENA includes both a second-order reconstruction method, the so-called *Piecewise Linear Reconstruction*, and a third-order reconstruction method, the so-called *Piecewise Parabolic Reconstruction* (PPM, Colella & Woodward, 1984). Both schemes are based on the calculation of primitive variables (see Sec. 3.3) at left and right with respect to each interface. The first method assumes that the primitive variables vary linearly within each cell, while the second one assumes that the primitive variables vary by following a monotonic parabolic function.

In order to increase the accuracy of our calculations, we performed all simulations showed in the next chapters by using the PPM method. Here, we omit details about the method (we refer to Stone et al., 2008, for a detailed explanation), but only illustrate the noteworthy features. The PPM method is based on spatial interpolation of the primitive variables and *characteristic* time-evolution of the linearized

Euler system in the primitive variables (see Sec. 3.3) within each cell. Constraints on the monotonicity of the parabolic function are fixed, so that the values on the left and right state of each primitive variable lie between adjacent cell-center values. Cell-by-cell fit, coupled with its monotonic construction and steepening procedure in the vicinity of sharp gradients ensured by the parabolic interpolation, allows to handle correctly discontinuities without the generation of non-physical oscillations.

3.3.2 Riemann solver

The left and right states of each interface, e.g. $\mathbf{U}^n_{\mathbf{L},i-1/2,j,k}$ and $\mathbf{U}^n_{\mathbf{R},i-1/2,j,k}$, are not equal, except in a smooth flow. They define a Riemann problem for Euler equations, whose solution provides the inter-cell flux $\mathbf{F}_{i-1/2,j,k}$. Godunov methods require the solution of this problem at every interface and at each computational time-step.

A Riemann problem is a peculiar initial value problem for Euler equations, or for any system of hyperbolic partial differential equations, characterized by the presence of two constant states separated by a single discontinuity. The solution of the Riemann problem is the time evolution of the various waves and the intermediate states that connect them, which propagate away from the interface. Consider, for example, the discontinuity at the interface $x_{i-1/2}$. The left and right states with respect to the discontinuity, $\mathbf{U}_{\mathbf{L},i-1/2,j,k}$ and $\mathbf{U}_{\mathbf{R},i-1/2,j,k}$, represent the initial conditions of our problem. These states interact giving rise to $m-1$ connecting intermediate states, with m the number of distinct eigenvalues (three for Euler equations) of the Jacobian matrix $\partial\mathbf{F}(\mathbf{U})/\partial\mathbf{U}$ (see Sec. 3.2 and eq. 3.6). All states, including $\mathbf{U}_{\mathbf{L},i-1/2,j,k}$ and $\mathbf{U}_{\mathbf{R},i-1/2,j,k}$, are separated by m characteristic waves that propagate with a given speed b_m. The wave speeds, b_m, do not generally coincide with the eigenvalues of the system (e.g. shock wave indeed propagates with a velocity that is always greater than the highest eigenvalue of the system). The intermediate states and the wave speeds must be determined to solve the problem.

For Euler equations, the analytic solution of a general Riemann problem is available. However, this solution is too computationally expensive, and using accurate methods that solve Riemann problems in some approximate way is more convenient. These algorithms are known as approximate Riemann solvers.

In ATHENA, the inter-cell fluxes are computed using approximate Riemann solvers. The Riemann solver that we used in our simulations is the HLLE solver (Einfeldt et al., 1991), based on the HLL fluxes (Harten, 1983). The HLLE solver imposes that there are only two wave speeds instead of three as in an non-approximate solution and the intermediate state assumes a constant value. According to this

Riemann solver, the inter-cell flux at the interface $x_{i-1/2}$ is given by:

$$\mathbf{F}_{i-1/2,j,k} = \frac{b_+\mathbf{F}(\mathbf{U}_{\mathbf{L},i-1/2,j,k}) - b_-\mathbf{F}(\mathbf{U}_{\mathbf{R},i-1/2,j,k}) + b_+b_-(\mathbf{U}_{\mathbf{L},i-1/2,j,k} + \mathbf{U}_{\mathbf{R},i-1/2,j,k})}{b_+ - b_-} \tag{3.21}$$

with

$$b^+ = \max[\max(\Lambda^M_{\mathbf{L}}, \Lambda^M_{\mathbf{R}}), 0\,], \;\; b^- = \min[\min(\Lambda^0_{\mathbf{L}}, \Lambda^0_{\mathbf{R}}), 0\,] \tag{3.22}$$

where $\Lambda^M_{\mathbf{L}}, \Lambda^M_{\mathbf{R}}$ and $\Lambda^0_{\mathbf{L}}, \Lambda^0_{\mathbf{R}}$ are, respectively, the maximum and minimum eigenvalues of the Jacobian matrix $\partial\mathbf{F}(\mathbf{U})/\partial\mathbf{U}$ calculated at the left $(v_{x,L}+c_{\mathrm{s},L},\, v_{x,L},\, v_{x,L}-c_{\mathrm{s},L})$ and right $(v_{x,R}+c_{\mathrm{s},R},\, v_{x,R},\, v_{x,R}-c_{\mathrm{s},R})$ states of the interface $x_{i-1/2}$. Using a single intermediate state computed from a conservative average, without considering the full eigenvalue structure, makes the HLLE solver slightly more diffusive than other HLL solvers. However, a remarkable advantage of this solver with respect to less diffusive solvers is that the intermediate state is positive-definite, thus impeding the pressure and density in the intermediate state to be negative.

3.4 Radiative cooling and heating

In this Section, we describe how we implemented radiative cooling and heating of the gas in ATHENA. As already discussed in Chapter 2, radiative processes are an important ingredient for our investigations, focused on the time evolution of the mass of cold gas as a consequence of its interaction with a hotter gas phase.

Radiative cooling and heating are inserted as source term in the energy conservation equation (eq. 3.3):

$$\frac{\partial e}{\partial t} + \nabla\cdot[(e+P)\mathbf{v}] = -\rho^2\Lambda_{\mathrm{net}}(T, Z, n_{\mathrm{H}})\,, \tag{3.23}$$

where $\rho^2\Lambda_{\mathrm{net}}$ is the net rate of energy lost by gas per unit volume [erg cm^{-3} s^{-1}] due to radiative processes, and Λ_{net} is the net cooling rate normalized to the square of the total gas density [erg cm^3 s^{-1}]. $\Lambda_{\mathrm{net}} \equiv \Lambda - H$, where Λ and H are, respectively, the gas cooling and heating rates. They depend on the total gas temperature T, metallicity Z and hydrogen number density n_{H}.

In ATHENA the cooling/heating term, $\rho^2\Lambda_{\mathrm{net}}$, is added to the energy fluxes via operator splitting and explicit treatment of the integration time. However, the explicit treatment causes problems of stability when the time-scale associated to radiative processes becomes much smaller than the time-scale associated to hydrodynamic processes (eq. 3.12). To avoid possible problems in regions where radiative cooling is very effective, we limited the hydrodynamic time-step to be a fraction

(10%) of the net cooling time:

$$t_{\rm cool} = \frac{P}{(\gamma - 1)\rho^2 \Lambda_{\rm net}(T, Z, n_{\rm H})} \,. \tag{3.24}$$

We note that $t_{\rm cool}$ strongly depends on the total gas density. In the presence of very high gas densities, the time-step required for stability could be so small that the explicit treatment would becomes impractical due to very long computational times. However, in our simulations, gas densities are low enough to make the explicit treatment of cooling viable. Indeed, the computational time-steps are comparable with the characteristic hydrodynamical time-scale of our simulation or larger than those, given the high resolution of our calculations.

In the next two sections, we illustrate how the values of cooling and heating rates were obtained, and how we inserted them into ATHENA.

3.4.1 Collisional ionization equilibrium

In the first part of the PhD project, we calculated cooling rates by assuming gas in collisional ionization equilibrium. We present the simulations performed under this assumption in Chapter 4.

In the case of collisional ionization equilibrium (CIE), gas is optically thin and external radiation fields that may affect the ionisation balance are absent. Then, radiative heating is null ($H = 0$) and eq. 3.23 becomes:

$$\frac{\partial e}{\partial t} + \nabla \cdot [(e + P)\mathbf{v}] = -\rho^2 \Lambda(T, Z) \,. \tag{3.25}$$

$\Lambda(T, Z)$ is called cooling function. It only depends on temperature T and metallicity Z of the gas.

We adopted the cooling function of Sutherland & Dopita (1993) in the case of CIE. Fig. 3.1 shows three examples of this cooling function, normalized to a hydrogen number density of $n_{\rm H} = 1$ cm^{-3}, for three different values of $\log[Z/Z_\odot]$ (logarithm of gas metallicity in solar units). The cooling curves in Fig. 3.1 overlie for temperatures up to $T \sim 10^{4.25}$ K, where the radiative cooling is mainly dominated by hydrogen recombination. However, at higher temperatures, where a strong contribution to the cooling function is given by metal recombination, the cooling curves are totally different. The presence of metals can indeed increase cooling rates by almost an order of magnitude (or more for lower gas metallicity) going from $\log[Z/Z_\odot] = -1.0$ to $\log[Z/Z_\odot] = 0.0$.

The cooling rates published in Sutherland & Dopita (1993), $\Lambda_{\rm SD}(T, Z)$, are normalized to $n_{\rm e} n_{\rm t}$, being $n_{\rm e}$ and $n_{\rm t}$ the number density of electrons and ions respectively. Since ATHENA works with total mass densities rather than number densities

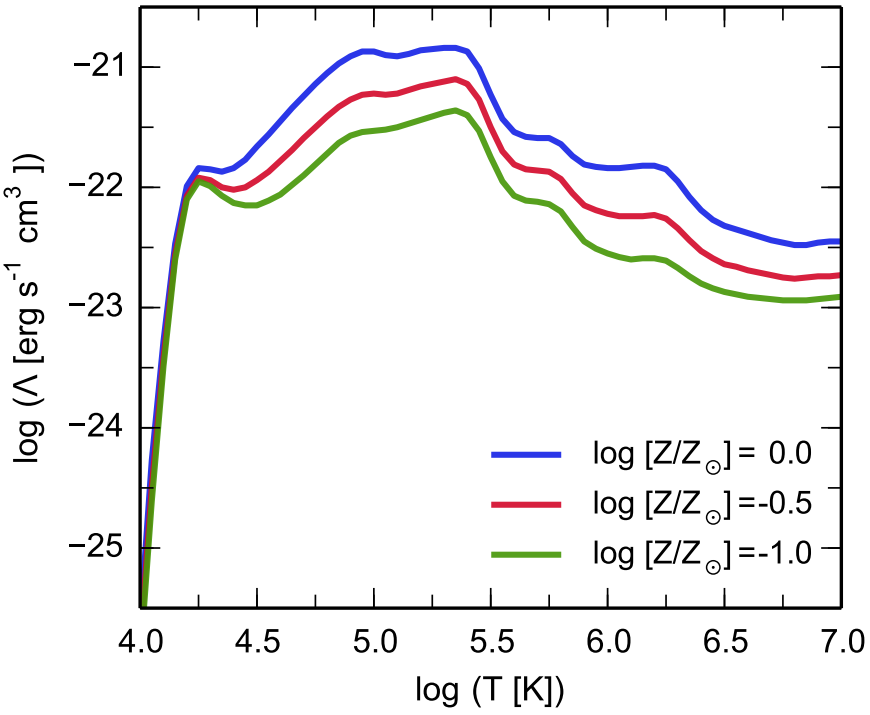

Figure 3.1: Cooling functions with different metal contents (from Sutherland & Dopita, 1993). The curves are normalized to a hydrogen number density of $n_{\rm H} = 1$ cm $^{-3}$. The metallicity of the gas is indicated as $\log[Z/Z_\odot]$, the logarithm of the gas metallicity in solar units.

of electrons and ions, we converted $\Lambda_{\rm SD}(T, Z)$, by normalizing it to the total mass density. The expression for the cooling function, used in ATHENA, $\Lambda(T, Z)$, is therefore:

$$\Lambda(T, Z) = \frac{x(T, Z)}{[1 + x(T, Z)]^2 \bar{\mu}(T, Z)^2} \Lambda_{\rm SD}(T, Z) \,, \tag{3.26}$$

with $x(T, Z) = n_{\rm t}/n_{\rm e}$ and $\mu(\bar{T}, Z)$ mean particle mass:

$$\bar{\mu}(T, Z) = \sum_{i}^{species} \frac{n_{\rm i} m_{\rm i}}{n_{\rm t} + n_{\rm e}} \,, \tag{3.27}$$

being $n_{\rm i}$ is the number density of the species i and $m_{\rm i}$ its mass. The sum is taken over all the species, including both ions and electrons. All the quantities on the right-hand side of eq. 3.26 were taken from Sutherland & Dopita (1993).

To implement the cooling term in ATHENA, we created a lookup table where Λ and $\bar{\mu}$ are listed as a function of T and Z. Temperature ranges from 10^4 to 10^7 K with a resolution of 0.05 dex, while metallicity ranges between 0.1 and 1.0 $Z_\odot$ with a resolution of 0.5 dex. By knowing the values of Z and T in each cell of

the computational domain, the corresponding value of Λ(T,Z) can be calculated through linear interpolation on a logarithmic scale, starting from the tabulated cooling rates. Therefore, to determine the cooling rate needs to know the metallicity and the temperature of the gas in each cell. Below, we describe the procedure that we followed.

At each time-step, the metallicity of each cell is computed as follows. First of all, we note that, in our simulations, metallicity is not fixed across the computational domain but varies with other gas properties and evolves with time as a result of hydrodynamical processes. In ATHENA, metallicity is treated as a passive scalar field, that is as a scalar field advected passively by the fluid, not influencing (directly) its dynamical evolution. In ATHENA (and any grid-based hydrodynamic code), advection of passive scalar fields is treated in the same manner as advection of the mass conservation:

$$\frac{\partial}{\partial t}(\eta\rho) + \nabla \cdot (\rho\eta\mathbf{v}) \; = \; 0 \, . \tag{3.28}$$

The advection equation (eq. 3.28) is integrated, together with the equation of hydrodynamics (eq. 3.1, 3.2 and 3.3) by using the same methods describe in Sec. 3.3. In this way, temporal and spatial evolution of metallicity - and more in general of any scalar quantity passively advected with the fluid - can be followed.

The temperature of each cell is computed from the equation of state of an ideal gas, by inverting the relation:

$$\frac{P}{\rho} - \frac{k_{\rm B} T}{\bar{\mu}(T, Z)} = 0 \, . \tag{3.29}$$

The value of P, ρ and Z are known on the whole computational domain at each time-step. Therefore, it is possible to solve eq. 3.29 for T numerically by using an iterative method. In our implementation we used the secant method (Press et al., 2007).

3.4.2 Photoionization and collisional ionization

In the second part of the PhD project, we included heating by a photoionizing background in our calculations. In particular, we considered the presence of photoionization from a uniform UV background, accounting for the UV radiation emitted by all stars and AGN throughout the evolution of the Universe and attenuated by the Lyα forest (Haardt & Madau, 2012). We present the simulations performed under this assumption in Chapter 5.

The new cooling and heating rates, $\Lambda(T, Z, n_{\rm H})$ and $H(T, Z, n_{\rm H})$, were calculated through the CLOUDY spectral synthesis code (version c13; Ferland et al., 2013). In the model, we included both photoionization from uniform UV background and collisional ionization of all atoms and ions. All chemical elements were assumed

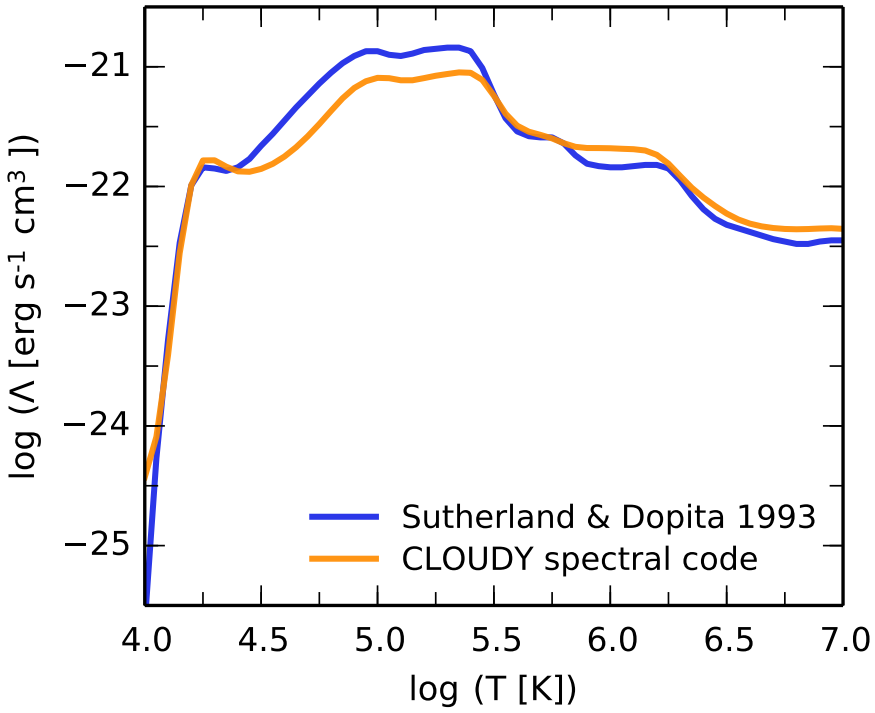

Figure 3.2: Comparison between the cooling function of Sutherland & Dopita (1993) (blue curve) and the cooling function obtained with the CLOUDY spectral code (Ferland et al., 2013) (orange curve) in the case of CIE. Same abundances for each element (taken from Sutherland & Dopita, 1993) and same gas metallicity, $\log[Z/Z_{\odot}] = 0.0$, were assumed. The curves are normalized to a hydrogen number density of $n_{\rm H} = 1$ cm $^{-3}$.

to be in ionization equilibrium, which means that atomic processes (recombination, photoionization, collisional ionization) become steady in a time-scale lower than the hydrodynamical time-scale. We point out the explicit dependence on the gas density of these cooling and heating rates, in contrast with the CIE assumption made in the previous section.

For the implementation of these processes we created a new lookup table where Λ, H and $\bar{\mu}$ (see eq. 3.27 and 3.29) were tabulated as a function of temperature, metallicity and hydrogen number density. T ranges from 10^4 to 10^7 K with a resolution of 0.05 dex in the log space. $\rm n_H$ ranges from 10^{-6} to 1 cm^{-3} with a resolution of 0.5 dex. The gas metallicity assumes three values, $\log[Z/Z_{\odot}] = -1.0, -0.5, 0.0$. In order to be as consistent as possible with the cooling rates calculated by Sutherland & Dopita (1993), we modified the default solar abundances of CLOUDY (most of them taken from Grevesse & Sauval, 1998) and we adopted the solar abundances and the primordial ($\log[Z/Z_{\odot}] \leq -1.0$) ratios from Sutherland & Dopita (1993). For the model at $\log[Z/Z_{\odot}] = -0.5$, we used ratios linearly interpolated on logarithmic scale between the solar and primordial ratios.

Beside temperature, metallicity and hydrogen number density, cooling and heating rates also depend on redshift, z, because the radiation background evolves with time. We considered the effects of the photoionizing radiation background at two different redshifts, $z = 0$ and $z = 0.2$. The reasons of this choice are explained in the next chapters. Thus, we created two different lookup tables depending on redshift and, according to the problem to simulate, we used the relevant one in ATHENA.

Since the tabulated cooling and heating rates depend on n_H, we need to know the value of n_H in each cell of the computational domain and at each time step. For this reason, we calculated the temporal and spatial evolution of n_H by modelling it as a passive scalar field (eq. 3.28). The initial conditions of the hydrogen number density were calculated in each cell as follows:

$$n_H = X(Z)\frac{\rho}{m_H} \tag{3.30}$$

where ρ is the total gas density, m_H is the hydrogen mass, while $X(Z)$ is the hydrogen mass fraction, as obtained by CLOUDY. The value of X slightly decreases with increasing metallicity.

In Chapter 4 we present results obtained using the cooling rates of Sutherland & Dopita (1993), therefore we consider worthwhile to compare the cooling function of Sutherland & Dopita (1993) with the cooling function calculated with CLOUDY, in order to evaluate their potential different impact on our results. Fig. 3.2 show this comparison at $\log[Z/Z_\odot] = 0.0$. Collisional ionization equilibrium and absence of UV radiation were assumed in both cases. Despite we used the same solar abundances, the two curves present slight differences. The most significant one corresponds to the double peak at $10^5 < T < 10^{5.5}$ K due to metal cooling, where the cooling function obtained with CLOUDY exhibits lower cooling rates (difference $< 50\%$). The disagreement is likely due to differences in dielectric rate coefficients, which control the double-peak behaviour (see also Gnat & Sternberg, 2007). We conclude that, by using the cooling function obtained by CLOUDY, the process of gas condensation could become slower (i.e. less efficient) in the range of temperature between $10^{4.5}$ and $10^{5.5}$ K and the amount of cold gas estimated at each time could be slightly lower.

Fig. 3.3 shows the net cooling rates, normalized to n_H^2, as a function of temperature at various hydrogen number densities. Radiation background at redshift $z = 0$ was adopted. For comparison, the orange dashed curve shows the cooling function under the assumption of CIE. At $T \sim 10^{4.5}$ K the curve at low density and metallicity shows a discontinuity, below which heating dominates over cooling. We plotted this region using a dash-dotted line, in order to distinguish it from the region where cooling dominates. The main effect of UV radiation background is to increase the ionization state of the gas, reducing the number of atoms/ions that can

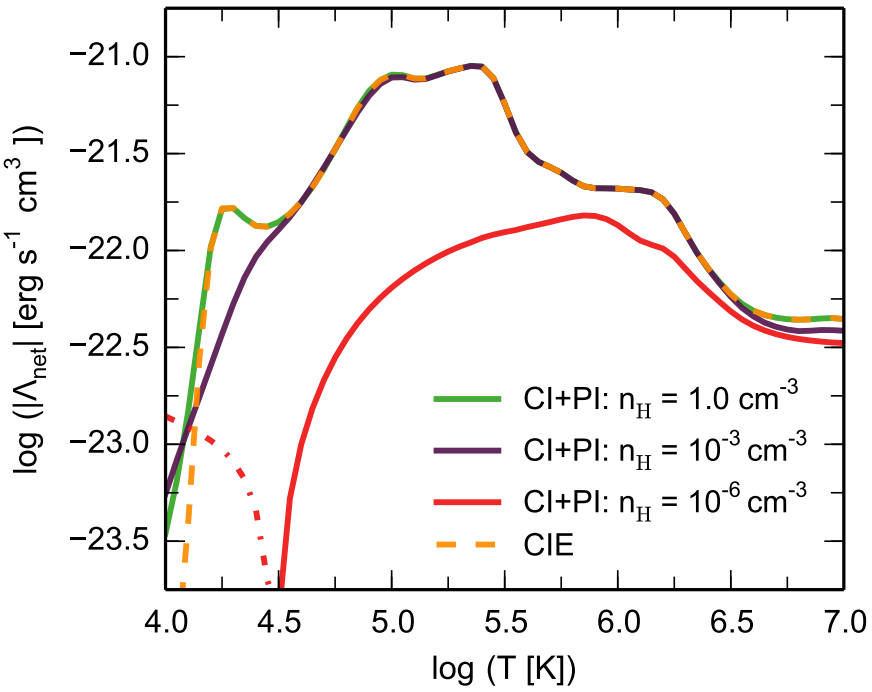

Figure 3.3: Absolute value of net cooling rate ($|\Lambda_{\rm net}| = |\Lambda - H|$) as a function of temperature for $n_{\rm H} = 1.0$ cm^{-3} (green solid curve), $n_{\rm H} = 10^{-3}$ cm^{-3} (violet solid curve), $n_{\rm H} = 10^{-6}$ cm^{-3} (red solid curve). The curves were obtained by assuming both collisional ionization (CI) and photoionization (PI) by uniform UV background at $z = 0$ (Haardt & Madau, 2012). Each curve is normalized relative to $n_{\rm H}^2$. For comparison we show cooling rates in the case of CIE (orange dashed curve). The dash-dotted line for $n_{\rm H} = 10^{-6}$ cm^{-3} indicates that at lower gas density heating dominates over cooling ($\Lambda - H < 0$) at $T < 10^{4.5}$ K. All cooling functions were calculated assuming $\log[Z/Z_{\odot}] = 0.0$.

be collisionally excited. As a consequence, cooling rates decrease with respect to the case of CIE. However, cooling rates strongly depend on $n_{\rm H}$. Indeed, the higher the density of hydrogen atoms ionized by UV radiation, the larger the number of free electrons which can trigger collisional recombination cooling of metals. The cooling function at $n_{\rm H} = 1$ cm^{-3} overlaps the CIE cooling function, except at $T < 10^{4.1}$ K, where it presents higher values of the cooling rate due to the high number density of free electrons that enhance forbidden line cooling from low ionization elements. At intermediate densities the function departs from the CIE function only for $T < 10^{4.5}$ K.

3.5 Thermal Conduction

The most important development work carried out on the code during the PhD project was the implementation of a module for isotropic thermal conduction in

ATHENA. Despite a module for thermal conduction was already present, we implemented a new algorithm more suitable for our purposes (see Sec. 3.5.2 for details).

In the following, a brief description of the analytic theory of thermal conduction (Sec. 3.5.1) is presented, in order to better understand the choices made for its treatment (Sec. 3.5.2). Some tests of the algorithm are proposed in Sec. 3.5.3.

3.5.1 Analytic theory

Thermal conduction is the transfer of energy arising from a temperature gradient at the interface between two different gas phases. Classical theory is based on the assumption that, in a fully ionized plasma, the mean free path of the electrons is much smaller than the temperature scale-length, so that the heat is conducted by the electrons through collisions. Hot electrons transfer heat to the colder medium and the net effect is a smoothing of the temperature gradient at the interface between the two fluids. Under these assumptions, thermal conduction is given by (Spitzer, 1962):

$$\boldsymbol{q}_{\rm class} = -\kappa_{\rm Sp}\,\nabla T\,, \tag{3.31}$$

where $\boldsymbol{q}_{\rm class}$ is the so-called 'heat conduction flux', ∇T is the temperature gradient, and the heat conduction coefficient is:

$$\kappa_{\rm Sp} = \frac{1.84\times10^{-5}T^{5/2}}{\ln\Psi}\ \ {\rm erg\,s^{-1}\,K^{-1}\,cm^{-1}}\,. \tag{3.32}$$

$\ln\Psi$ is the Coulomb logarithm and it can be expressed as

$$\ln\Psi = 29.7 + \ln\left[\frac{T_e/10^6K}{\sqrt{n_e/cm^{-3}}}\right] \tag{3.33}$$

with $n_{\rm e}$ being the electron density and $T_{\rm e}$ the electron temperature.

In several astrophysical situations, the classical theory of thermal conduction is not directly applicable, and in particular the efficiency of thermal conduction is (strongly) reduced compared to the Spitzer value presented in eq. 3.31. For instance, in the presence of magnetic fields, the motion of the conducting electrons is not isotropic but parallel to the magnetic field lines, so the classical thermal conduction (eq. 3.31) is strongly reduced in the transverse direction. The Spitzer formula (eq. 3.31) is replaced by Balbus (1986):

$$\boldsymbol{q} = -\kappa_{||}\,\hat{\mathbf{b}}\,(\hat{\mathbf{b}}\cdot\nabla T) + \kappa_{\perp}\,[\nabla T - \hat{\mathbf{b}}\,(\hat{\mathbf{b}}\cdot\nabla T)]\,, \tag{3.34}$$

where $\hat{\mathbf{b}} = \mathbf{B}/|\mathbf{B}|$ is the unit vector in the direction of magnetic field, $\kappa_{||}$ and $\kappa_{\perp}$ are the heat conduction coefficients along and across the magnetic field. Perpendicular to the field, the electrons follow circular Larmor orbits with radius much smaller

than their own mean free path, so $\kappa_{\perp}$, which depends on the Larmor radius, is effectively zero. In presence of an ordered magnetic field $\kappa_{||} \sim \kappa_{\rm Sp}/3$ because thermal conduction is in one dimension rather than three.

In realistic astrophysical applications, magnetic field is tangled and thermal conduction behaves in a different way with respect to the simple case above mentioned, since heat transfer follows the anisotropic and chaotic electron motions. Therefore, an accurate study of astrophysical phenomena requires to model anisotropic thermal conduction in the hydrodynamic codes. However, implementing stable numerical algorithms solving the anisotropic heat transfer equation (eq. 3.34) is not trivial (see Kannan et al., 2016, for a detailed discussion). In order to make easier the treatment of thermal conduction, the effect of a tangled magnetic field is usually taken into account by multiplying the Spitzer formula by a dimensionless parameter f, less than or of the order of unity:

$$\boldsymbol{q} = -f\,\kappa_{\rm Sp}\,\nabla T\ . \tag{3.35}$$

Rechester & Rosenbluth (1978) and Chandran & Cowley (1998) estimated that, in the presence of a tangled magnetic field, the coefficient of thermal conduction is a factor of $\sim 100 - 1000$ lower than the Spitzer coefficient. Narayan & Medvedev (2001) found that if the turbulence extends on a wide range of length scales, as it might happen with strong-intermediate MHD turbulence, the efficiency of the Spitzer thermal conduction depends on the ratio between the minimum turbulence length scale and the relevant scale of the structure: f increases for decreasing turbulence length scales, converging around a maximum value of ~ 0.2.

The Spitzer formula also breaks down when the local temperature scale-length falls below the mean free path of the conducting electrons. In this case the heat flux is replaced by a flux-limited form, the so-called 'saturated heat flux' (Cowie & McKee, 1977):

$$|\,\boldsymbol{q}_{\rm sat}| = 5\Phi_{\rm s}\rho c^3\ , \tag{3.36}$$

where c and ρ are the plasma sound speed and density, respectively. We accounted for the suppression of saturated thermal conduction due to the presence of magnetic fields through $\Phi_{\rm s}$, where $\Phi_{\rm s} \sim \sqrt{f}$ (see also Cowie & McKee, 1977). This dependence can be understood through the following argument. If we call θ the angle between the local direction of the magnetic field and the local direction of the temperature gradient, the classical thermal conduction is reduced by a factor $\cos^2\theta$, where the first $\cos\,\theta$ corresponds to the projection of the temperature gradient onto the magnetic field direction and the second $\cos\,\theta$ corresponds to the projection of the resulting heat flux, parallel to the magnetic field, onto the direction of the flux gradient. However, the saturated heat flux (eq. 3.36) does not depend on the temperature gradient, therefore it is only reduced by a factor $\cos\,\theta$. In our simulations we assumed

$\Phi_s = \sqrt{f}$, neglecting other possible reductions of the saturated thermal conduction (as uncertainties connected with the flux-limited treatment) besides suppression due to magnetic fields.

Dalton & Balbus (1993) introduced a formula that takes into account a smooth transition between the classical and saturated regime:

$$\boldsymbol{q}_{\rm eff} = -\frac{\kappa_{\rm Sp}}{1+\sigma}\nabla T\ , \tag{3.37}$$

where σ is the ratio between the classical heat flux and the saturated heat flux

$$\sigma = \frac{\kappa_{\rm Sp}||\nabla T||}{5\Phi_s \rho c^3}\ . \tag{3.38}$$

$||\nabla T||$ being the magnitude of the local temperature gradient. Equation 3.37 guarantees that the thermal conduction is significantly reduced for $\sigma \geq 1$, and that the heat flux never exceeds the maximum saturated value. We will adopt this expression for the heat flux for the inclusion of thermal conduction in the ATHENA code.

3.5.2 Including thermal conduction in ATHENA

The module for isotropic thermal conduction originally present in ATHENA solves the classical heat conduction equation (eq. 3.31) under the assumption that the heat conduction coefficient (eq. 3.32) is constant. However, for an accurate treatment of isotropic thermal conduction, considering the strong dependence of the heat conduction coefficient on temperature ($k_{\rm Sp} \propto T^{5/2}$) is essential. We modified the algorithm present in ATHENA, taking into account not only this dependence but also possible effects of saturation and the low efficiency of thermal conduction due to the presence of magnetic fields. For all these purposes, we numerically implemented the analytic formula given by a combination of eq. 3.35 and 3.37:

$$\boldsymbol{q} = -f\frac{\kappa_{\rm Sp}}{1+\sigma}\nabla T. \tag{3.39}$$

with $\kappa_{\rm Sp}$ given by eq. 3.32.

We did not use the explicit update of thermal conduction present in the original version of ATHENA, because it involves very restrictive CFL constraints on the computational time-step (eq. 3.12). Indeed, as already explained for the time-scale associated to radiative processes, the explicit treatment causes problems of stability when the hydrodynamic time-scale is larger than the time-scale associated to thermal conduction:

$$t_{\rm cond} = \frac{P}{(\gamma-1)\kappa_{Sp}T}\left[\min(\Delta x, \Delta y, \Delta z)\right]^2 \tag{3.40}$$

where Δx, Δy and Δz are the cell sizes in the three spatial directions, as defined in

Sec. 3.3. We note that, while the hydrodynamic time-scale linearly depends on the cell size, the conduction time-scale depends on its square. The high resolution of our calculations entails very small cell sizes and, then, conduction time-scales generally an order of magnitude (or more) lower than the characteristic hydrodynamic time-scale. In order not to limit the hydrodynamic time-step to the conduction time-step and to avoid very long computational times, we implemented an semi-implicit time integration scheme. This method achieves the stability of an implicit method, preserves the accuracy of an explicit method, which does not require approximation due to the non-linearity of the energy equation and assures a more realistic time-dependent solution.

Thermal conduction introduces in the energy conservation equation eq. 3.3 a source term of the form:

$$\frac{\partial e}{\partial t} + \nabla \cdot [(e + P)\mathbf{v}] = -\nabla \cdot \boldsymbol{q} \, . \tag{3.41}$$

In our newly implemented thermal conduction module, this term is included into ATHENA by adding it at first order via operator splitting to the energy equation. In practice, we treated thermal conduction by solving the equation for the evolution of the internal energy density due to heat conduction only, by keeping fixed all the other gas variables such as density. The resulting equation is a parabolic partial differential equation, that in a 3D cartesian geometry can be written:

$$\frac{\partial U}{\partial t} = \frac{\partial}{\partial x}\left(\kappa_{\mathrm{Sp}}\frac{\partial T}{\partial x}\right) + \frac{\partial}{\partial y}\left(\kappa_{\mathrm{Sp}}\frac{\partial T}{\partial y}\right) + \frac{\partial}{\partial z}\left(\kappa_{\mathrm{Sp}}\frac{\partial T}{\partial z}\right) \, , \tag{3.42}$$

$U = P/(\gamma - 1)$ being the gas internal energy density. Equation 3.42 can be easily transformed into an equation for the temperature evolution:

$$\frac{\partial T}{\partial t} = \frac{T}{U}\left[\frac{\partial}{\partial x}\left(\kappa_{\mathrm{Sp}}\frac{\partial T}{\partial x}\right) + \frac{\partial}{\partial y}\left(\kappa_{\mathrm{Sp}}\frac{\partial T}{\partial y}\right) + \frac{\partial}{\partial z}\left(\kappa_{\mathrm{Sp}}\frac{\partial T}{\partial z}\right)\right] \, , \tag{3.43}$$

which is the form of heat conduction that we numerically solve in our new thermal conduction module.

To solve the heat equation (eq. 3.43), we used an Alternating Direction Implicit (ADI) method, a finite difference method that splits the heat equation into the three spatial directions. Below we show the discretization algorithm for the x spatial direction only. Note that in this case the y and z coordinates are kept constant. The x spatial direction represents only one of the three sub-cycles of time integration (two for 2D problems) of which the ADI method is composed. In the following sub-cycles, the y and z spatial directions are treated separately using the same strategy, but with the new temperature distributions. We point out the non-linearity of the heat equation (eq. 3.43): κ_{Sp} is not constant but strongly temperature dependent,

$\kappa_{\rm Sp} \equiv \kappa_{\rm Sp}(T) \propto T^{5/2}$ (see eq. 3.32). We solved eq. 3.43 using a specific ADI method for non-linear parabolic partial differential equations (Press et al., 2007), as detailed below. The semi-implicit approach was taken from Vieser & Hensler (2007a): the implicit part is weighted by a factor $0.5 < \alpha < 1$ and the explicit part by a factor $1-\alpha$. In practice, we discretized eq. 3.43 as follows:

$$\frac{T^{n+1}_{i,j,k} - T^{n}_{i,j,k}}{\Delta t/N} = \alpha \left\{ \frac{T^{n+1}_{i,j,k}}{e^{n+1}_{i,j,k}} \frac{1}{\Delta x^2} \left(u^{n+1}_{i+1,j,k} - 2u^{n+1}_{i,j,k} + u^{n+1}_{i-1,j,k} \right) \right\} + (1-\alpha) \left\{ \frac{T^{n}_{i,j,k}}{e^{n}_{i,j,k}} \frac{1}{\Delta x^2} \left[\kappa_{\rm Sp}(T^{n}_{i+1/2,j,k}) \left(T^{n}_{i+1,j,k} - T^{n}_{i,j,k} \right) - \kappa_{\rm Sp}(T^{n}_{i-1/2,j,k}) \left(T^{n}_{i,j,k} - T^{n}_{i-1,j,k} \right) \right] \right\}, \tag{3.44}$$

being N the number of spatial directions of the problem (3 in a 3D geometry), and:

$$du = \kappa_{\rm Sp}(T) dT \implies u = \int \kappa_{\rm Sp}(T) dT = \frac{2}{7} \kappa_{\rm Sp}(T)\, T\,, \tag{3.45}$$

discretizing and expanding $u^{n+1}_{i,j,k}$ as

$$u^{n+1}_{i,j,k} \equiv u(T^{n}_{i,j,k}) + (T^{n+1}_{i,j,k} - T^{n}_{i,j,k}) \left. \frac{\partial u}{\partial T} \right|^{n}_{i,j,k} = \frac{2}{7} \kappa_{\rm Sp}(T^{n}_{i,j,k})\, T^{n}_{i,j,k} + (T^{n+1}_{i,j,k} - T^{n}_{i,j,k})\, \kappa_{\rm Sp}(T^{n}_{i,j,k})\,. \tag{3.46}$$

The equations 3.44, 3.45 and 3.46 can be rearranged in order to assume the following tridiagonal matrix form:

$$A_{i,j,k} T^{n+1}_{i-1,j,k} + B_{i,j,k} T^{n+1}_{i,j,k} + C_{i,j,k} T^{n+1}_{i+1,j,k} = D_{i,j,k}\,, \tag{3.47}$$

where the i index varies along the x axis and the j and k index are kept constant. This equation matrix, which has a tridiagonal form, can be efficiently solved with the 'Thomas algorithm' (see e.g., Press et al., 2007).
Finally, the α parameter depends on the ratio between the hydrodynamic time-scale (eq. 3.12) and the conduction time-scale (eq. 3.40), $\beta = t_{hydro}/t_{cond}$:

$$\alpha = \frac{1 - \beta - \exp(-\beta)}{\beta(\exp(-\beta) - 1)} \tag{3.48}$$

with the additional limitation: $\alpha = 0.5$ if $\alpha < 0.5$ and $\alpha = 1.0$ if $\alpha > 1.0$. Therefore the implicit part contribution is dominant if the conduction time-scale is much smaller than the hydrodynamic time-scale, and it is 50% or more in the other cases.

In the discussion above, for simplicity, we have shown only the algorithm to solve eq. 3.31. The solution of eq. 3.39 is simply obtained by replacing $\kappa_{\rm Sp}$ by $f[\kappa_{\rm Sp}/(1+$

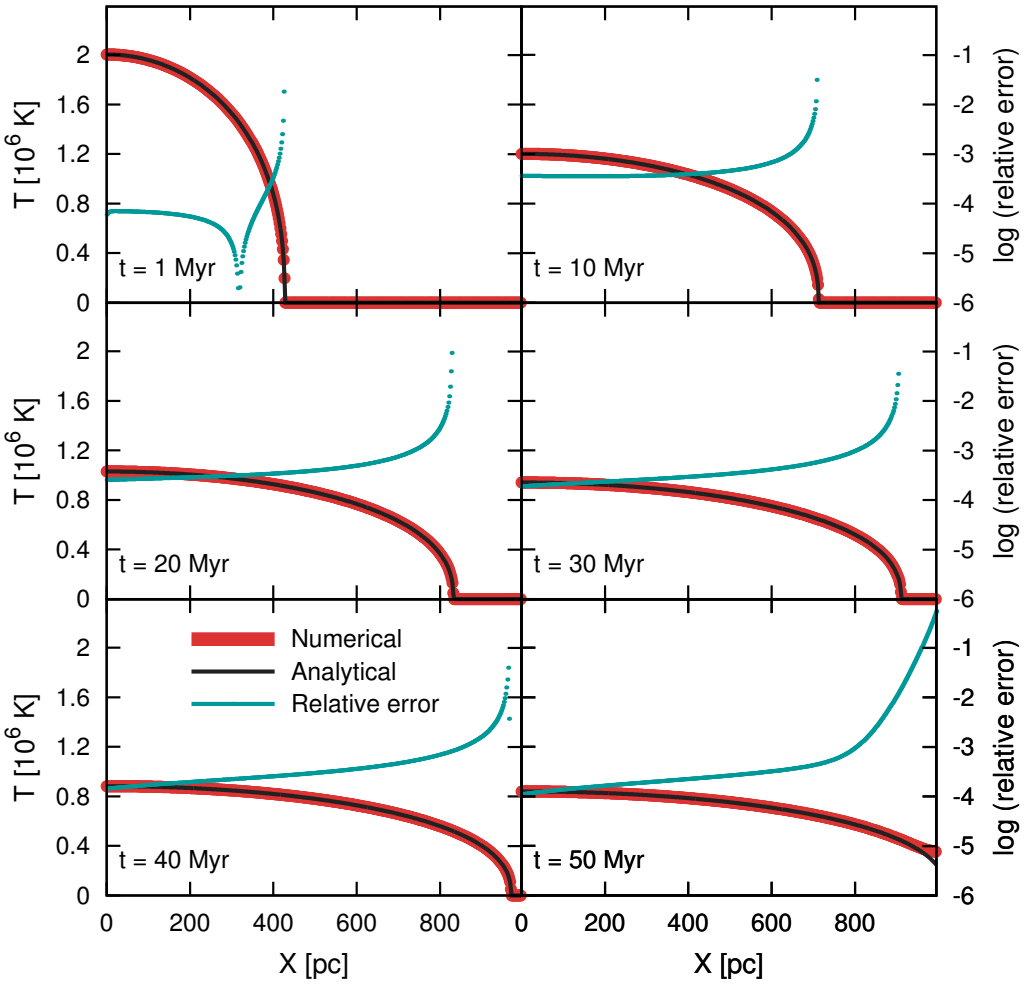

Figure 3.4: Propagation of the conduction front with time. Comparison of the numerical results (red curve) with the analytic solution (black curve). The relative error between the two solution is also plotted (cyan curve).

$\sigma)]$. We treated $f[\kappa_{\rm Sp}/(1+\sigma)]$ as a single coefficient depending on temperature and we discretized σ as follows:

$$\sigma = \frac{\kappa_{\rm Sp}||\nabla T||}{5\Phi_{\rm s}\rho c^3} \implies \sigma_{i,j} = \frac{\kappa_{\rm Sp}(T_{i,j})\,||(T_{i+1,j} - T_{i-1,j})/(2\Delta x)||}{5\Phi_{\rm s}\rho_{i,j}{c_{i,j}}^3}\,, \tag{3.49}$$

when solving the heat equation (eq. 3.43) in the x spatial direction. An analogous formula is used for the y and z directions.

3.5.3 Testing the algorithm

Propagation of a plane conduction front: pure conduction test

To test the accuracy of the algorithm we computed the numerical solution in the case of the classical propagation of a plane conduction front in a static uniform medium, in which the gas density is kept constant throughout the whole time evolution. For this test only thermal conduction across the plasma has been considered, therefore only eq. 3.43 has been solved. An analytic solution for the temperature distribution as a function of time exists for this problem (Reale, 1995):

$$T = T_{\rm c}\left(1 - \frac{x^2}{x_{\rm f}^2}\right)^{2/5} , \tag{3.50}$$

$$T_{\rm c} = 0.6\left(\frac{Q^2}{at}\right)^{2/9} , \tag{3.51}$$

$$x_{\rm f} = 1.01\,(Q^{5/2}at)^{2/9} . \tag{3.52}$$

For the numerical solution we took as initial profile the analytic solution at $t = 1$ Myr for a plasma with numeric density $n = 10^{-3}$ cm^{-3}. In 3.51 and 3.52, a is a constant value equal to $5.6 \times 10^{-7}(\gamma - 1)/(k_{\rm B}n)$, with $k_{\rm B}$ the Boltzmann constant. Q is the integral of T over the whole space, that we assumed to be 1.5×10^9 K pc, corresponding to an maximum temperature $T = 2 \times 10^6$ K at $t = 1$ Myr. The grid is 1 kpc long and it is composed by 500 cells, with a resolution of 2 pc. Zero-gradient conditions on the temperature were imposed at all boundaries. Fig. 3.4 shows the numerical solution, the analytic solution and the relative error for different times. In general, the numerical solution is in very good agreement with the analytic solution. The relative error within the hottest region of the plasma is less than 1%. In the panels at 1, 10, 20, 30, 40 Myr the relative error trend becomes asymptotic when the temperature falls to zero. In this region the relative error is meaningless because it was calculated by dividing the difference between the analytic and numeric solution for a null value. In the last panel the difference between the two trends at the boundaries is visible and the relative error amounts to about 70%. This is due to the temperature gradient forced to be zero at the grid boundary.

Propagation of a plane conduction front: test with conduction and plasma dynamics

As an additional test, we simulated the propagation of a plane conduction front including also the plasma hydrodynamics. Therefore, the whole set of Euler equations (eq. 3.1, 3.2, 3.3) has been solved, taking into account the presence of thermal conduction. In this way, the thermal conduction algorithm was tested within the code

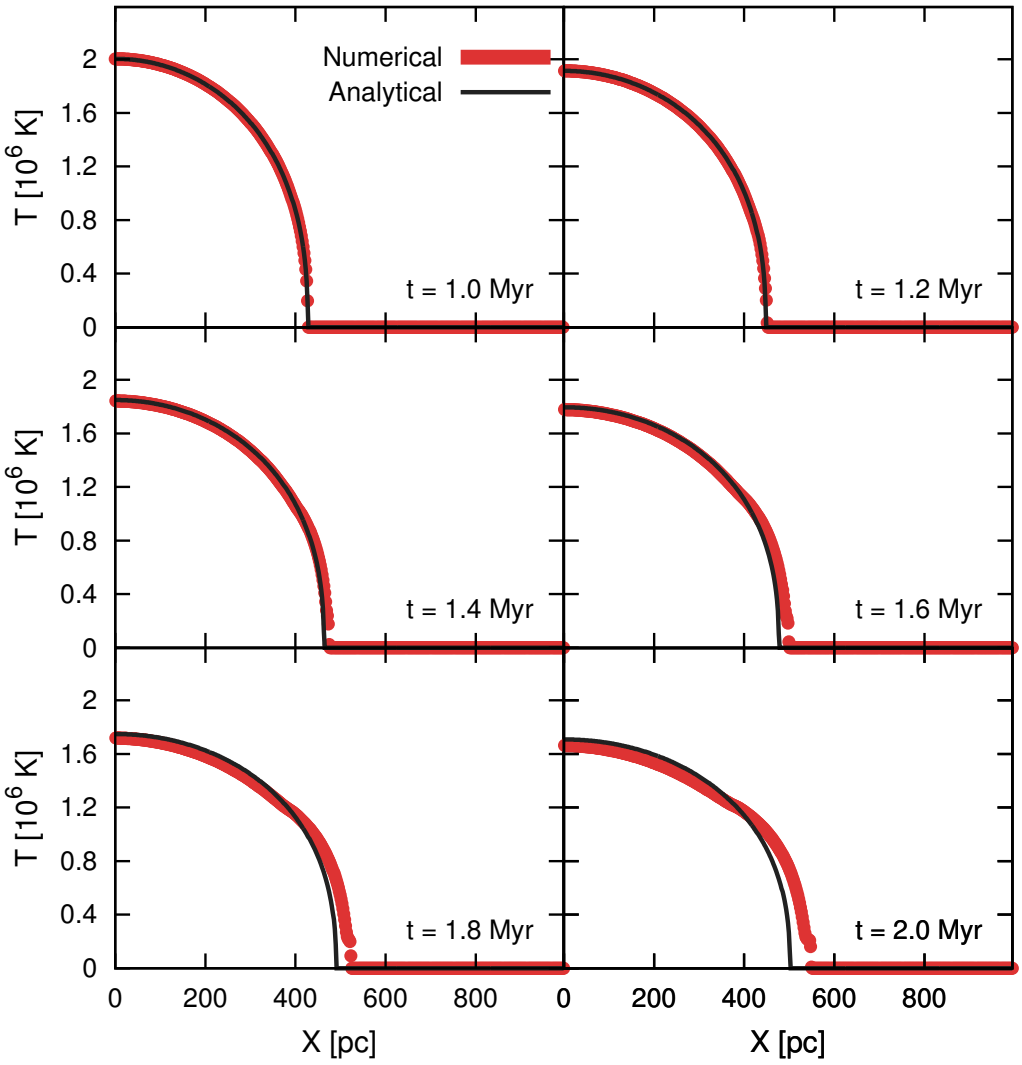

Figure 3.5: Propagation of the conduction front with time including the plasma hydrodynamics. Comparison of the numerical results (red curve) with the analytic solution (black curve), where hydrodynamic is not included.

in its full functionality. Radiative processes were neglected. The initial conditions are the same as in the previous test (pure front conduction). Fig. 3.5 shows the comparison between the numeric solution and the analytic solution, where plasma dynamics is turned off (eq. 3.50,, 3.51 and 3.52).

The numerical solution is able to reproduce the analytic solution up to 1.4 Myr. After 1.4 Myr, the numeric conduction front propagates slightly faster with respect to the analytic solution. This is due to the presence of gas dynamics. Since the initial density distribution of the plasma is uniform, the presence of a hot conduction front causes an overpressure in the regions crossed by the front. As a consequence, a strong pressure wave propagates towards the unperturbed medium, accelerating the plasma motion in the same direction as the conduction front. In Fig. 3.5, the

conduction front passes through ~ 50 pc in 0.4 Myr. The mean propagation speed, v_c, is therefore $\sim 125\,\mathrm{km\,s^{-1}}$, while the mean plasma sound speed, c_s, is $\lesssim 200\,\mathrm{km\,s^{-1}}$ ($T \sim 1.8 \times 10^6$ K). The two velocities are roughly comparable and the initial agreement between the analytic and numerical solution is very good. Decreasing the temperature, the sound speed [$\delta c_s \propto \delta(T^{0.5})$] decreases more slowly than the propagation speed due to pure thermal conduction [$\delta v_c \propto \delta(T^{2.5})$] and a divergence between the analytic and numerical trend with time begins to appear.

Evaporation of a static cold cloud

As a final test, we performed a 2D simulation including hydrodynamics and isotropic thermal conduction in the classical case. Radiative processes were neglected at this stage. The test describes the evolution a cold ($T_{cl} = 10^4$ K) static cloud embedded in an isothermal and uniform plasma with temperature $T_{hot} = 2 \times 10^6$ K and number density $n_{hot} = 10^{-3}$ cm^{-3}. Pressure equilibrium between the two fluids is assumed. The initial radius of the cloud is $R_{cl} = 41$ pc. At the grid boundaries zero-gradient conditions have been set for all hydrodynamical quantities.

Thermal conduction produces a heat flux from the hot plasma to the cold cloud, reducing the temperature gap at the interface between the two fluids. Cowie & McKee (1977) studied the classical evaporation of a spherical cloud in a hot plasma: they derived a time-independent solution for the mass-loss rate, $\dot{m}$, by assuming that the heat transfer occurs at subsonic speeds. However, this solution is not directly applicable to cylindrical clouds. Since our simulation were performed in a 2D geometry, we are effectively simulating an infinite cylinder with initial radius R_{cl}. In order to compare the analytic theory with our 2D numerical results, we modified the time-independent energy equation, derived by Cowie & McKee (1977), as follows:

$$\frac{5}{2}\dot{m}c_s^2 = 2\pi r h \kappa_{Sp}\frac{dT}{dr}\,, \tag{3.53}$$

where c_s^2 is the sound speed and $2\pi rh$ is the lateral surface area of the cylindrical cloud, with r and h respectively the cylinder radius and height.

We integrated eq. 3.53 by setting $T = T_{cl} \simeq 0$ when $R = R_{cl}$ and $T = T_{cor}$ when $R = R_B$, where $R_B = 1$ kpc is the distance between the cloud center and the grid boundary in the computational domain of our simulation. We, indeed, verified that the temperature at the grid boundary remains roughly constant, without decreasing significantly, during the simulated-time span. The mass-loss rate of the cylindrical cloud is then:

$$\dot{m} = \frac{32\pi\mu\kappa_{Sp}h}{75k_B}\ln\frac{R_{cl}}{R_B}\,, \tag{3.54}$$

where k_B is Boltzmann's constant, μ is the mean molecular weight of the plasma and R the cloud radius. In order to make the initial mass of our simulated cylindrical

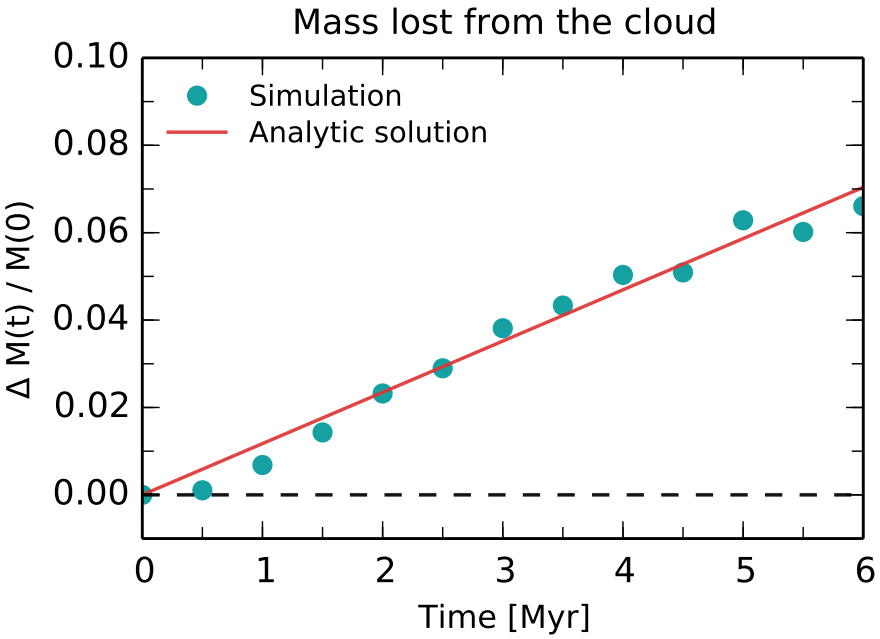

Figure 3.6: Fraction of mass lost from the cloud with time in the evaporation test. The red line indicates the analytic prediction (eq. 3.54) while the cyan points are the results of the simulation. The analytic solution is calculated as $\Delta M(t) \equiv M(0) - M(t) = \dot{m}\Delta t$, being $\dot{m} \sim 2.4 \times 10^{-5}$ $M_\odot$ and the initial mass cloud $M(t = 0) = 2000$ $M_\odot$. In the simulation, the mass lost from the cloud is given by the difference between the initial cloud mass and the mass at $T \leq 10^4$ K (the cloud temperature). The resolution of this simulation is 1.25pcx1.25pc.

cloud equal to the mass of the spherical cloud in the same volume, we fixed the cylinder height h to be $4/3\, R_{\rm cl}$. According to eq. 3.54, the mass-loss rate in our test problem should be $\dot{m} \sim 2.4 \times 10^{-5}$ $M_\odot$ yr^{-1}.

The result of the simulation is compared with the analytic prediction in Fig. 3.6, which shows the mass fraction lost from the cloud with time ($\Delta M(t) \equiv M(0) - M(t) = \dot{m}\Delta t$), being M the mass of gas at $T \leq 10^4$ K. The analytic solution (red line) overlaps very well with the numerical solution (cyan points) during at all times. We stopped the simulation after 6 Myr, when the hot gas temperature at the grid boundaries has decreased from 2×10^6 K to 1.9×10^6 K and the assumption of a constant temperature fails and eq. 3.54 for the loss-mass rate is not We conclude that the agreement between analytic and numerical predictions demonstrate the accuracy of our treatment of thermal conduction.

We also studied the convergence of the code at different grid spacing by carrying out four simulations with different resolution: 10pcx10pc, 5pcx5pc, 2.5pcx2.5pc, 1.25pcx1.25pc. Fig. 3.7 shows the mass lost from the cloud as obtained from these four simulations. The amount of lost mass is systematically higher in the simulations with low resolution, 10pcx10pc and 5pcx5pc, where the effect of numeric diffusion

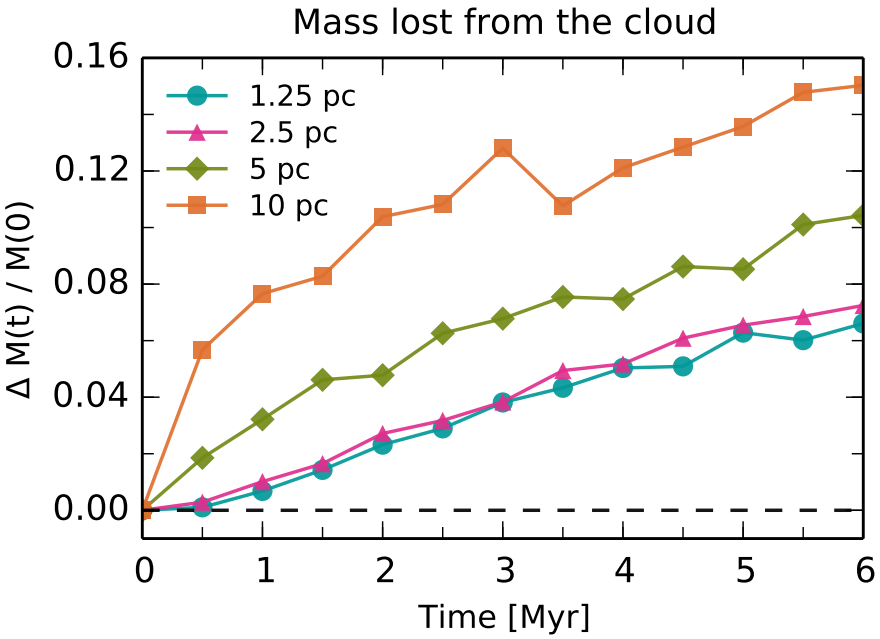

Figure 3.7: Fraction of mass lost from the cloud with time (details in the caption of Fig. 3.6) as a function of the grid resolution. Results are convergent for a resolution larger than 2.5pcx2.5pc.

is dominant. Instead, there is a very good agreement between the simulations with resolution 2.5pcx2.5pc and 1.25pcx1.25pc. This implies that convergence in the results (which we remind also agree with analytic expectations) is reached for a resolution of 2.5pcx2.5pc. In Chapter 4, we show how achieving the convergence of the code becomes harder when radiative processes are also turned on.

Chapter 4

Efficiency of gas cooling and accretion at the disc-corona interface[†]

4.1 Introduction

A long standing problem in the evolution of star-forming galaxies like the Milky Way is how they keep accreting gas from the environment to feed their star formation. The star formation rate of these galaxies has mildly declined throughout their life time ($\sim$ 10 Gigayears) (e.g., Aumer & Binney, 2009; Fraternali & Tomassetti, 2012). In addition, it appears that the neutral gas content of these galaxies has remained approximately unchanged throughout the Hubble time (e.g., Bauermeister, Blitz & Ma, 2010; Zafar et al., 2013). Typically, the mass of gas contained in the thin disc can sustain the process of star formation for a few gigayears only and thus, at any given cosmic epoch, spiral galaxies need some supply of external gas to be brought into the disc, at a rate of $\sim 1\,M_\odot\,yr^{-1}$, that compensates the conversion of gas into stars (e.g Sancisi et al., 2008). This gas should be metal poor to comply with chemical evolution models (e.g., Chiappini, Matteucci & Romano, 2001; Schönrich & Binney, 2009). Cosmological coronae seem to be a significant reservoir of gas that could be accreted by star-forming galaxies to sustain star formation at the

[†]The results of this Chapter have been published in Armillotta, Fraternali, & Marinacci (2016).

observed rates. However, how these hot media can cool from the virial temperature and accrete gas onto the discs is still matter of debate.

There is much observational evidence of a constant interaction between the cold gas in star-forming galaxies and their surrounding coronae. HI observations of star-forming disc galaxies have revealed that $\sim 10\%$ of HI content of these galaxies is located a few kpc above the disc, forming the so-called HI extra-planar layer (e.g., Swaters, Sancisi & van der Hulst, 1997; Fraternali et al., 2002). The kinematics of extra-planar HI is peculiar: its rotational velocity is slower with respect to the neutral gas component of the thin disc and it decreases with increasing height above the galactic plane (e.g., Oosterloo, Fraternali & Sancisi, 2007; Zschaechner et al., 2011). Most of this gas is thought to be composed by fountain clouds, gas ejected from the disc by stellar feedback (Bregman, 1980; Houck & Bregman, 1990), that travels through the halo region and eventually falls back to the disc in a time-scale of $\sim 80-100$ Myr. During this journey, fountain clouds must strongly interact with the galactic corona.

Fraternali & Binney (2008) built a dynamical model of fountain clouds accreting material with lower angular momentum, as a consequence of their interaction with ambient medium and applied it to the extra-planar HI observations of two nearby galaxies, NGC 891 and NGC 2403. This model is able to reproduce the vertical velocity gradient of the extra-planar HI. In order to investigate the physical phenomenon the drives the interaction between the hot corona and the cold fountain clouds, Marinacci et al. (2010, 2011) carried out a set of 2D hydrodynamical simulations of a cold ($T = 10^4$ K) and disc-like metallicity cloud traveling through a hot ($T = 2 \times 10^6$ K) medium. They found that the cold fountain gas and the hot coronal gas mix efficiently in the turbulent wake that forms behind the cloud and this mixing reduces dramatically the cooling time of the hot gas, triggering the condensation and the accretion of a fraction of the corona onto the disc. Marasco, Fraternali & Binney (2012) used the dynamical model of Fraternali & Binney (2008) including condensation from the corona to reproduce the HI halo of the Milky Way. They found a current accretion rate of coronal gas onto the disc of $\sim 2\,\mathrm{M}_\odot\,\mathrm{yr}^{-1}$, in agreement with the accretion rate required to feed that star formation in the Milky Way ($\sim 1-3\,\mathrm{M}_\odot\,\mathrm{yr}^{-1}$, Chomiuk & Povich, 2011; Putman, Peek & Joung, 2012).

Accretion driven by galactic fountains seems to be a viable mechanism for star-forming galaxies to get the gas needed to sustain star formation. However, until now, it has been studied only under conditions representative of our Milky Way today. It becomes crucial to extend the study of the cloud-corona interaction to different galactic environments. In this Chapter we extend the work done by Marinacci et al. (2010, 2011) investigating, through high-resolution hydrodynamical simulations, the cloud-corona interaction for different coronal temperatures. This, given that the coronal temperature is expected to be close to the virial temperature, allows us

to probe a large range of halo virial masses. These new simulations include the presence of thermal conduction, absent in the calculations performed so far. Thermal conduction may be a key process to determine the efficiency of condensation. In fact, it may slow down or, under particular conditions, inhibit the condensation of coronal gas.

This Chapter is organized as follows. In Sec. 4.2 we introduce the set of hydrodynamical simulations performed justifying the choices of the parameters. In Sec. 4.3 we present our simulations results focusing on the efficiency of coronal gas cooling and on the impact of thermal conduction on this process. In Sec. 4.4, we discuss the limitations of these simulations and their implications for galaxy evolution and in Sec. 4.5 we summarize our main results.

4.2 Numerical simulations

Our simulations were performed with the ATHENA code (see Chapter 3) in a two-dimensional cartesian geometry. We performed one three-dimensional simulation (Sim. 11 in Tab. 4.2), discussed in Sec. 4.4.1, in order to estimate the differences between the two geometries. Open boundary conditions were imposed to all the sides of the computational domain.

As in Marinacci et al. (2010, 2011), our simulations model a cold and metal-rich cloud that travels through a hot and static coronal gas with a given initial velocity (the ejection velocity from the galactic disc). The fountain clouds orbit over the disc in the gravitational potential of the galaxy and fall back onto the disc. However, in our simulations both gravitational acceleration and the coronal density variation along the cloud trajectory were neglected. This assumption is justified because, during their orbits, the clouds reach at most heights of few kpc above the galactic plane and their distances from the Galaxy center vary by less than 30% (Fraternali & Binney, 2006; Marasco, Fraternali & Binney, 2012). Therefore, if the corona is in hydrostatic equilibrium with the gravitational potential of the galaxy, the coronal density is not expected to vary much (Marinacci et al., 2011). In Sec. 4.4.2, we present a simulation that includes the vertical gravitational field of the galaxy (Sim. 13 in Tab. 4.2) and we show that the presence of gravity does not significantly modify our results.

For the simulations shown in this Chapter, we only considered the effect of radiative cooling, neglecting any heating process (except for Sim. 12 in Tab. 4.2). We used the prescription of Sutherland & Dopita (1993) in case of collisional ionization equilibrium (CIE, see Sec. 3.4.1).

The parameters fixed in each simulation are listed in Table 4.1. In all simulations the initial cloud temperature is 10^4 K while the initial cloud velocity is $75\,\mathrm{km\,s^{-1}}$. This value represents a typical relative velocity between clouds and corona, being

$T_{\rm cl}$ (K)	$v_{\rm ej}$ (km/s)	$n_{\rm cor}$ (cm^{-3})	$Z_{\rm cor}$ ($Z_\odot$)	$Z_{\rm cl}$ ($Z_\odot$)
10^4	75	10^{-3}	0.1	1.0

Table 4.1: Initial parameters of all our simulations: ejection velocity $v_{\rm ej}$, coronal density $n_{\rm cor}$, cloud temperature $T_{\rm cl}$, coronal metallicity $Z_{\rm cor}$ and cloud metallicity $Z_{\rm cl}$. The cloud density is calculated by assuming pressure equilibrium between the cloud and the corona.

the threshold below which the corona stops absorbing momentum (Marinacci et al., 2011). The coronal particle density is 10^{-3} cm^{-3}. This value may be compared with the total particle density $n = 10^{-4}$ cm^{-3} at 10 kpc above the plane adopted by Heitsch & Putman (2009) or with the average electron density $< n_{\rm e} >= 5 \times 10^{-4}$ cm^{-3} between the disc and 50 kpc above it obtained by Anderson & Bregman (2011). The cloud metallicity is 1.0 $Z_\odot$ while the coronal metallicity is 0.1 $Z_\odot$, in agreement with the values estimated for the galaxies in which the hot halo was actually observed in the X-rays (Bogdán et al., 2013; Hodges-Kluck & Bregman, 2013; Anderson, Churazov & Bregman, 2016). For the Milky Way the value is not well defined but studies through Far Ultraviolet absorption spectra and emission lines of OVII and OVIII return values between 0.1 and 0.3 $Z_\odot$ (Sembach et al., 2003; Miller & Bregman, 2015).

In table 4.2 the parameters that characterize the different simulations are listed: the coronal temperature, the grid resolution, the presence or absence of thermal conduction and its efficiency, the cloud radius. Our main goal is to investigate the cloud-corona interaction and the efficiency of coronal gas condensation in environments with different temperatures. The coronal gas temperature is close to the virial temperature, $T_{\rm vir}$, of the dark matter halo where the galaxy resides:

$$T_{\rm vir} = \frac{G\mu m_{\rm p} M_{\rm vir}}{2 k_{\rm B} r_{\rm vir}} , \tag{4.1}$$

where μ is mean molecular weight of the coronal gas, $m_{\rm p}$ the proton mass, $k_{\rm B}$ the Boltzmann constant, G the gravitational constant and $M_{\rm vir}$ the virial mass. In eq. 4.1, $r_{\rm vir}$ is the virial radius, defined as the radius of a sphere within which the average mass density is $\Delta_{\rm vir}$ times the critical density $\rho_{\rm cr}$ of the Universe:

$$r_{\rm vir} \equiv \left(\frac{3 M_{\rm vir}}{4\pi \, \Delta_{\rm vir} \, \rho_{\rm cr}} \right)^{1/3} . \tag{4.2}$$

$\Delta_{\rm vir}$ is the virial overdensity provided by the dissipationless spherical top-hat collapse, it is a function of the cosmological models, and it may vary with time. For the family of flat cosmologies ($\Omega_{\rm m} + \Omega_\Lambda = 1$), $\Delta_{\rm vir}$ can be approximated by $\Delta_{\rm vir} \simeq 18\pi^2 + 82x - 39x^2/\Omega_{\rm m}(z)$, where $x \equiv \Omega_{\rm m}(z) - 1$ and $\Omega_{\rm m}(z)$ is the ratio of

Sim.	$T_{\rm cor}$ (K)	$M_{\rm cl}$ ($M_\odot$)	$R_{\rm cl}$ (pc)	Res. (pc)	TC	f	Geom.	Heating	Gravity
1	2×10^6	2.4×10^4	100	2	OFF	-	2D	OFF	OFF
2	2×10^6	2.4×10^4	100	2	ON	0.1	2D	OFF	OFF
3	2×10^6	2.4×10^4	100	4	ON	0.1	2D	OFF	OFF
4	2×10^6	2.4×10^4	100	1	ON	0.1	2D	OFF	OFF
5	1×10^6	1.2×10^4	100	2	ON	0.1	2D	OFF	OFF
6	4×10^6	4.8×10^4	100	2	ON	0.1	2D	OFF	OFF
7	8×10^6	9.6×10^4	100	2	ON	0.1	2D	OFF	OFF
8	8×10^6	2.4×10^4	60	2	ON	0.1	2D	OFF	OFF
9	2×10^6	2.4×10^4	100	2	ON	0.2	2D	OFF	OFF
10	2×10^6	2.4×10^4	100	10	ON	0.1	2D	OFF	OFF
11	2×10^6	2.4×10^4	100	10	ON	0.1	3D	OFF	OFF
12	2×10^6	2.4×10^4	100	2	ON	0.1	2D	ON	OFF
13	2×10^6	2.4×10^4	100	2	ON	0.1	2D	OFF	ON

Table 4.2: List of the performed simulations. We varied both the coronal temperature $T_{\rm cor}$ (Sim. 2, 5, 6, 7) and the grid resolution (Sim. 2, 3, 4). The initial cloud radius, $R_{\rm cl}$, is 100 pc in all simulations, expect one where it is 60 pc (Sim. 8). Thermal conduction (TC) is turned off just in one simulation (Sim. 1). In all others, it is turned on with an efficiency of 10% ($f = 0.1$, see Sec. 3.5.1), except one (Sim. 9) with an efficiency of 20% ($f = 0.2$). The simulations were performed in a 2D cartesian geometry, except one (Sim. 11) performed in a 3D geometry. In Sim. 12 and 13 we took into account respectively gas heating from an uniform photoionization background and the presence of the gravitational field of the galaxy.

mean matter density to critical density at redshift z (Bryan & Norman, 1998). In the ΛCDM cosmological model with $\Omega_{\rm m} = 0.3$ the value of $\Delta_{\rm vir}$ is ~ 350 at $z = 0$. Under these assumptions, the coronal temperature is a direct measure of the virial mass of the dark matter halo of the galaxy ($T_{\rm cor} \propto M_{\rm vir}^{2/3}$). Therefore, by changing the coronal temperature in our simulations we are exploring a range of virial masses.

We assumed pressure equilibrium between the cloud and the external medium at the beginning of each simulation. Indeed, we made experiments with out-of-equilibrium initial conditions and we found that the cloud readjusts itself and it reaches pressure equilibrium in ~ 5 Myr. In this way, the cloud number density, that we assumed uniform, is fixed by environmental parameters and it varies in simulations with different coronal temperature: higher coronal temperature means higher cloud density. The initial cloud radius is the same used by Marinacci et al. (2010): it is set at a value of 100 pc in all simulations except in Sim. 8. Then, since the initial radius is fixed, the mass of the cloud changes with the number density between the different setups. In particular, it ranges between 1.2×10^4 $M_\odot$ and 9.6×10^4 $M_\odot$ (see Sim. 2, 5, 6, 7 in Tab. 4.2). These cloud masses are consistent with the estimated masses of the Galactic Intermediate-Velocity Clouds (IVCs) for

which good distance constraints exist (Wakker, 2001). The Jeans mass of a standard cloud ($T_{\rm cl} = 10^4$ K, $R_{\rm cl} = 100$ pc) is 1.6×10^8 $M_\odot$, and so in our simulations the absence of self-gravity is justified.

The hydrodynamical simulations performed by Marinacci et al. (2010, 2011) started with unrealistically spherical clouds. Hydrodynamical simulations of supernovae explosions have indeed shown that the geometry of the gas ejected from the disc is strongly irregular (e.g., Melioli, de Gouveia Dal Pino & Geraissate, 2013). A non-spherical geometry implies a wider contact surface between cloud and corona and, then, a faster and more efficient interaction between them. In order to allow a quick deformation of the spherical cloud and to make the simulations more realistic, we introduced the presence of turbulent motions inside the cloud. We initialized the x-velocity and y-velocity of each cell comprising of the cloud by randomly sampling a gaussian distribution with a given velocity dispersion. For this quantity we used a value of $10\,{\rm km\,s^{-1}}$, in agreement the velocity dispersion, mainly due to turbulence, observed for the HI in our Galaxy and in nearby disc galaxies (Tamburro et al., 2009). To impart a net initial velocity to the cloud, as specified in Table 4.1, we added a bulk velocity of $75\,{\rm km\,s^{-1}}$ to the turbulent velocity field in the x-direction (the cloud's direction of motion).

Since we used a 2D geometry, one of the dimensions perpendicular to the cloud velocity has been suppressed and we are simulating flow around an infinite cylindrical cloud that is moving perpendicular to its long axis. The cylinder initially has a circular cross-section of radius $R_{\rm cl}$. From the simulations we obtained quantities per unit length of the cylinder and we related these to the corresponding quantities for an initially spherical cloud of radius $R_{\rm cl}$ by multiplying the cylindrical results by the length $4R_{\rm cl}/3$ within which the mass of the cylinder equals the mass of the spherical cloud. We calculated the values of the cloud mass in Tab. 4.2 by using this correction.

4.2.1 Thermal Conduction

In Sec. 3.5, we described in detail the analytic theory concerning thermal conduction and its implementation in ATHENA. Despite we chose not to consider the presence of magnetic fields in our simulations, we took into account their impact on the thermal conduction efficiency through the f factor in the heat flux equation 3.35.

According to Narayan & Medvedev (2001) the maximum value that f should have is 0.2. However their analysis is performed on a single plasma phase while our work focuses on the interaction between two different fluids, cloud and corona, with different magnetic fields. At the interface between two fluids with different magnetic fields, thermal conduction can be further reduced due to low efficiency of a phenomenon called 'magnetic reconnection'. The magnetic reconnection breaks

and reconnects magnetic field lines belonging to different fluids. When the process of reconnection is highly efficient, the conducting electrons are able to move and to transfer heat from the hot medium to the cold one. When the process of reconnection is weakly efficient, the conducting electrons tend to remain inside their own fluid and thermal conduction is strongly reduced (e.g., Biskamp, 2000; Priest & Forbes, 2000). In a chaotic magnetic field the role of the magnetic reconnection could be very hard to trace and certainly this goes beyond our current purposes. In order to take into account a possible thermal conduction reduction due to a less efficient magnetic reconnection we fix $f = 0.1$. We judge this to be a good compromise between the upper limit found by Narayan & Medvedev (2001) and a possible effect due to magnetic reconnection at the cloud-corona interface. In Sec. 4.4.1 we also discuss a test (Sim. 9 in Tab. 4.2) with $f = 0.2$. For very high values of the suppression ($f \lesssim 0.01$) the simulations tend to resemble the case without thermal conduction (Sim. 1 in Tab. 4.2).

4.3 Results

Below we describe the main results of our hydrodynamical simulations, focusing on the mass transfer between the cloud and the ambient medium and on the growth of cold gas mass with time. In this Chapter, we are interested in studying the evolution of gas at temperatures below $10^{4.3}$ K. Indeed, under the assumption of CIE, at temperature above $10^{4.3}$ K, the hydrogen is almost completely ionized and the fraction of HI is less than 10% (e.g, Sutherland & Dopita, 1993). Then, we indicate as 'cold gas' only gas at temperatures below $10^{4.3}$ K.

4.3.1 Thermal conduction effects at $T_{cor} = 2 \times 10^6$ K

Fig. 4.3 shows the temperature distribution on our grid after 20, 40 and 60 Myr of the simulations without (left panels) and with (right panels) thermal conduction with $T_{cor} = 2 \times 10^6$ K (Sim. 1 and Sim. 2 in Tab. 4.2). Qualitatively, the evolution of the cloud in the present simulations is similar to that observed in the simulations of Marinacci et al. (2010, 2011). Due to the ram pressure stripping arising from the motion, the cloud feels a drag which causes it to decelerate and to warp. Moreover, the relative motion between cloud and corona produces Kelvin-Helmholtz instabilities at the interface between the two fluids. The cold gas, stripped from the cloud, mixes efficiently with the hot coronal gas in a turbulent wake behind the cloud, where radiative cooling could become effective.

The general evolution of the cloud with and without thermal conduction appears to be quite similar: the two fluids mix creating turbulent wakes behind the cloud. However, by looking at Fig. 4.3, we can note some difference in the shape of the

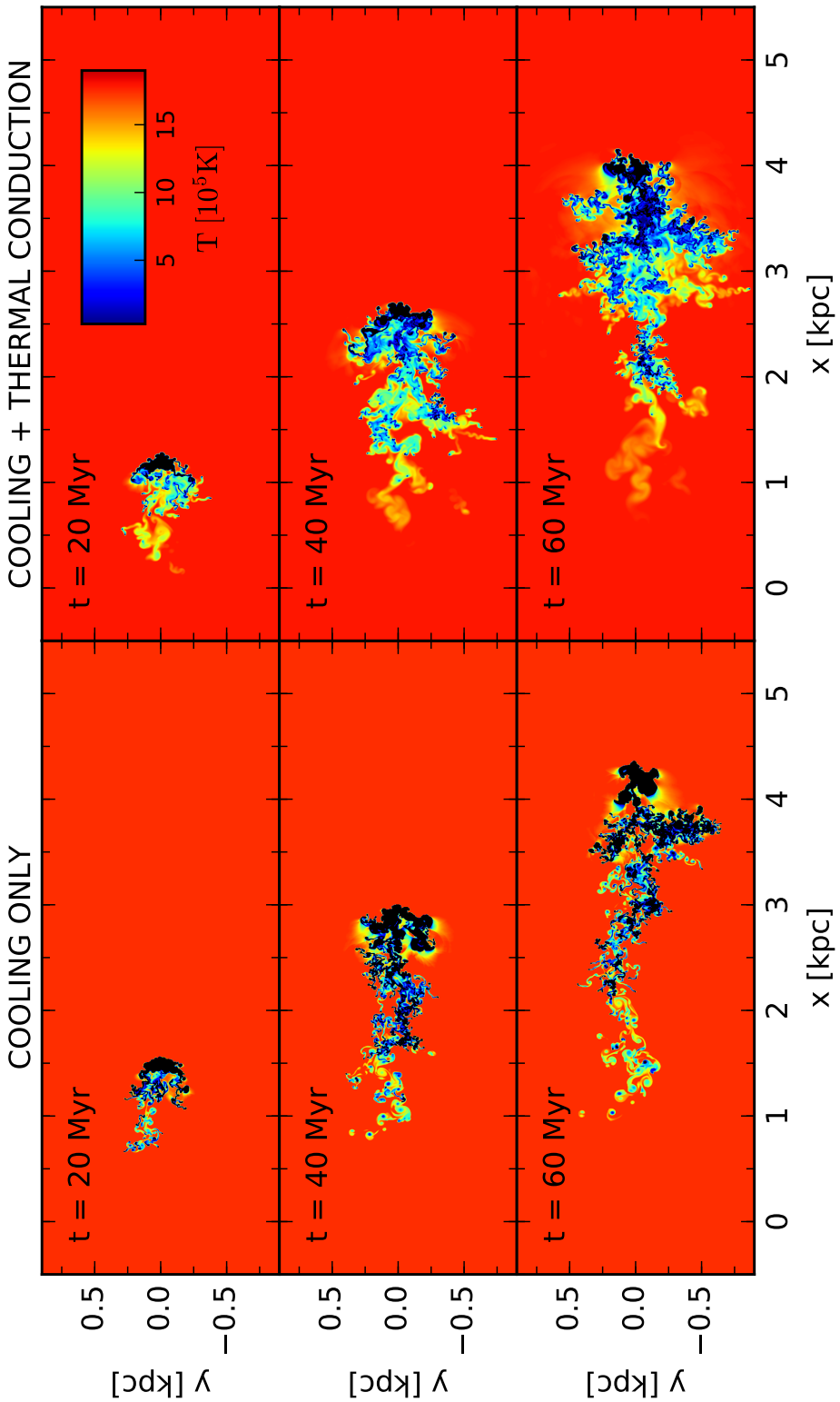

Figure 4.3: Temperature snapshots of the simulations without (left panels) and with (right panels) thermal conduction with $T_{\rm cor} = 2 \times 10^6$ K (Sim. 1 and Sim. 2 in Tab. 4.2). The time at which the snapshots have been taken is indicated in each panel. The initial position of the cloud centre is $x = 0$ and $y = 0$.

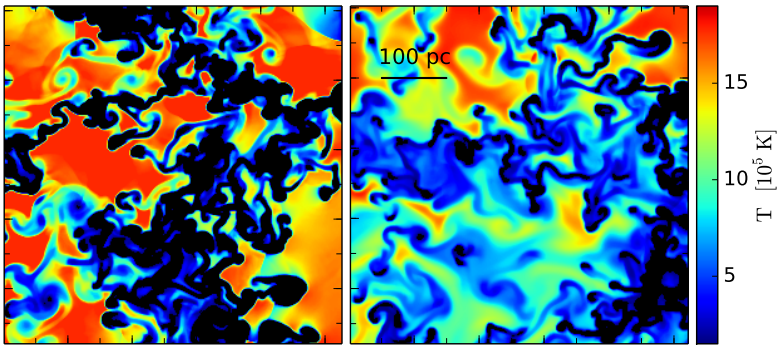

Figure 4.4: Temperature map zoom of a portion of the wake behind the cloud of the simulations with $T_{\rm cor} = 2 \times 10^6$ K without (left panel) and with (right panel) thermal conduction after 60 Myr.

wake, which is less elongated but more laterally extended when thermal conduction is included. Fig. 4.4 shows a magnification of a portion of the wake for both simulations. In the case without thermal conduction (left panel) the wake is composed by numerous cloudlets in which gas is cooling down ($T \lesssim 5 \times 10^5$ K). In the case with thermal conduction (right panel) the wake is composed by a mixture of gas at different temperatures: cold clouds and filaments are embedded in a hotter gas at temperature close to 10^6 K.

Thermal conduction is a diffusive process. Its effect is to create a widespread and warmer wake in which the temperature gradients, due to the presence of colder structures, tend to be smoothed. Therefore, thermal conduction partially hinders the formation and survival of cold cloudlets, consequence of the radiative cooling of the wake.

4.3.2 Condensation of coronal material

The main purpose of this work is to understand under what conditions cold clouds survive and cool down coronal gas during their motion or if they evaporate in the surrounding coronal medium. Thermal conduction can play an important role on gas evaporation or condensation. In Sec. 4.3.1, we saw that thermal conduction tends to smooth the temperature gradients at the interface between different fluids, limiting the efficiency of radiative cooling and preventing the survival of the cold gas.

An analytic criterion to compare the efficiency of cooling and thermal conduction was found by Begelman & McKee (1990). They investigated the evolution of a two-phase medium consisting of clouds embedded in a hot plasma and showed that radiative cooling dominates if the length scales of the relevant structures, l, exceed

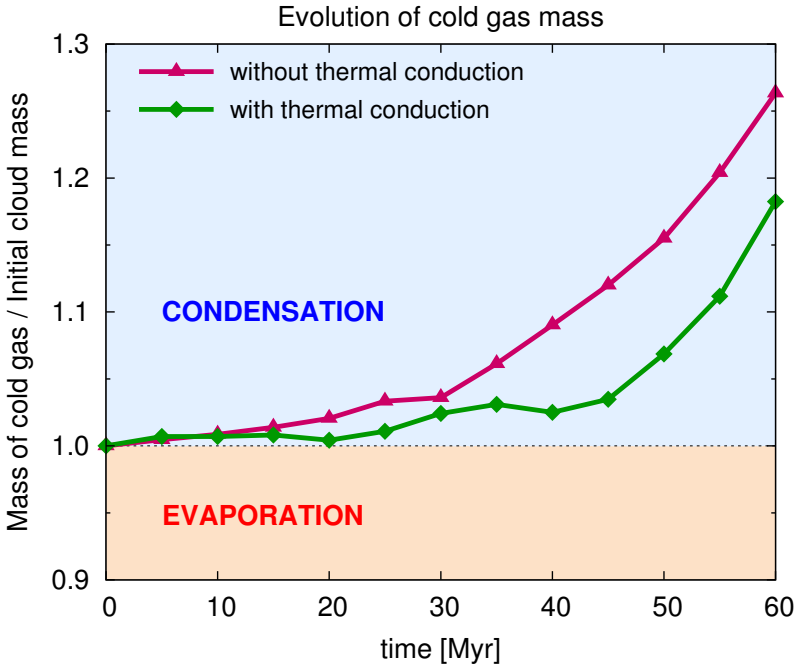

Figure 4.5: Evolution of the mass of cold gas ($T < 10^{4.3}$ K) with time for two simulations with coronal temperature 2×10^6 K : one without thermal conduction and one with thermal conduction (Sim. 1 and Sim. 2 in Tab. 4.2).

a critical length:

$$\lambda_{\rm Field} \equiv \sqrt{\frac{\kappa_{\rm Sp} T_{\rm hot}}{n^2_{\rm cold}\Lambda(T_{\rm cold})}} \ . \tag{4.3}$$

the so-called 'Field length', in view of Field (1965) work on thermal instabilities in astrophysical plasmas, in which he demonstrated that thermal instabilities are suppressed on scales smaller than this characteristic length. In eq. 4.3 $T_{\rm hot}$ is the temperature of the hot plasma and $n_{\rm cold}$ and $\Lambda(T_{\rm cold})$ respectively the numerical density and the cooling rate of the cold gas. The Field length is the maximum length scale on which heat energy transport is effective: for $l \ll \lambda_{\rm Field}$ the temperature distribution of structures that are embedded in the hot plasma is dominated by thermal conduction, while for $l \gg \lambda_{\rm Field}$ thermal conduction is negligible and the temperature evolution is dominated by radiative cooling.

In the simulations showed in Sec. 4.3.1, $T_{\rm cor} = 2\times10^6$ K and $n_{\rm cl} = 0.2$ cm^{-3}, then the Field length is ~ 20 pc[†] . This value is $\sim$ five times smaller than the initial cloud radius (100 pc), therefore a global evolution of the cloud quite similar in the presence or in the absence of thermal conduction is expected. However, the Field length is comparable with the size of cold cloudlets created in the wake (see Fig. 4.4). At this point the fundamental issue is to understand whether these structures evaporate

[†]We used $\Lambda(T_{\rm cold}) = 10^{-23.93}$ ergs cm^3 s^{-1}, that is the average cooling rate in the temperature range between 10^4 K and $10^{4.3}$ K, according to Sutherland & Dopita (1993).

in the mixture or not because the growth of cold gas mass is determined by their survival.

We studied the evolution of mass of the cold gas in the two previous simulations, by extracting the mass of gas at temperatures below $10^{4.3}$ K at different times. Fig. 4.5 shows the quantitative result. Both in the presence and in the absence of thermal conduction the amount of cold gas increases with time, indicating that more and more coronal gas condenses in the wake. The mass profiles become nearly exponential after $\sim$ 30 Myr in the absence of thermal conduction and after $\sim$ 40 Myr in the presence of it. We interpreted this delay as the time required for cold gas, stripped from the cloud, to mix efficiently with the coronal gas plus the time required for the coronal gas to cool to $T \lesssim 10^{4.3}$ K (see also Marasco, Fraternali & Binney, 2012). The latter is longer in the presence of thermal conduction because the process of condensation is hindered. For this reason, the amount of condensation in the absence of thermal conduction is systematically larger: after 60 Myr the amount of cold mass without conduction is $\sim$ 26% of the initial mass of the cloud against $\sim$ 18% with conduction.

We can conclude that thermal conduction slows down the coronal gas condensation but does not inhibit it. Inside the warm wake at temperatures close to 10^6 K, condensation on smaller scales occurs creating cold clouds and filaments. A fraction of these structures is able to survive for a time longer than the simulation time (60 Myr). This results has been obtained with a coronal temperature of 2×10^6 K, obviously the situation could change for different coronal temperatures, as we show in Sec. 4.3.4 and 4.3.5.

4.3.3 Resolution

We studied the convergence of the code at different grid spacing by carrying out three simulations with different resolutions: 4pcx4pc, 2pcx2pc, 1pcx1pc (see Sim. 2, 3, 4 in Tab. 4.2). In Fig. 4.6 we compare the results obtained from these three simulations. The upper panel shows the temporal evolution of the cold gas velocity centroid, defined as the total momentum of the cold gas in the cloud direction of motion divided by the total mass of cold gas. There is a good agreement between all three trends, it seems that even the lower resolution is able to model the slowdown effect of the cloud due both to coronal ram-pressure stripping and to condensation of material that was originally at rest (see Marinacci et al., 2011; Marasco, Fraternali & Binney, 2012, for details).

A different result is found in the lower panel of Fig. 4.6, where we show the mass evolution of cold gas with time. The amount of cold gas in the simulation at lower resolution is systematically higher, while the simulations with intermediate and high resolution have roughly similar mass profiles intersecting one another at

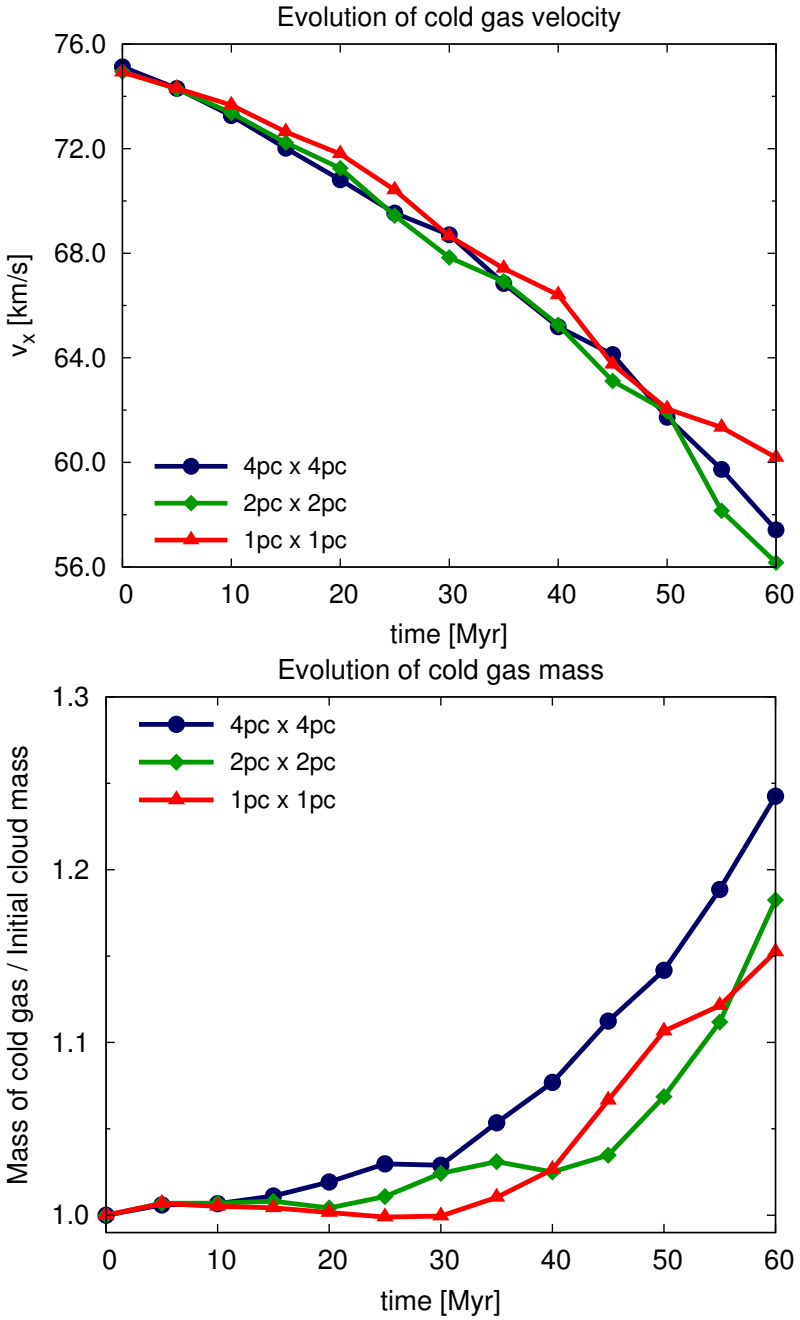

Figure 4.6: Evolution of the velocity (*upper panel*) and of the mass (*lower panel*) of cold gas ($T < 10^{4.3}$ K) with time for three different resolutions when the thermal conduction is switched on (Sim. 2, 3, 4 in Tab. 4.2).

different times and showing a difference not larger than a few percent. Different profiles at different resolutions are related to the evolution of material stripped from the cloud and to its mixing with the coronal gas. As we saw in Fig. 4.3 and Fig. 4.4, the wake of the cloud is composed by small cloudlets and filaments. In a numerical simulation, numerical diffusion truncates this hierarchy of substructures on a scale of a few times the grid resolution: the numerical diffusion tends to smooth temperature gradients so the higher the resolution of the wake, the greater the concentration of the cold material in substructures. Increased resolution inhibits the phase mixing and the subsequent coronal gas condensation. Therefore, in simulations with radiative cooling but without any physical diffusive processes (e.g. thermal conduction), it is very difficult to reach convergence between results at different resolutions: the higher the resolution, the lower the amount of condensation.

It appears that the introduction of thermal conduction has been helpful to restrain the effect of numerical diffusion. As we said in Sec. 4.3.1, thermal conduction is a diffusive process: like numerical diffusion, it destroys the smaller structures smoothing the temperature gradients and creating a homogeneous mixture at intermediate temperature. However, unlike numerical diffusion, the scale at which thermal conduction operates does not depend on the grid resolution, but on physical conditions of the problem, in particular on the temperature of the hot coronal gas (see eq. 3.31 and 3.32). Thus, although at very low resolutions numerical diffusion is the dominant diffusive process, increasing the resolution, thermal conduction can become the dominant process. The development of turbulence in the wake of our fountain clouds produces a hierarchy of smaller and smaller structures, following a power law distribution. The size of the smallest structures is determined by resolution, however their survival is largely determined by thermal conduction which operates efficiently on scales below the Field length ($\sim$ 20 pc). Therefore, the smallest clouds (a few parsec) do not influence the growth of cold gas mass because they are not able to survive, mix with hotter gas and trigger condensation. The convergence in condensation shown in Fig. 4.6 may reflect this change of regime.

After these considerations we can conclude that the resolution 2pcx2pc is good enough for our kind of simulations and we proceed with this resolution for the rest of the Chapter.

4.3.4 Thermal conduction effects at different T_{cor}

Thermal conduction strongly depends on the temperature of the hot gas. The heat conduction flux, $\boldsymbol{q}$, is proportional to $T^{5/2}$ (see eq. 3.32), then small differences of temperature lead to large differences of exchanged heat. The consequence is that at high temperatures cold structures can evaporate much faster. However, as we saw in Sec. 3.5, when the temperature changes on scales smaller than the mean free path of the conducting electrons, thermal conduction enters in a regime of saturation and

the correlation between high temperatures and high heat transfer can be mitigated. A criterion to ascertain the effects of saturated thermal conduction on a structure with length scale l is given by the global saturation parameter:

$$\sigma_0 = \left(\frac{T_{\rm cor}}{1.54 \times 10^7}\right)^2 \frac{f}{\Phi_{\rm s} n_{\rm cor} l_{\rm [pc]}} \,. \tag{4.4}$$

For $\sigma_0 \gtrsim 1$ the effect of saturated thermal conduction becomes significant (Cowie & McKee, 1977; Dalton & Balbus, 1993). In our simulations, the effect of saturation is negligible for the global evolution of the cloud: $\sigma_0 \ll 1$ for $l = R_{\rm cl} = 100$ pc, regardless of coronal temperature. However, the saturation effect on the cold cloudlets in the turbulent wake could become more and more important ($\sigma_0 \propto l^{-1}$) for increasing coronal temperature. Indeed, at $T_{\rm cor} = 8 \times 10^6$ K $\sigma_0 \lesssim 1$ and at these high temperatures the saturation effect could have some influence on the general cloud evolution.

We investigated the evolution of cold clouds in coronae at different temperatures and we found that it is closely related to the importance of thermal conduction at a given temperature. Fig. 4.7 shows the temperature distribution on the grid after 20, 40 and 60 Myr for the simulations with with $T_{\rm cor} = 10^6$ K (left panels) and with $T_{\rm cor} = 8 \times 10^6$ K (right panels) in the presence of thermal conduction (respectively Sim. 5 and Sim. 7 in Tab. 4.2). The general evolution of the cloud is very different in the two cases. In the simulation with $T_{\rm cor} = 10^6$ K the situation is quite similar to the case analysed in Sec. 4.3.1, with $T_{\rm cor} = 2 \times 10^6$ K (see right panel in Fig. 4.3). The cold gas, stripped from the cloud, mixes with the hot coronal gas in the turbulent wake behind the cloud. The wake is composed by large amount of gas at temperature below 2×10^5 K, indicating a very effective radiative cooling. Instead, in the simulation with $T_{\rm cor} = 8 \times 10^6$ K the cloud nearly behaves like a rigid body. The turbulent wake does not exist, with the consequence that the mixing between the two fluids is absent.

It is important to point out that at $T_{\rm cor} = 10^6$ K the Field length is ~ 10 pc, while at $T_{\rm cor} = 8 \times 10^6$ K it is ~ 70 pc (see eq. 4.3), a value comparable with the initial cloud radius (100 pc). Therefore, while at low temperatures thermal conduction affects only the cold cloudlets in the turbulent wake (see also Sec. 4.3.1), at high temperature it can influence the global motion of the cloud. The effect of thermal conduction is to smooth the temperature gradients at the interface between the two fluids, creating a transition region at intermediate temperatures (this is clearly visible in the right panels in Fig. 4.7). The temperature smoothing leads the cloud to lose momentum at the contact surface. The resulting absence of a strong velocity gradient prevents the formation of hydrodynamical instabilities at the cloud-corona interface, implying very long destruction times for the cloud (see also Vieser & Hensler, 2007b). The main consequence of this phenomenon is the

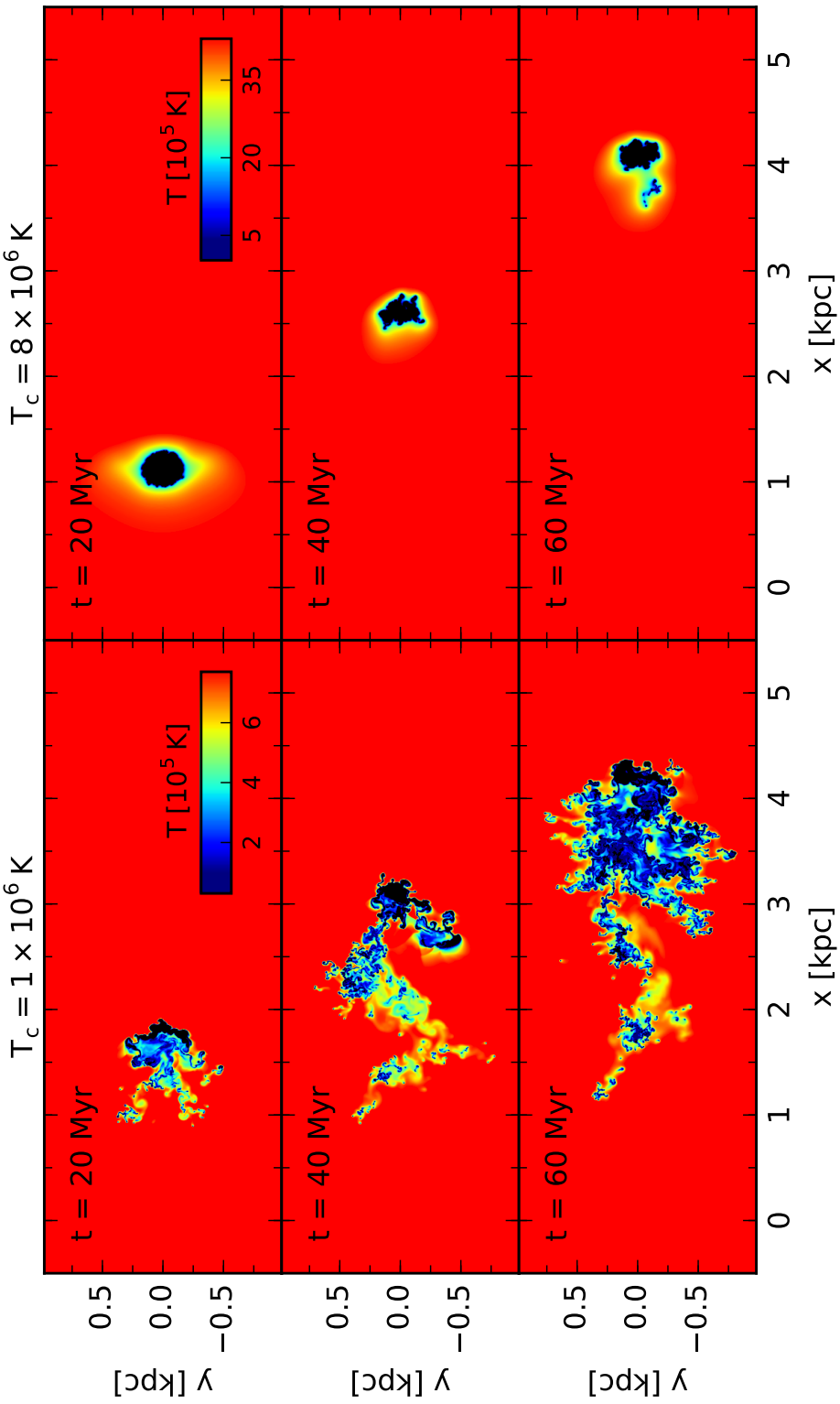

Figure 4.7: Temperature snapshots of the simulations with $T_{\rm cor} = 10^6$ K (left panels) and with $T_{\rm cor} = 8 \times 10^6$ K (right panels) in the presence of thermal conduction (Sim. 5 and Sim. 7 in Tab. 4.2). The time at which the snapshots have been taken is indicated in each panel. The initial position of the cloud centre is $x = 0$ and $y = 0$.

delay or the lack of the mixing phase between cloud and corona.

At $T_{\rm cor} = 8 \times 10^6$ K, the initial cloud mass is 9.6×10^4 $M_\odot$, the largest value that we explored in our simulations. In addition to thermal conduction, an inefficient coronal ram pressure could contribute to the slow destruction of massive clouds: large masses imply a large drag time ($t_{\rm drag} \propto M_{\rm cl}^{1/3}$, Fraternali & Binney, 2006) and, then, a less efficient coronal ram pressure. In order to understand which of these two phenomena dominate at $T_{\rm cor} = 8 \times 10^6$ K, we performed a simulation with a cloud four times less massive and a radius almost two times smaller, $M_{\rm cl} = 2.4 \times 10^4$ $M_\odot$ and $R_{\rm cl} = 60$ pc (see Sim. 8 in Tab. 4.2). We found that the cloud evolution does not change significantly with respect to the standard simulation with a larger and more massive cloud: the cold gas remains in a compact configuration at the cloud head and the turbulent wake is absent. Then, we conclude that the strong effect of thermal conduction at $T_{\rm cor} = 8 \times 10^6$ K drives the cloud evolution, regardless of its own initial mass and size.

4.3.5 Condensation at different $T_{\rm cor}$

In order to understand how the galactic environment influences the coronal gas condensation, we analyzed the evolution of mass of cold gas with time in four simulations with different coronal temperatures, $1 \times 10^6, 2 \times 10^6, 4 \times 10^6$ and 8×10^6 K (respectively Sim. 5, 2, 6 and 7 in Tab. 4.2). Fig. 4.8 shows the results in the presence of thermal conduction. The amount of condensation becomes less efficient for increasing coronal temperature. After 60 Myr the mass of condensed gas is $\sim 30\%$ of the initial mass of the cloud for $T_{\rm cor} = 1 \times 10^6$ K, $\sim 18\%$ for $T_{\rm cor} = 2 \times 10^6$ K, $\sim 4\%$ for $T_{\rm cor} = 4 \times 10^6$ K and less than 1% for $T_{\rm cor} = 8 \times 10^6$ K.

In our simulations, the cloud temperature is fixed ($T_{\rm cl} = 10^4$ K), therefore, higher coronal temperature means higher mixture temperature and, then, longer cooling times. For this range of temperatures the shape of the cooling function is crucial (see Sutherland & Dopita, 1993). At $T \sim 10^6$ K a rising or falling of the temperature could have a great impact on the cooling time. In coronae with temperatures much larger than 2×10^6 K, the turbulent wake does not reach temperature low enough to trigger an exponential increase of condensation.

Thermal conduction can also play an important role in the different coronal gas condensation at different temperatures. The higher the coronal temperature, the more efficient the thermal conduction. As we show in Sec. 4.3.1 and 4.3.4, thermal conduction has two important effects. It smooths the velocity gradient at the cloud-corona interface, making the cloud more compact and preventing the formation of hydrodynamical instabilities and subsequent mixing. This phenomenon causes a very slow cloud destruction (see Sec. 4.3.4). The second effect is that once the gas is stripped from the cloud, thermal conduction changes its role, accelerating the

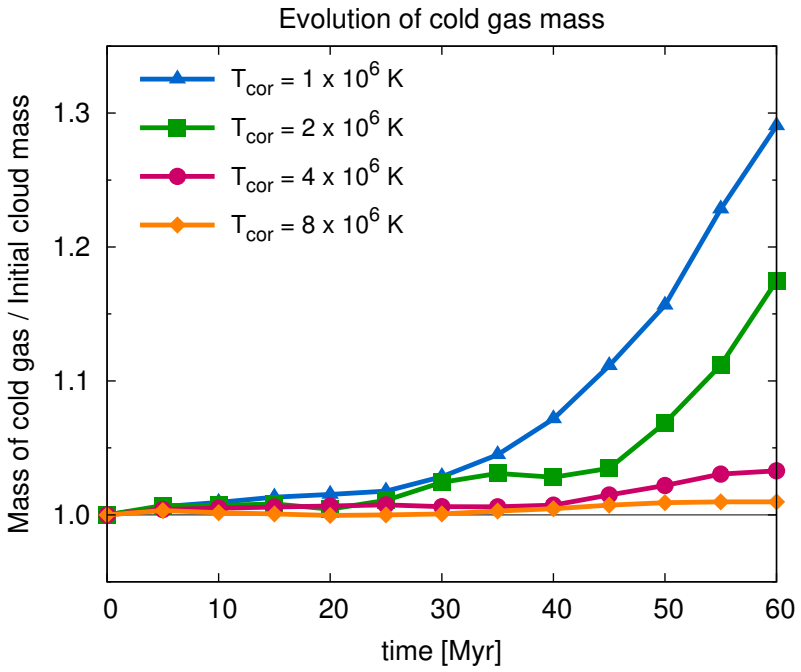

Figure 4.8: Evolution of the mass of cold gas ($T < 10^{4.3}$ K) with time for four different values of coronal temperature: $1 \times 10^6, 2 \times 10^6, 4 \times 10^6$ and 8×10^6 K (respectively Sim. 5, 2, 6, 7 in Tab. 4.2).

heating of the cold gas and its evaporation in the coronal medium (see Sec 4.3.1).

We note that at $T_{\rm cor} > 4 \times 10^6$ K the evolution of the cold mass is nearly flat. This means that the cold cloud does not acquire coronal gas and, at the same time, it does not lose its own mass. In this regime the cloud radius is comparable with the Field length (see Sec. 4.3.4), therefore the effect of radiative cooling is still important although not dominant.. Moreover, in Sim. 8 (see Tab. 4.2), where the cloud radius is slightly smaller than the Field length, the equilibrium between thermal conduction and radiative cooling is evident. In this case the amount of cold mass decreases at a very slow rate: at the end of the simulation the cloud has lost $\sim 1\%$ of its own initial mass. At higher temperature the radiative cooling is likely to become ineffective, leading the cloud evaporation in the coronal medium.

4.4 Discussion

4.4.1 Limitations of our results

We discuss physical and numerical issues that can affect our estimates about the growth of the cold gas mass during the simulation.

All our simulations were performed in a two-dimensional cartesian geometry. In order to estimate the limitations of the two-dimensional geometry, we performed one

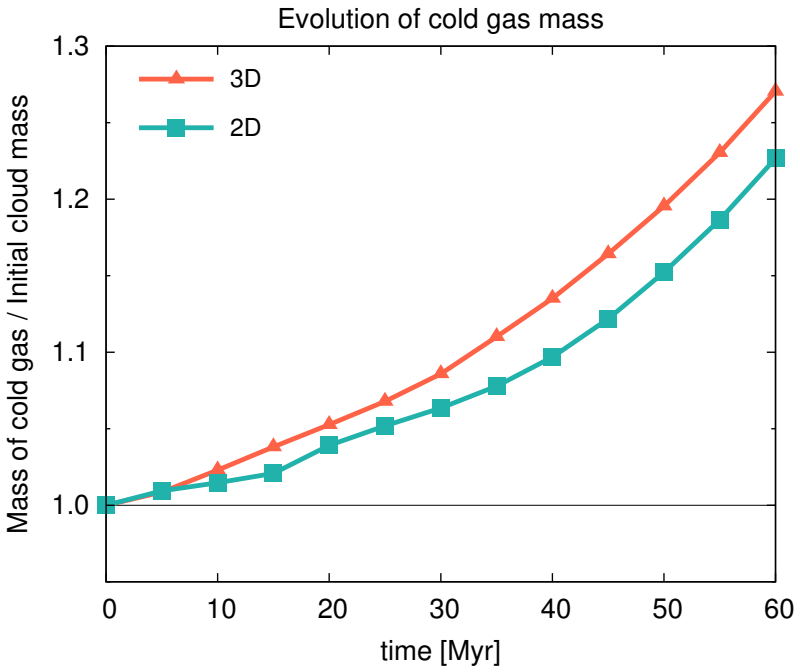

Figure 4.9: Evolution of mass of cold gas ($T < 10^{4.3}$ K) with time for two simulations, one in 3D and one in 2D cartesian geometry (Sim. 10 and Sim. 11 in Tab. 4.2).

three-dimensional simulation at low resolution, 10pcx10pc (higher resolutions would have imply very long computational times for a code with static grid, as ATHENA). In Fig. 4.9 we compare the results obtained using the two different geometries, and in particular the evolution of the mass of cold gas with time. The two simulations were performed with the same initial parameters and the same grid resolution (Sim. 10 and Sim. 11 in Tab. 4.2). The amount of cold gas increases with time in both simulations, it increases faster in the 3D case but the difference is not large. After 60 Myr the fraction of condensed mass is $\sim 27\%$ of the initial mass of the cloud in the 3D case, $\sim 23\%$ in the 2D case. The nature of the cloud-corona interaction is different in 2D and 3D simulations. In 2D we simulate an infinite cylinder that is moving perpendicular to its long axis, while in 3D we actually simulate a spherical cloud. The result is that in 3D the contact surface between the two fluids is larger leading to additional developments of hydrodynamical instabilities and a more rapid phase mixing between the cold gas, stripped from the cloud, and the coronal gas. This result is in agreement with recent works that studied the differences between the two geometries through the evolution of a spherical cloud in a hotter and shocked medium (Pittard & Parkin, 2016). In conclusion, we can expect that the 2D geometry slightly underestimates the growth of the cold gas mass.

The efficiency of magnetic field in suppressing thermal conduction, that we quantified through the factor f (see Sec. 3.5.1), can also affect our findings. We remind that, according to Narayan & Medvedev (2001), in the presence of a tangled

magnetic field the efficiency of the Spitzer thermal conduction is reduced to 20% ($f = 0.2$). However, for reasons that we explained in Sec. 4.2.1, we preferred to use $f = 0.1$ in our simulations. We then performed a simulation with $f = 0.2$ (Sim. 9 in Tab. 4.2). The parameters of this simulation are the same of the simulations discussed in Sec. 4.3.2, with $T_{\rm cor} = 2 \times 10^6$ K. We found that after 60 Myr the amount of cold gas is $\sim 9\%$ of the initial mass of the cloud for $f = 0.2$, while it is $\sim 18\%$ for $f = 0.1$. Thus, the difference of a factor 2 in thermal conduction efficiency corresponds to a difference of a factor 2 in amount of condensation. The value of $\sim 9\%$ represents a lower limit of the condensation that we can obtain by varying the efficiency of thermal conduction through f. The upper limit is instead given by the simulation in the absence of thermal conduction, that corresponds to assume $f = 0$. In this case the amount of cold gas is $\sim 25\%$ of the initial mass. We conclude that in the interval of possible values of f the process of condensation always occurs and the amount of accreting cold gas anticorrelates with the efficiency of thermal conduction.

Heating processes, like photoionization by background sources or by the star-forming disc, were neglected in our simulations. The effect of heating would be to render our estimates as upper limit, since it slows down the cooling process. In Fig. 4.10, we show a preliminary result (Sim. 12 in Tab. 4.2) obtained by including photoionization from a uniform UV background at $z = 0$ (Haardt & Madau, 2012, see Sec. 3.4.2 for theory and implementation in ATHENA) in Sim. 2 (Tab. 4.2). We compare the evolution of the mass of cold gas with time in the presence and in the absence of photoionization. Note that both simulations were run for 70 Myr, in order to better evaluate the relative effects of cooling and heating. The amount of cold gas increases in both simulations, indicating that condensation of coronal gas can occur also in the presence of heating by background sources. However, according to our expectations, the condensation process is slowed down by photoionization: the amount of cold gas slightly decreases (3% at 35 Myr) before that its exponential growth begins. After 70 Myr the amount of cold mass is $\sim 20\%$ of the initial mass cloud against $\sim 27\%$ in the absence of photoionization.

In Sec. 3.4, we discussed how the presence of photoionization from a uniform UV background affects cooling rates depending on total gas temperature, metallicity and hydrogen density. In case of collisional ionization equilibrium (see Fig. 3.1), at fixed metallicity radiative cooling rates depend mainly on the gas temperature, then, once the gas in the turbulent wake reaches values of temperature close to the peak of the cooling function, the process of condensation starts with an exponential trend (see Sec. 4.3.2). Instead, in the presence of heating photoionization (see Fig. 3.3), the net cooling rates (cooling rates minus heating rates) strongly depend on the gas density: the lower the density the more efficient the heating process. Therefore, the gas density in the wake must become high enough for the cooling process to begin

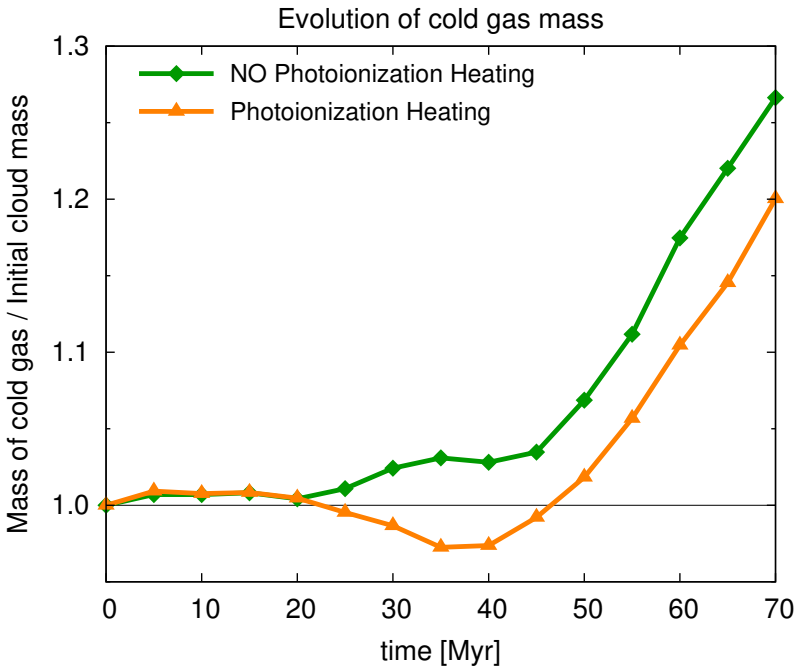

Figure 4.10: Evolution of the mass of cold gas ($T < 10^{4.3}$ K) with time for two simulations, one in the presence and one in the absence of photoionizing background (Sim. 12 and Sim. 2 in Tab. 4.2).

efficiently. After 30-40 Myr, in the innermost regions of the wake (Sim. 2), turbulent mixing increases the coronal density by almost two order of magnitude, from $\sim 10^{-3}$ cm^{-3} to $\sim 10^{-1}$ cm^{-3}. At this density, radiative heating does not significantly alter the shape of cooling function (see Fig. 3.3) and condensation can start, as shown in Fig. 4.10. We conclude that, in our simulations, the main effect of a photoionizing UV background is likely a delay in the time of the start of the condensation.

At this stage, we neglected radiation coming from star-forming disc in our photoionization model. Fountain clouds orbit within ~ 2 kpc above galactic discs (see Sec. 4.4.2) and the effect of stellar radiation could be important. We point out that heating by stellar radiation varies along the orbit of the fountain cloud as a function of its distance from the star-forming region. Therefore, hydrodynamical simulations need to be performed in the presence of the gravitational field of the galaxy, in order to account for the heating effect at different distances from the galactic plane. Further investigations are required to test this effect.

4.4.2 Simulations including gravity

The simulations presented in Sec. 4.2 and 4.3 were performed by neglecting the gravitational field of the galaxy. In order to check whether the cold gas in the turbulent wake follows the motion of the fountain cloud until back to disc, we performed a simulation in the presence of gravity.

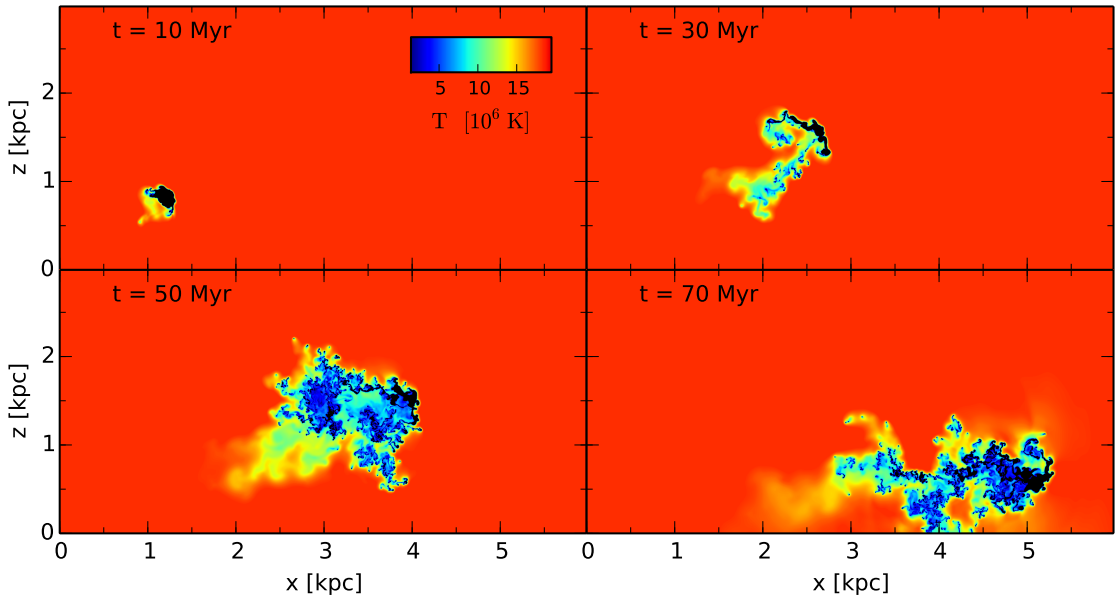

Figure 4.11: Temperature snapshots of the simulation that includes the vertical gravitational field of the Galaxy (Sim. 13 in Tab. 4.2). The initial velocity components along the x- and z-axis are respectively $70\,\mathrm{km\,s^{-1}}$ and $75\,\mathrm{km\,s^{-1}}$. The time at which the snapshots have been taken is indicated in each panel. The initial position of the cloud centre is at $x = 0.5$ kpc and $z = 0.2$ kpc.

Fig. 4.11 shows temperature snapshots of a simulation (Sim. 13 in Tab. 4.2) of cloud-corona interaction in the presence of the vertical gravitational field of our own Galaxy at the solar circle ($R_\odot = 8.5$ kpc) (Model II in Binney & Tremaine, 2008). The cloud is ejected from nearly the Galactic plane ($z = 0.2$ kpc) with a vertical velocity (velocity along the z-axis in Fig. 4.11) of 70 $\mathrm{km\,s^{-1}}$, which is the typical ejection velocity of a fountain cloud (Marasco, Fraternali & Binney, 2012). We assumed that the azimuthal motion of the cloud occurs along the x-axis, with an azimuthal velocity is 75 $\mathrm{km\,s^{-1}}$, roughly the relative rotation velocity between the Galactic corona and the disc at the solar circle (Marinacci et al., 2011). The coronal gas, with number density $n_{\mathrm{cor}} = 10^{-3}$ $\mathrm{cm^{-3}}$ at $z = 0$ kpc, is in hydrostatic equilibrium with the vertical gravitational field of the Milky Way. From the figure, we can note that the orbital time of the cloud is ~ 70 Myr. After this time, cold coronal gas in the turbulent wake falls onto the disc (bottom side of the computational domain) together with the fragments of the initial cloud.

In Fig. 4.12, we compare the evolution of the mass of cold gas with time in the presence and in the absence of gravity. The exponential evolution of the condensation process starts slightly later in the presence of gravity (after ~ 50 Myr). However, at the end of its orbit, the fountain cloud has cooled down an amount of coronal gas equal to 25% of its own mass, against $\sim 27\%$ in the absence of gravity. The initial disagreement between the two trends can be explained by the differ-

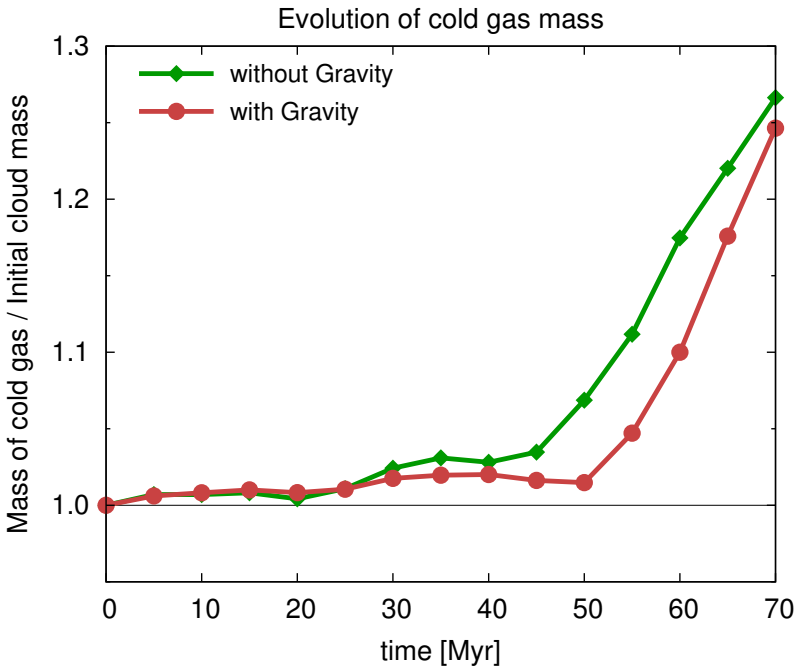

Figure 4.12: Evolution of the mass of cold gas ($T < 10^{4.3}$ K) with time for two simulations, one in the presence (magenta line) and one in the absence of a vertical gravitational field (green line)(Sim. 13 and Sim. 2 in Tab. 4.2).

ent initial velocity of the cloud. It is $75\,\mathrm{km\,s^{-1}}$ in the absence of gravity, while it is $\sim 100\,\mathrm{km\,s^{-1}}$ in the presence of gravity. Higher velocities entail more efficient coronal ram-pressure stripping and, then, a more destructive effect on the cloud. However, during the first half of the orbital time, the vertical velocity of the cloud quickly decreases due to gravity, thus balancing the initial destructive effect. Most of the corona condensation seems to take place in the descending part of the orbit when the cold gas rains down to the disc.

We conclude that the presence of gravity does not alter our results: both the overall cloud evolution and the amount of condensation after an orbital time are in good agreement.

4.4.3 Implications for gas accretion in disc galaxies

Star-forming galaxies like the Milky Way need some supply of external gas to feed star formation at the observed rate of $\sim 1\,\mathrm{M_\odot\,yr^{-1}}$ (see Sec. 4.1). There are strong indications from cosmological models that the gas accreted by these galaxies to form stars must come from the intergalactic medium, which accumulates around galaxies in the form of hot coronae. Hence, the evolution of a star-forming galaxy is strongly influenced by the flows of gas between the galaxy and its surrounding environment.

Our simulations show that the hot coronal gas can be efficiently cooled by the

interaction with cold and metal-rich fountain gas at the disc-corona interface. Coronal gas condenses into a turbulent wake behind the cloud becoming fresh material that may sustain star formation at the current observed rates. However, the amount of coronal condensation strongly depends on the galactic environment as it becomes less efficient for increasing coronal temperature. The Milky Way coronal temperature is $\sim 2 \times 10^6$ K (Fukugita & Peebles, 2006; Miller & Bregman, 2015). In environments with this coronal temperature, the coronal gas condensation is efficient: after 60 Myr our cloud with initial mass $2.4 \times 10^4\,M_\odot$ condenses an amount of coronal gas equal to $\sim 18\%$ of its own mass (see Sec. 4.3.1 and 4.3.4).

Both model and observations show that the coronal temperature of a galaxy is roughly its virial temperature, which in turn is a measure of the virial mass of the dark matter halo where the galaxy resides. Using equations 4.1 and 4.2, we related the coronal temperature of our simulations to the virial mass of the galaxy. Coronal temperatures of 10^6 K correspond to virial masses of $\sim 10^{12}$ $M_\odot$, coronal temperatures of 8×10^6 K correspond to a virial masses larger than $10^{13}\,M_\odot$. The virial mass corresponding to 2×10^6 K is $\sim 3 \times 10^{12}$ $M_\odot$, slightly higher than the virial mass estimated for the Milky Way ($\sim 2 \times 10^{12}$ $M_\odot$, e.g., Li & White, 2008). We note however that the observations of the Milky Way corona are quite sensitive to the coronal medium close to the disc where feedback may cause slight departures from the virial temperature (e.g., Strickland et al., 2004).

Our simulations have shown that the ability of fountain clouds to cool their surrounding corona is very efficient in galaxies with coronal temperature $\lesssim 2\times10^6$ K / virial mass $\lesssim 3\times10^{12}$ $M_\odot$, drops significantly for galaxies with coronal temperature $\gtrsim 4 \times 10^6$ K / virial mass $\gtrsim 8 \times 10^{12}$ $M_\odot$, and it is totally absent in galaxies with coronal temperature larger than $\gtrsim 8 \times 10^6$ K / virial mass $\gtrsim 10^{13}$ $M_\odot$. Thus, there appears to be a mass threshold (3×10^{12} $M_\odot \lesssim M_{\rm vir} \lesssim 8 \times 10^{12}$ $M_\odot$) beyond which the cooling and accretion of the corona is not viable.

Schawinski et al. (2014) showed that star-forming galaxies are mostly in haloes with low virial masses, while disc galaxies located in the green valley region, between the blue cloud of star-forming galaxies and the red sequence of quiescent galaxies in the colour-mass diagram, are almost exclusively galaxies with high virial masses, typically larger than $10^{12}\,M_\odot/h$, where $h = H_0/100$ km s^{-1} Mpc^{-1} is the Hubble parameter. Green valley galaxies are objects that are moving off or have already left the main sequence of star formation (e.g., Brinchmann et al., 2004; Peng et al., 2010; Schawinski et al., 2014). Since all star-forming galaxies are on the main sequence and since green-valley galaxies must have experienced star formation in the past, by definition some process has turned off star formation but, to date, the ways this quenching of the star formation occurs is still matter of debate. In terms of the Hubble fork, the disc galaxies with the lowest ratio between the current and the past SFRs are early-type disc galaxies, near the S0/Sa locus (e.g., Boselli et al.,

2001). Then, while late-type disc galaxies are undergoing a current phase of star formation, early-type disc galaxies have experienced a decline of star formation in response of exhaustion of gas reservoir. Milky Way galaxies, with virial mass close to the mass limit between the blue cloud and the green valley region are still forming stars at slowly declining rates.

Recent theoretical works showed that haloes below a critical shock-heating mass, $M_{\rm shock} \sim 2-3\times10^{11}$ M$_\odot$, enjoy gas supply by cosmological cold streams (*cold mode* accretion), not heated by a virial shock, and form stars, while the cold gas accretion is turned-off above this mass (e.g., Dekel & Birnboim, 2006; Kereš et al., 2009). According to these works, the shut off of gas supply prevents further star formation, leading the galaxies to evolve passively from the blue cloud to the red sequence as consequence of the depletion of the gas reservoir. However, as we said previously, Milky Way galaxies, with $M > M_{\rm shock}$, are still forming stars and mechanisms able to feed the star formation are needed.

The mechanism of coronal condensation driven by fountain clouds we proposed seems to suggest a suitable solution for explaining the presence of galaxies with $M > M_{\rm shock}$ on the main sequence of star formation. We note that our model does not exclude but it integrates the quenching mechanism due to the turning-off of *cold mode* accretion. Our study shows that the coronal gas cools down efficiently in galaxies with low-intermediate virial masses but the ability of the galaxy to cool their corona decrease going from late-type to early-type disc galaxies, inhibiting accretion of cold gas available for star formation and leading potentially to the quenching of the star formation. Moreover, given that the condensation is the consequence of mixing between the corona and the cold disc gas, it follows that early-type galaxies of any virial mass must be inefficient in cooling their corona because they have much less cold gas (e.g., Catinella et al., 2010).

Our results therefore suggest that the turn-off of the star formation in massive disc galaxies may be due not only to heating mechanisms of the hot halo, such as AGN (e.g., Dubois et al., 2012) or stellar thermal feedback (e.g., Stinson et al., 2013), but also to the inability to cool their own coronal material experienced by massive galaxies ($M_{\rm vir} > 3\times10^{12}$ M$_\odot$). We can also speculate that our mechanism could explain both the quenching processes identified by Peng et al. (2010): the stellar-mass and the environmental quenching. Indeed, the only effect that determines the star-formation quenching in our model is the ambient temperature. This correlates both with the stellar mass (or the halo mass) of the galaxies (as mentioned), at least for isolated galaxies (Behroozi, Wechsler & Conroy, 2013; Moster, Naab & White, 2013), and with the kind of environment the galaxies live in. For example, dense environments, as galaxy clusters, are characterized by high virial temperatures. In these environments, not only the massive galaxies but also the late-type disc galaxies would not be able to cool the ambient medium, thus leading to the quenching of

their star formation.

4.5 Summary and conclusions

Cold gaseous discs of spiral galaxies are embedded in extended hot coronae of virial-temperature gas ($T \gtrsim 10^6$ K) that may contain a significant fraction of the so-called missing baryons. Milky Way-like galaxies might sustain their star formation at the current observed rates by transferring gas from the corona to the star-forming disc. In the region at the disc-corona interface there is a continuous interaction between the galaxy and its surrounding corona: cold fountain clouds ($T \sim 10^4$ K), ejected from the disc by stellar feedback, travel through the hot coronal gas and interact with it. Marinacci et al. (2010, 2011), through hydrodynamical simulations, studied the physical phenomenon the drives this interaction in an environment representative of our own Milky Way. They found that the cold fountain gas and the hot coronal gas mix efficiently and this mixing reduces dramatically the cooling time of the hot gas, triggering the condensation and the accretion of a fraction of the corona onto the disc. This new fresh coronal gas could become gas available for the star formation.

In this work, we extended the work done by Marinacci et al. (2010, 2011) investigating, through high-resolution hydrodynamical simulations, the cloud-corona interaction in environments with different coronal temperatures. The new simulations were performed in the presence of radiative cooling and isotropic thermal conduction, the latter absent in the previous works. From these simulations we can draw the following conclusions.

- At $T_{\rm cor} \lesssim 2 \times 10^6$ K, formation of hydrodynamical instabilities at the interface cloud-corona triggers the loss of cold gas from the cloud. This gas mixes significantly with the hot coronal material in a turbulent wake, where radiative cooling is effective and forms cold gas cloudlets. The effect of thermal conduction is to prevent the survival of these cold structures by creating a warmer wake with smoothed temperature gradients. Nevertheless, thermal conduction is not able to inhibit the coronal gas condensation: after $\sim 30 - 40$ Myr, the latter starts with a trend nearly exponential and, after 60 Myr, the amount of cold gas is $\gtrsim 18\%$ of the initial cloud mass.

- At higher coronal temperatures ($T_{\rm cor} \gtrsim 4 \times 10^6$ K), the effect of thermal conduction is to smooth the velocity gradient at the interface between the cloud and corona, preventing the formation of hydrodynamical instabilities and the subsequent cloud destruction. This phenomenon makes the cloud more compact and hinders the mixing phase between the two fluids.

- The amount of coronal condensation strongly depends on the environment temperature as it becomes less efficient for increasing coronal temperature.

This trend is due to the combined effect of radiative cooling, that dominates at low coronal temperatures, and thermal conduction, that increases its efficiency at high coronal temperatures.

Since the coronal temperature correlates with the virial mass of the dark matter halo where galaxy resides, it appears that the ability of a galaxy to cool its own corona decreases for increasing the halo mass: it is high for $M_{\rm vir} \lesssim 3{\times}10^{12}$ $\mathrm{M}_{\odot}$, while it drops significantly for $M_{\rm vir} \gtrsim 8 \times 10^{12}$ $\mathrm{M}_{\odot}$. We speculate that coronal condensation driven by interaction between fountain clouds and hot coronal gas could have important implications for galaxy evolution. It could have been a viable mechanism to sustain the star formation in Milky Way-like galaxies after the turn-off of the *cold mode* accretion. At the same time, its drop in efficiency for increasing ambient temperature could provide a possible explanation for both mass and environment quenching of the star formation.

Chapter 5

Survival of gas clouds in the Circumgalactic Medium of Milky Way-like galaxies[†]

5.1 Introduction

As discussed in Chapter 1, several pieces of evidence have shown the presence of multiphase gas in the halo regions of low-redshift galaxies. In this Section, we summarize the main properties of the multiphase halo gas, in order to introduce the work presented in this Chapter.

The presence of a diffuse and hot phase of the circumgalactic medium is predicted by current cosmological theories. Low-redshift galaxies are expected to be surrounded by hot coronae at the virial temperature ($T \gtrsim 10^6$ K, Fukugita & Peebles, 2006), extending out to hundreds of kpc from the galaxy center. Unfortunately the X-ray surface brightness of these coronae is rather faint, limiting their possibility of detection (Bregman, 2007). In the Milky Way most of the evidence of the existence of a hot corona collected over the last decades has been indirect: the head-tail structure of several high velocity clouds (HVCs, Putman, Saul & Mets, 2011), the asymmetry of the Magellanic Stream (MS, Mastropietro et al., 2005) and

[†]The results contained in this Chapter have been submitted to MNRAS as Armillotta, Werk, Prochaska, Fraternali, & Marinacci (2016).

the loss of external gas in the dwarf spheroidal galaxies of the Local Group (Grcevich & Putman, 2009; Gatto et al., 2013; Salem et al., 2015) may all be explained by ram-pressure exerted by the coronal medium. Recently, the presence of a hot corona around our Galaxy was also detected through OVII and OVIII absorption lines in quasar spectra and emission lines in the soft X-ray background (Miller & Bregman, 2015). Haloes of hot gas have also been observed around some massive spiral galaxies. In these cases X-ray emission has been detected at more than 50 kpc from the center, indicating the presence of extended structures. Once extrapolated to the virial radius, the mass of these coronae is comparable with the mass of the baryonic discs of these galaxies ($\sim 10^{11}$ $M_{\odot}$) (e.g., Dai et al., 2012; Bogdán et al., 2013; Anderson, Churazov & Bregman, 2016).

Regarding the colder phase of the CGM, HI observations in the Milky Way revealed a population of HVCs, characterized by velocities inconsistent with the rotation of the Galactic disc, generally at distances of $\sim 5-10$ kpc from the Galactic disc (e.g Wakker & van Woerden, 1997; Wakker et al., 2007), except for the Magellanic Stream (MS), situated in the interval at $\sim 50-200$ kpc from the disc (Putman, Peek & Joung, 2012). Furthermore, a significant fraction of these HVCs exhibits OVI absorptions (e.g., Sembach et al., 2003; Fox et al., 2004) indicating the presence of a more highly ionized and hotter medium at 10^{5-6} K, likely at the interface between the HVCs and the corona. In recent years, lines of different ions (CII, CIII, CVI, SiII, SiIII, SiVI), probing low ionization state material at $T \sim 10^{4-5}$ K, have been observed in absorption towards extragalactic sources in the Milky Way's halo (e.g., Shull et al., 2009; Lehner & Howk, 2011). They fill about $70-90\%$ of the sky and are often associated with the neutral gas emission from HVCs (e.g., Lehner et al., 2012).

HI clouds have been observed around the discs of some nearby spiral galaxies. The detected clouds are generally close to the host galaxy, within $\sim 10-20$ kpc above the galactic plane (e.g., NGC 891 Oosterloo, Fraternali & Sancisi, 2007). High-sensitivity observations around M 31 have shown evidence for HI clouds out to distances $\gtrsim 50$ kpc from the disc (e.g., Lewis et al., 2013). However, several of these clouds are potentially the result of an interaction between M 31 and its companion galaxy, M 33.

Recently, the COS-Halos survey has constrained the physical properties of the CGM in nearby galaxies (e.g., Werk et al., 2012; Tumlinson et al., 2013), detecting gas through absorption lines of different ions (CII, CIII, MgII, SiII, SiIII) against background QSO spectra for a sample of galaxies in the low-redshift ($0.1 < z < 0.35$) Universe. A large fraction of the sample galaxies, regardless of their type, have shown both Lyα absorbers and strong column densities of low/intermediate ionization elements (CII, CIII, MgII, SiII, SiIII) out to projected distances of 150 kpc from the centre, probing the presence of a cold and predominantly ionized circumgalactic

phase ($T < 10^5$ K, Tumlinson et al., 2013; Werk et al., 2013). Detections of highly ionized material (e.g., OVI), corresponding to a warm gas phase ($T \sim 10^{5-6}$ K), have also been reported out to the same distances as the cold absorbers (Tumlinson et al., 2011; Werk et al., 2014).

The study presented in this Chapter aims to shed light on the coexistence and the ubiquity of different gas phases in the CGM, and, in particular, to understand under what conditions the cold gas can survive in the hot corona. Our working hypothesis is that the observed cold/warm and ionized phase is associated with the interaction and mixing between the hot coronal medium and a colder neutral phase. The mechanism originating this cold phase can be various: for instance, the same that generated the Milky Way's HVCs (see Chapter 2 for an extensive discussion), gas streams due to tidal/ram pressure stripping (e.g. the MS) or, potentially, clouds ejected by powerful outflows (e.g. the HVC toward the Large Magellanic Cloud, Barger, Lehner & Howk, 2016). In this Chapter, we do not investigate the origin of the cold clouds but focus on the problem of their survival. In Sec. 5.2 we introduce the set of hydrodynamical simulations performed justifying the choices of the parameters and we briefly describe the main features of the code that we used. In Sec. 5.3 we present the results of our simulations and we compare them with the COS-Halos observations. In Sec. 5.4 we discuss our simulations by referring to other numerical works investigating the survival of cold clouds, while in Sec. 5.5 we summarize our main results.

5.2 Hydrodynamical simulations

We performed a suite of two-dimensional hydrodynamical simulations of cold neutral clouds ($T = 10^4$ K) travelling through a hot and low-density coronal medium at given initial velocities. As seen in the previous chapters, Kelvin-Helmholtz instabilities tear up the cold cloud during its motion, generating a long turbulent wake where cloud and corona materials mix and produce gas at intermediate temperature. This gas mixture may evaporate in the surrounding hot medium or, if radiative cooling is effective, condensate in colder and smaller structures (see Sec. 4.3 and Marinacci et al., 2010).

The main goal of the present simulations is to understand, by sampling different cloud sizes and velocities, whether the cold gas may survive its journey through the coronal medium. As done in Chapter 4, when we refer to the cold gas, we take into account both the cold gas belonging to the cloud, and the cold gas present in the turbulent wake.

The parameters fixed in each simulation are listed in Table 5.1. In all simulations the parameters of the coronal medium were chosen assuming the typical properties of the Milky Way at large distances from the galactic disc ($50 - 150$ kpc, following

$T_{\rm cor}$ (K)	$n_{\rm cor}$ ($\rm cm^{-3}$)	$Z_{\rm cor}$ ($\rm Z_\odot$)	$T_{\rm cl}$ (K)	$n_{\rm cl}$ ($\rm cm^{-3}$)	$Z_{\rm cl}$ ($\rm Z_\odot$)
2×10^6	10^{-4}	0.1	10^4	2×10^{-2}	0.3

Table 5.1: Initial parameters of all our simulations: coronal temperature $T_{\rm cor}$, coronal density $n_{\rm cor}$, coronal metallicity $Z_{\rm cor}$, cloud temperature $T_{\rm cl}$, cloud density $n_{\rm cl}$, cloud metallicity $Z_{\rm cl}$.

the observed impact parameters of the COS-Halos survey). The coronal temperature was set to 2×10^6 K, roughly the coronal temperature of the Milky Way (Fukugita & Peebles, 2006; Miller & Bregman, 2015), while the coronal metallicity was set to 0.1 $\rm Z_\odot$, according to the value estimated for those galaxies in which the hot halo was actually observed in X-rays (Bogdán et al., 2013; Hodges-Kluck & Bregman, 2013; Anderson, Churazov & Bregman, 2016). For the Milky Way the value is not well constrained, but studies through both Far Ultraviolet absorption spectra and emission lines of OVII and OVIII returned values between 0.1 and 0.3 $\rm Z_\odot$ (Sembach et al., 2003; Miller & Bregman, 2015). We assumed a coronal number density of 10^{-4} $\rm cm^{-3}$, this value is compatible with the coronal number density of $1.3 - 3.6 \times 10^{-4}$ $\rm cm^{-3}$ in the range $50 - 90$ kpc from the galactic disc found by Gatto et al. (2013), the average value of $\sim 2 \times 10^{-4}$ $\rm cm^{-3}$ within 100 kpc found by Grcevich & Putman (2009) and the upper limit of $\sim 10^{-4}$ $\rm cm^{-3}$ found by Besla et al. (2012) by reconciling simulations of MS formation and observations. We assumed pressure equilibrium between the cloud and the external medium. Our numerical experiments have indeed shown that if the cloud is initially out of pressure equilibrium with the ambient medium it readjusts itself and it reaches pressure equilibrium in a few Myr. With this prescription the cloud number density is fixed by environmental parameters to 2×10^{-2} $\rm cm^{-3}$. The cloud metallicity was fixed to be the same in all simulations. Its value is 0.3 $\rm Z_\odot$, in agreement with the metallicities measured for most high-velocity complexes in the Milky Way, usually between 0.1 and 0.5 $\rm Z_\odot$ (e.g., Wakker, 2001), and with the typical metallicity of the Magellanic Clouds (Hunter et al., 2009).

The only two parameters changing in our set of simulations are the initial cloud velocity with respect to the hot gas, $v_{\rm cl}$, and the initial cloud radius, $R_{\rm cl}$. Our goal is to investigate how these two physical quantities influence the cloud survival. We assumed three different values for the initial velocity, 100, 200 and 300 $\rm km\,s^{-1}$. These values are compatible with the results found by Tumlinson et al. (2013) and Werk et al. (2013): the material detected by the COS-Halos observations is within approximately $\pm 200\,\rm km\,s^{-1}$ of the galaxy systemic velocity. This range also encompasses the typical circular velocity of Milky Way halo (e.g., Lux et al., 2013). The values chosen for the initial radius of the cloud are 50, 100, 250 and 500 pc, corresponding to cloud masses of 1.6×10^2, 1.3×10^3, 2×10^4 and 1.6×10^5 $\rm M_\odot$, respectively. The estimated masses of most of the Milky Way's HVCs, for which good distance

constraints exist, lie in a range of higher masses, between 10^5 and $5 \times 10^6\,M_\odot$ (See Sec. 1.1.1 and Putman, Peek & Joung, 2012). However, these complexes are always composed by smaller clouds (Thom et al., 2008; Hsu et al., 2011), then the masses which we chose for our simulations are fully justified. Also the MS shows clear evidence for a hierarchy of structures, in the form of cloudlets around the main filaments of the Stream (Putman et al., 2003; Fox et al., 2014). The same cloud sizes are observed around external galaxies, in particular M 31 (Thilker et al., 2004).

In our simulations the clouds are initially spherical. As mentioned in the previous chapters, this assumption is unrealistic because the geometry of the HI clouds around our Galaxy is strongly irregular (e.g., Putman, Peek & Joung, 2012). In order to make our simulations more realistic, we allowed for a quick breakdown of the sphericity and homogeneity of the cloud by introducing internal random motions inside it. Both in most Milky-Way's HVCs and in the MS, the typical velocity dispersion observed for the gas phase at $T \lesssim 10^4$ K is $\sim 12\,\mathrm{km\,s^{-1}}$ (e.g., Kalberla & Haud, 2006). This dispersion is mainly due to turbulent motions, rather than to thermal broadening. We introduced turbulence inside the cloud both along the x-axis and the y-axis: the initial velocity inside the cloud follows a gaussian distribution with dispersion $10\,\mathrm{km\,s^{-1}}$ for both the axes and mean value $0\,\mathrm{km\,s^{-1}}$ for the y-axis and the initial cloud velocity, $v_{\rm cl}$, for the x-axis, which is the cloud direction of motion (see also Sec. 4.2).

5.2.1 The numerical scheme

All simulations were performed with the ATHENA code (Stone et al., 2008), using a two-dimensional Cartesian geometry with fixed grid. The 2D geometry suppresses one of the dimensions perpendicular to the cloud velocity and it results in simulating an infinite cylinder that is moving perpendicular to its long axis. From the simulations we obtained quantities per unit length of the cylinder, then, to relate these to the corresponding quantities for an initially spherical cloud of radius $R_{\rm cl}$, we multiplied the cylindrical results by the length $4R_{\rm cl}/3$ within which the mass of the cylinder equals the mass of the spherical cloud. We used this correction to calculate the gas mass below a given temperature for all the simulations presented in this work (see also Sec. 4.2 and Marinacci et al., 2010).

We implemented an algorithm to make the grid adaptive and moving, in order to follow the cloud along its motion. This is necessary in order to reduce the size of the computational domain and the time needed to run the simulations. After every Myr the algorithm repositions the cloud's head at the grid centre. Open boundary conditions were imposed at the four sides of the simulation domain. The spatial resolution is 2pc×2pc. Our results on the study of the code convergence showed that this resolution appear to be optimal for limiting divergence problems related to numerical diffusion (see Sec. 4.3.3 for details).

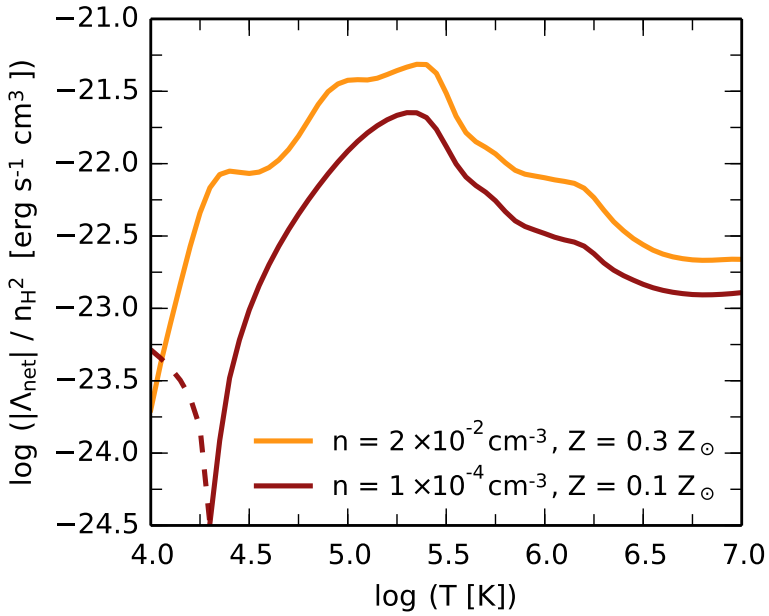

Figure 5.2: Absolute value of net cooling/heating rate as a function of gas temperature for $n = 2 \times 10^{-2}$ cm^{-3} and $Z = 0.3$ $Z_{\odot}$ (orange line) and $n = 10^{-4}$ cm^{-3} and $Z = 0.1$ Z$_{\odot}$ (brown line). We plot the absolute value of the radiative cooling minus the photoheating rate per unit volume, divided by $n_{\rm H}^2$. We use a dashed line to indicate that, at the lowest gas density and metallicity, heating dominates over cooling for $T < 10^{4.3}$ K.

We did not take into account gravitational acceleration and coronal density variation along the cloud motion. Including a gravitational field is indeed beyond our current purposes. We were interested to study the average environmental effects on the cloud survival so we did not specify its trajectory (outflow or inflow) or its exact location in the circumgalactic halo. Furthermore, we neglected the cloud self-gravity: the Jeans mass of a standard cloud ($T_{\rm cl} = 10^4$ K, $n_{\rm cl} = 2 \times 10^{-2}$ cm^{-3}) is $\sim 10^9$ M$_{\odot}$, so self-gravity in our simulations is totally negligible.

We included both thermal conduction (Sec. 3.5) and radiative cooling/heating (Sec. 3.4 and 3.4.2) in our simulations. As in Chapter 4, we assumed that the efficiency of thermal conduction is reduced to 10% by magnetic fields (see Sec. 4.2.1 for details). To calculate cooling an heating rates, we evaluated the effect of photoionization from a uniform UV background at $z = 0.2$ (the average redshift of the COS-Halos sample of galaxies), accounting for the UV radiation emitted by all stars and AGN throughout the evolution of the Universe and attenuated by the Lyα forest (Haardt & Madau, 2012). Collisional ionization of all atoms and ions is also included in the model.

Fig. 5.2 shows the net cooling/heating rates as a function of temperature in the logarithmic scale for two extremest values present in our simulations, one with density and metallicity of the cloud ($n = 2 \times 10^{-2}$ cm^{-3} and $Z = 0.3$ $Z_{\odot}$) and

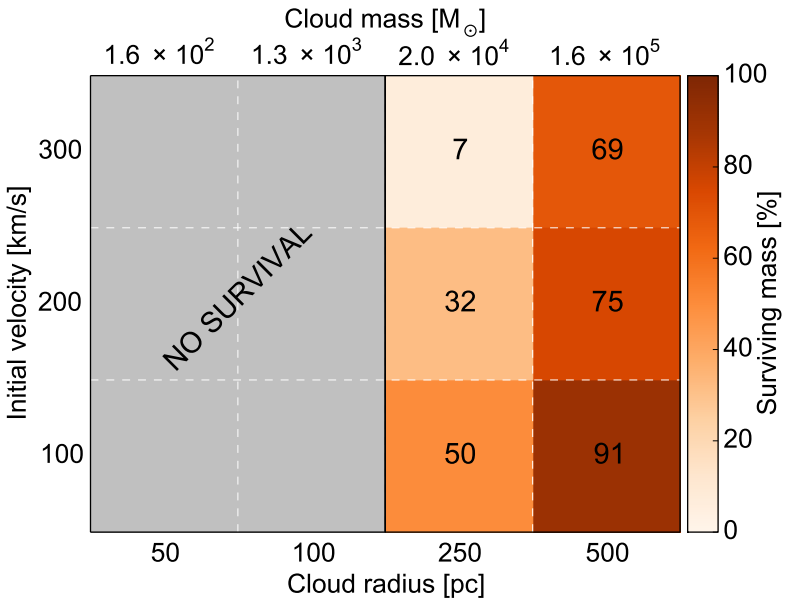

Figure 5.3: Parameter space (radius-velocity-mass) explored in our simulations to test cold gas survival for 250 Myr. The number written in each square and the color bar indicate the percentage of cold gas (T $< 10^5$ K) that survives. The grey band represents the range of parameters in which the cloud is not able to survive.

the other with density and metallicity of the coronal medium ($n = 10^{-4}$ cm^{-3} and $Z = 0.1$ Z$_\odot$). Most of our cells falls typically within these values. At $T \sim 10^{4.3}$ K the curve at low density and metallicity show a discontinuity, below which heating dominates over cooling (dotted line).

5.3 Results

We run our simulations of cold clouds interacting with the surrounding coronal gas for 250 Myr. We found that the mass of cold gas decreases with time in all the performed simulations. The cold gas, stripped from the cloud by hydrodynamical instabilities, mixes with the coronal gas in a turbulent wake, however, in all the analyzed cases, the wake density is not high enough to allow for gas condensation (unlike the simulations shown in Sec. 4.4.1), and most of cold gas lost from the cloud evaporates in the hot coronal medium. However, in several cases, a consistent fraction of cold gas survives until the end of the simulation: most of this gas resides inside the cloud head and only a very small fraction is located in the wake, as we show in Sec 5.3.1.

Fig. 5.3 shows the values of initial radius and velocity of the cloud that allow the cold gas ($T < 10^5$ K) survival for at least 250 Myr, and the fraction of gas able to survive after this time. Clouds with radius equal to or less than 100 pc

are entirely destroyed after 250 Myr. Clouds with radius equal to 250 pc are able to survive. However, the fraction of surviving mass strongly depends on the initial cloud velocity, decreasing with increasing velocity. The cloud with $v_{\rm cl} = 100\,{\rm km\,s^{-1}}$ is able to keep $\sim 50\%$ of its own initial mass after 250 Myr, while the cloud with $v_{\rm cl} = 300\,{\rm km\,s^{-1}}$ retains only $\sim 7\%$. The situation changes completely for larger clouds ($R_{\rm cl} = 500$ pc): a significant fraction of cold gas survives ($\gtrsim 70\%$) and its dependence on the initial velocity becomes rather weak.

A key issue in this analysis is the efficiency of coronal ram pressure to warp the cloud, triggering its ablation. The coronal flow flattens the cloud perpendicularly to the motion direction, increasing its cross section. The resulting shear flow over the leading face of the cloud causes the formation of Kelvin-Helmholtz instabilities at the cloud-corona boundary and the subsequent cloud ablation. Therefore, the time scale associated to the cloud survival is strongly related to time scale associated to ram pressure exerted on the cloud by the coronal medium, the so-called drag time (Fraternali & Binney, 2006):

$$t_{\rm drag} = \frac{M_{\rm cl}}{v_{\rm cl}\sigma\rho_{\rm cor}}\ , \tag{5.1}$$

where $\sigma \simeq \pi {R_{\rm cl}}^2$ is the cross section of the cloud. The drag time increases with increasing cloud size ($t_{\rm drag} \propto M_{\rm cl}/\sigma \propto R_{\rm cl}$) and decreases with increasing cloud velocity. The effect of coronal ram pressure on the largest clouds is very weak and they are able to survive for very long times.

The velocity can also play an important role. Fig. 5.3 shows that the fraction of surviving mass decreases with increasing velocity for the clouds with $R_{\rm cl} = 250$ pc and for the clouds with $R_{\rm cl} = 500$ pc and $v_{\rm cl} = 100\,{\rm km\,s^{-1}}$ and $200\,{\rm km\,s^{-1}}$. A dependence on the velocity is instead roughly absent for the cloud with $R_{\rm cl} = 500$ pc and $v_{\rm cl} \geqslant 200\,{\rm km\,s^{-1}}$. The cloud with $v_{\rm cl} = 300\,{\rm km\,s^{-1}}$ keeps $\sim 70\%$ of its own initial mass, while the cloud with $v_{\rm cl} = 200\,{\rm km\,s^{-1}}$ keeps $\sim 75\%$, a small difference. In this last case the velocity is supersonic (the sound speed is $\sim 200\,{\rm km\,s^{-1}}$ at $T = 2 \times 10^6$ K) and the radius is large enough to keep the velocities supersonic for almost the entire simulation time. In fact, in our simulations the cloud velocity evolves with time approximately as (Fraternali & Binney, 2006):

$$v_{\rm cl}(t) \simeq \frac{v_{\rm cl}(0)}{1 + t/t_{\rm drag}}\ . \tag{5.2}$$

For $t \ll t_{\rm drag}$, $dv_{\rm cl}(t)/dt \propto 1/t_{\rm drag} \propto 1/R_{\rm cl}$, then, the larger the cloud radius, the slower the cloud deceleration. In the supersonic case the formation of a bow shock in front of the cloud suppresses the formation of Kelvin-Helmholtz instabilities and hampers the cloud destruction (see also e.g., Scannapieco & Brüggen, 2015, and Sec. 2.4).

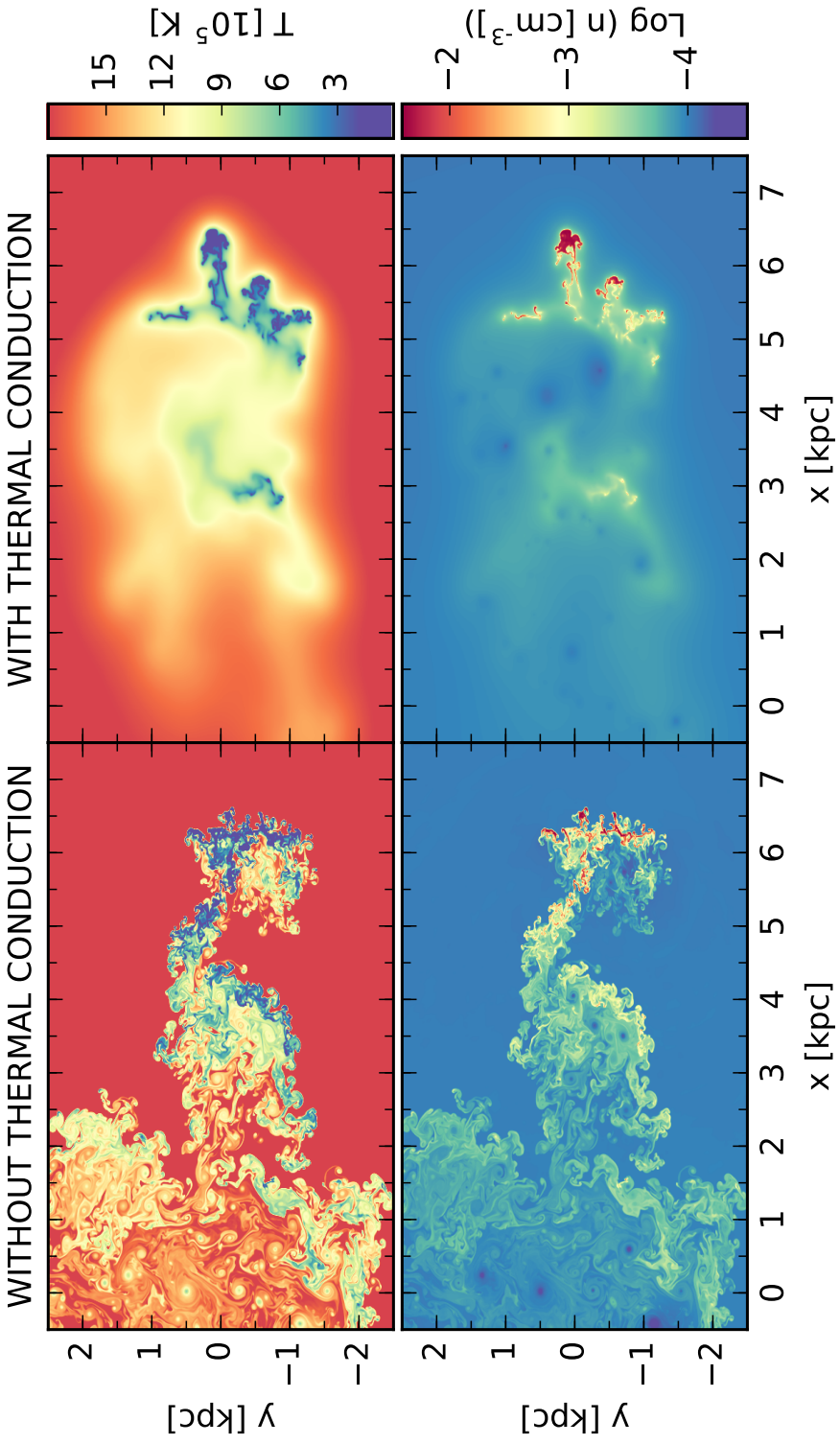

Figure 5.4: Temperature (*top panels*) and number density (*bottom panels*) snapshots of the simulations with initial cloud velocity $100\,\mathrm{km\,s^{-1}}$ and initial cloud radius 250 pc without (*left panels*) and with (*right panels*) thermal conduction. The time at which the snapshots have been taken is 200 Myr.

5.3.1 The role of thermal conduction

Thermal conduction is a key mechanism to consider in the interaction between different gas phases because it allows for transfer of heat from a hot to a cold medium, accelerating their mixing (Sec. 3.5 and 4.3).

In order to better understand how thermal conduction can influence the cloud survival, we chose a fiducial simulation, $R_{\rm cl} = 250$ pc and $v_{\rm cl} = 100\,{\rm km\,s^{-1}}$, and we analyzed it both in the absence and the presence of thermal conduction. Fig. 5.4 shows the temperature (top panels) and density (bottom panels) distributions on the grid after 200 Myr for the simulations without (left panels) and with (right panels) thermal conduction. The general evolution of the cloud is very different in the two cases. In the absence of thermal conduction the initial cloud is totally destroyed while the turbulent wake is characterized by the presence of a gradient in temperature and in density extended to several kpc downstream in the coronal medium. Colder and denser regions are situated in the head of the wake, where the gas lost from the cloud is not yet well mixed with the coronal gas. Most of this cold gas is approximately an order of magnitude less dense than the initial cloud ($n \sim 10^{-3}$ cm^{-3}), then, despite it encompasses a large volume, its contribution to the total mass will be low. Instead, in the presence of thermal conduction the bulk of the initial cloud is partially intact after 200 Myr and the cold gas mainly resides inside the dense cloud, while the wake is nearly lacking cold gas and it is composed by an extremely homogeneous mixture at $T \sim 10^6$ K and $n \sim 10^{-4}$ cm^{-3}. The effect of thermal conduction is indeed to create a more widespread and warmer wake in which temperature and density gradients have been smoothed.

Fig. 5.5 shows the quantitative results for these two simulations. We compared the evolution of the mass of cold gas ($T < 10^5$ K) with time and we found that it decreases in both cases. The cold gas lost from the cloud evaporates in the coronal medium because the warm wake, produced by the mixing of cold and hot gas, is unable to cool down. As we saw in Fig. 5.4, regardless of the presence of thermal conduction, regions in the wake at temperatures close to the peak of the cooling function ($T \sim 10^{5.5}$ K) exhibit very low densities ($n \sim 10^{-3}$ cm^{-3}) and metallicities ($Z < 0.3$ Z$_\odot$). Under these conditions, the condensation of gas is hard to occur. The efficiency of condensation strongly depends on gas density and metallicity (see Fig. 5.2): decreasing density and metallicity, the cooling rates decrease and the effect of heating photoionization becomes more and more important. Therefore, the net result is the loss of cold gas. However, Fig. 5.5 shows that the reduction of cold gas mass occurs faster without thermal conduction. After 250 Myr the mass of cold gas is $\sim 50\%$ of the initial cloud mass in the presence of thermal conduction compared to less than 40% in the absence of it.

Thermal conduction smooths the velocity gradient at the interface between the two fluids, making the cloud core more compact and preventing the formation of

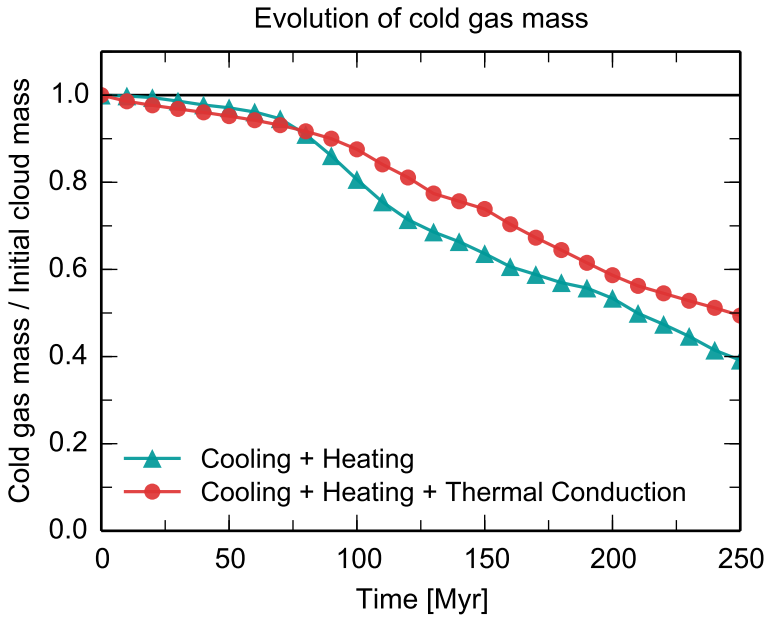

Figure 5.5: Evolution of the mass of cold gas ($T < 10^5$ K) with time for two simulations with initial cloud velocity 100 km s^{-1} and initial cloud radius 250 pc: one without (green line) and one with thermal conduction (red line).

Kelvin-Helmholtz instabilities and subsequent mixing (see also Vieser & Hensler, 2007b). This phenomenon explains the slow destruction of the cloud in the presence of thermal conduction. Once the gas is stripped from the cloud, thermal conduction changes its role, accelerating the heating of cold gas and its evaporation in the coronal medium.

5.3.2 Column densities: comparison with COS-Halos data

The key observational properties of the COS-Halos detections is given by their column densities. Here we compared the column densities of our fiducial simulation ($R_{\rm cl} = 250$ pc, $v_{\rm cl} = 100\,{\rm km\,s^{-1}}$) at 200 Myr with the COS-Halos observations. We estimated the column density of a given ion, $N_{\rm X}$, along random vertical lines across the simulation box by summing, for each pixel, i, along the line, the product between the hydrogen column density, $N_{{\rm H},i}$, the abundance of the ion with respect to its own species at the pixel temperature and hydrogen number density, $X/A\,(T_i, n_i)$, and the abundance of the species with respect to hydrogen at the pixel metallicity, $A/H\,(Z_i)$, as in following formula:

$$N_{\rm X} = \sum_i N_{{\rm H},i} \frac{X}{A}(T_i, n_i) \frac{A}{H}(Z_i) \tag{5.3}$$

For this calculation, we excluded the gas at $T > 10^6$ K, that is the temperature upper limit for the detected OVI (Werk et al., 2014). The abundance of the ion with respect to its own species, X/A, was obtained through the CLOUDY package, by using the same model including photoionization and collisional ionization that we described in Sec. 3.4.2 for the cooling/heating rates. The abundance of the species with respect to hydrogen, A/H, at a given metallicity was obtained by interpolating the solar and primordial abundances, taken from Sutherland & Dopita (1993).

The left panel of Fig. 5.6 shows the distribution of SiII, SiIII and OVI in bins of column density by directly comparing our simulation predictions to the observations. The blue bars represent the observed data, where we excluded all the upper and lower limits (from Tumlinson et al., 2011; Werk et al., 2013). The red bars represent the simulated column densities. The dotted line indicates the sensitivity limit of observations, while the simulations allow calculations of much lower values. We found that the ranges of observed and simulated column densities overlay for the low/intermediate ionization elements, while they do not overlap for the OVI. In the first case the mean values of two distributions differ by a factor of a few, while in the second case they differ almost by two orders of magnitude. Furthermore, the observed column densities extend to a higher range of values.

The different column densities may be explained by the fact that the observations can probe multiple cloudlets along the line of sight, while in our simulations we have effectively followed the evolution of a single cloud. The central panel of Fig. 5.6 shows the distribution of SiII, SiIII and OVI in bins of column density, accounting for presence of multiple cloudlets along the line of sight: the simulated column densities have been multiplied by a factor 3. We made this choice because it corresponds to the typical number of kinematic components present in individual absorption lines (Werk et al., 2013). We found that the column densities obtained from the simulation are in very good agreement with the observations for the SiII and the SiIII. However, the ranges of observed and simulated column densities do not overlap for the OVI, they differ by about one order of magnitude.

We also calculated the column densities for the simulation with $R_{\rm cl} = 500$ pc and $v_{\rm cl} = 200\,{\rm km\,s^{-1}}$, without taking into account the presence of multiple cloudlets along the line of sight. The agreement between simulations and observations is excellent for SiII and SiIII: the larger radius of the cloud implies a greater amount of cool gas and, then, higher column densities. Instead, also in this case, we found a comparatively worse agreement between the simulations and the observations for the OVI.

In order to examine the different behaviour of a weakly ionized element, as the SiII, and a highly ionized element, as the OVI, we analyzed their spatial distribution in our simulations. Fig. 5.7 shows the SiII (top panel) and OVI (bottom panel) number density distributions on the grid after 200 Myr in our fiducial simulation.

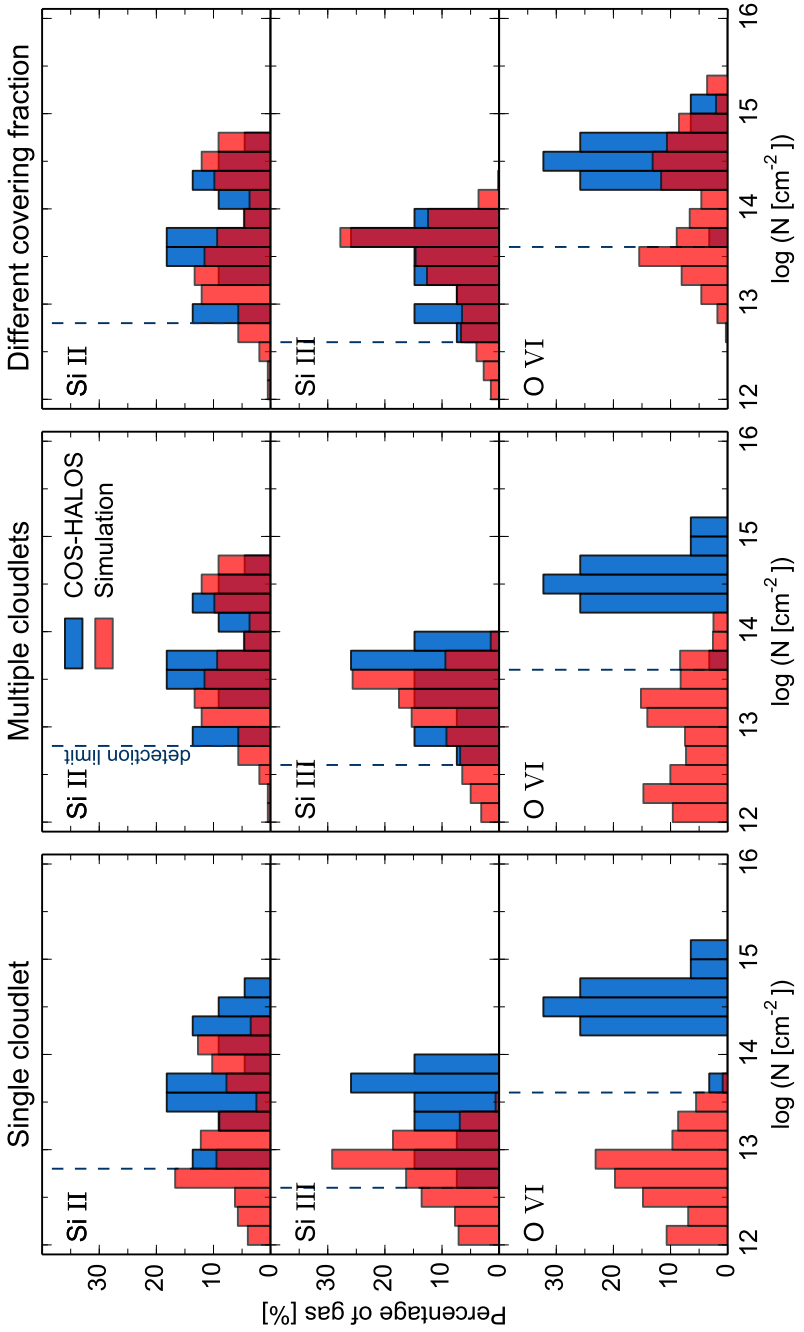

Figure 5.6: Histograms of distribution of the observed (blue bars) and simulated (red bars) data in bins of column density. The *top panels* show the distribution of SiII, the *middle panels* the distribution of SiIII and the *bottom panels* the distribution of OVI. The *left panel* was obtained by directly comparing the simulation results with the observations. The *central panel* was obtained by accounting for the contribution of 3 (average detections in COS-Halos) intervening clouds along the line of sight. The *right panel* was obtained both by accounting for the contribution of 3 simulated clouds along the line of sight and by considering a larger covering area for OVI ($\sim$ 20 times). The dotted line indicates the observational detection limit.

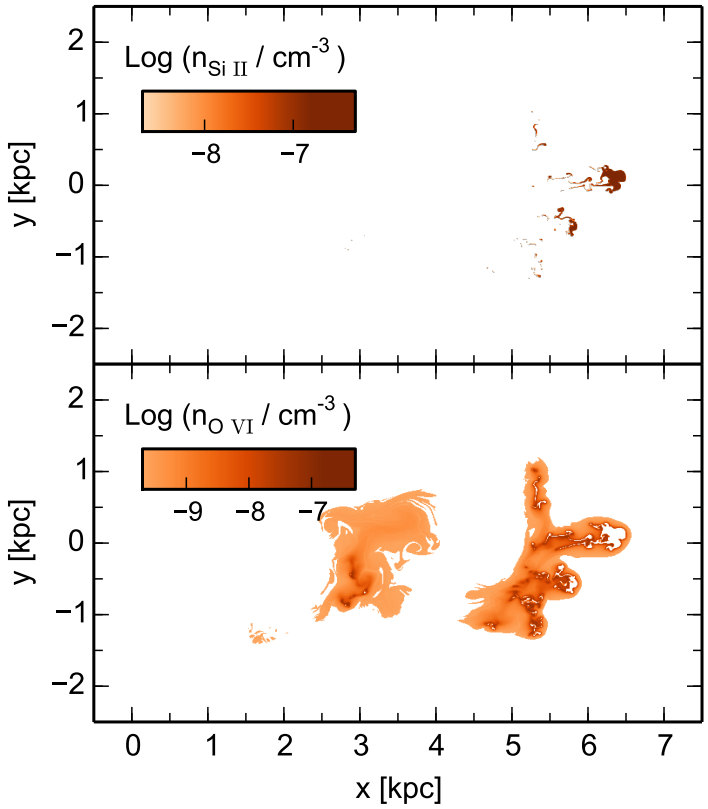

Figure 5.7: Snapshots of SiII (*top panel*) and OVI (*bottom panel*) number densities for the simulation with initial cloud velocity 100 km s^{-1} and initial cloud radius 250 pc with thermal conduction. The time at which the snapshots have been taken is 200 Myr. The white color indicates that the ion density is null or negligible (i.e. the cold gas in the cloud head or hot material with $T > 10^6$ K, the upper limit of temperature for the detected OVI).

The comparison between these snapshots and the right panels of Fig. 5.4 shows that the SiII traces the coldest and densest gas phase, it is present in the head of the cloud and in a few cold filaments in the wake, while it is totally absent everywhere else. Instead, the OVI is nearly absent in the coldest regions, while it is widely distributed in the wake, with peaks of density at the boundaries of the cold structures, where the mixing with hotter gas occurs and thermal conduction is stronger. Therefore, the OVI traces a warmer (T $\sim 10^{5-6}$ K) and more widespread gas phase, which occupies regions more spatially extended with respect to colder gas. It is therefore natural to expect that, generic lines of sight should cross an higher number of warm wakes containing OVI rather than cold cloud cores containing low ionization elements. In our simulation we estimate that the ratio between the area occupied by OVI and the area occupied by a generic low/intermediate ionization element, as the SiII, is ~ 20. Therefore, detection of ~ 3 clouds containing SiII could correspond to detection of ~ 60 regions containing OVI.

The right panel of Fig. 5.6 shows the numerical distribution of SiII, SiIII and OVI in bins of column density, taking into account observation of multiple clouds along the line of sight and a larger covering fraction for the OVI. In this case the simulated column densities have been multiplied for a factor 3 for SiII and SiIII and for a factor 60 for OVI. The ranges of column densities are in very good agreement with the observations both for the low/intermediate and for the high ionization elements. The observed and theoretical distributions of the low ions are also compatible with each other according to the Kolmogorov-Smirnov test, while the results for the OVI are dominated by the gap in detections present in the data between $10^{13.8}$ and $10^{14.2}$ cm^{-2} (see Fig. 5.6), which might be due to poor statistics.

We conclude by noting that due to the way thermal conduction operates, in particular suppressing cold cloudlets in the wake, warm (10^{5-6} K) gas can be found at large distances (several kpc) from the location of the cold material (see Fig. 5.4 and Fig. 5.7). This may be relevant in explaining the detections of OVI (see Werk et al., 2016, for other possible explanations) not directly associated with the classical Galactic HVCs, observed in HI, or with the Magellanic Stream (Sembach et al., 2003; Savage et al., 2003). Indeed, in our simulations, this intermediate temperature material appears to survive in the corona for times of the order of hundreds of Myr.

5.4 Discussion

Simulations of the survival of cold HVCs moving in a hot environment were already performed in the past, showing that the survival timescales are relatively short. Heitsch & Putman (2009) found that, for cloud velocities and halo densities typical of the Milky Way, HI clouds are destroyed on timescales of $\sim$ 100 Myr. However, they investigated the survival of HI gas ($T \lesssim 10^4$ K), while we took into account all gas at $T < 10^5$ K, i.e. both neutral and ionized cold gas. Furthermore, they analyzed clouds with mass $\lesssim 3 \times 10^4$ $\mathrm{M}_\odot$, while our mass range extends up to 1.6×10^5 $\mathrm{M}_\odot$. In order to better compare their result with ours, we analyzed the evolution of gas at $T \leq 10^4$ K in our simulations. We obtained that the mass surviving after 250 Myr is $\sim 35\%$ of the initial mass for the cloud with $M_{\mathrm{cl}} = 2 \times 10^4$ $\mathrm{M}_\odot$ and $v_{\mathrm{cl}} = 100\,\mathrm{km\,s^{-1}}$, while it is null for higher velocities. This result seems to agree with those of Heitsch & Putman (2009), accounting that they neglected thermal conduction, which prevents the cloud destruction. In our simulations with $M_{\mathrm{cl}} = 1.6 \times 10^5$ $\mathrm{M}_\odot$ the mass of gas at $T \leq 10^4$ K is less than 50% after 250 Myr.

Short survival timescales (100-200 Myr) were also found by Bland-Hawthorn et al. (2007). They focused on the origin of Hα emission along the MS and explained it as due to the interaction between the HI Stream and the hot corona: the cold ionized gas is shocked material as it is ablated from the Stream clouds by Kelvin-Helmholtz instabilities at the cloud-corona interface. This result agrees with ours:

the large amount of ionized gas at $T \sim 10^{4-5}$ K found by Bland-Hawthorn et al. (2007) is comparable to the cold gas mass at $T < 10^5$ K that survives in our simulations.

Both the simulations above mentioned were performed in a three-dimensional cartesian geometry, while all our simulations are two-dimensional. Indeed, 3D simulations would have imply prohibitive computational times for a code with static grid, as ATHENA. In Sec. 4.4.1, we compared low-resolution simulations of cloud-corona interaction obtained by using the two different geometries. We found that, since in 3D the contact surface between the two fluids is larger, Kelvin-Helmholtz instabilities and subsequent loss of gas from the cold cloud evolve more quickly. In this work, the effect of 2D geometry could therefore be to slow down the cloud destruction. However, in Sec. 4.4.1, the difference in terms of mass of cold gas between the two geometries is lower than 10% during the whole computational time, so it does not affect significantly the final result. Moreover, we point out that in the present work thermal conduction is much more important to prevent the cloud destruction than for the simulations shown in Chapter 4. Thus, it is likely that the larger contact surface in 3D simulations would increase the development of velocity gradients at cloud-corona interface and the efficiency of thermal conduction. Therefore, it is unclear whether the combination of thermal conduction and 3D geometry would result in faster or slower cloud destruction, but we do not expect a significant difference with respect to our 2D simulations.

The simulations in the literature most similar to ours are those of Kwak, Henley & Shelton (2011), who simulated in a 2D cartesian geometry the motion of HVCs through the Galactic corona. They found that clouds with masses larger than 4×10^5 $M_\odot$ remain largely intact after 240 Myr, while we found that also clouds with smaller mass ($M_{\rm cl} = 1.6 \times 10^5$ $M_\odot$) are able to keep a large fraction of their own initial mass ($\gtrsim 70\%$ after 250 Myr). However, as Heitsch & Putman (2009), Kwak, Henley & Shelton (2011) analyzed the survival of HI gas, at $T \leq 10^4$ K and neglected thermal conduction. It is interesting to point out that, similarly to our analysis, they found that high ionization elements, as OVI, are produced by cloud-corona mixing and lines of sight that cross the turbulent wake detect a large number of high ionization elements but a small numbers of low ionization elements, which are nearly absent in the wake.

In Chapter 2 and 4, we analyzed the cloud motion at the disc-corona interface (a few kpc above the disc), showing that the cloud is able to trigger the condensation of a large portion of coronal material. This result does not contradict those presented here. Indeed, the coronal density in the region close to the galactic disc is around an order of magnitude larger than the coronal density in the outer halo that we considered in this Chapter. The balance between evaporation and condensation strongly depends on this density, since the cooling rate is proportional to its

square. Decreasing the coronal density, the gas condensation becomes ineffective and the cloud destruction occurs. This result is very important and can allow us to speculate about the possible fate of cold clouds in the Galactic corona. In fact, by extrapolating the trend of Fig. 5.5 up to 500 Myr, we should conclude that clouds with $R_{\rm cl} = 250$ pc do not survive their trip through the coronal medium beyond 500 Myr. However, if the cloud travels towards the galaxy centre, it passes through denser and denser regions of the corona and the loss of gas might trigger the production of fresh cold gas rather than its disappearance. Thus, we may speculate that these clouds could become potential contributors to cold gas accretion onto the Galactic disc (Sancisi et al., 2008).

5.5 Conclusions

In the last years, sensitive observations have revealed that low-redshift galaxies are embedded in extended haloes of multiphase gas, the circumgalactic medium. An important improvement to our knowledge of the CGM was obtained by the COS-Halos survey, which has detected gas through absorption lines against background QSO for a sample of galaxies at low-redshift, finding that a large fraction of galaxies, regardless of their type, are surrounded by large amount of cold and ionized gas ($T < 10^5$ K), extending out to impact parameters of 150 kpc from the galaxy centre.

In this Chapter we have explored the physical conditions that allow the survival of cold gas in hot galactic coronae. We performed high-resolution hydrodynamical simulations of cold neutral clouds ($T = 10^4$ K) travelling through a hot ($T = 2 \times 10^6$ K) and low-density ($n = 10^{-4}$ cm^{-3}) ambient medium. From our simulations, we conclude that the interaction and mixing between cold clouds and a hot corona lead to a gradual loss of gas from the clouds. The survival time of cold ($T < 10^5$ K) gas strongly depends on initial size (mass) of the cloud: clouds with radius $\gtrsim 250$ pc (mass $\gtrsim 2 \times 10^4\,{\rm M}_\odot$) are able to keep a large fraction of their own initial mass for hundreds of Megayears. Thermal conduction appears quite important for the cloud survival: its effect is to smooth the velocity gradients at the interface between cloud and corona, preventing the formation of Kelvin-Helmholtz instabilities and slowing down the cloud destruction.

We compared the column densities of our simulations with the column densities of the COS-Halos observations. The agreement is very good for low/intermediate ionization elements, as SiII and SiIII, but not for high ionization elements, as OVI. However, we observed that, while SiII traces a cold gas phase, mainly located inside the cloud, OVI traces a warmer gas phase, situated in the turbulent wake behind the cloud, produced by the mixing between the cold gas ablated from the cloud and the hot coronal medium. In the simulations, this warm phase covers an area $\simeq 20$

times larger than the cold gas phase. Therefore, accounting that observations can detect multiple clouds along the line of sight, the probability of detecting diffuse and extended wakes is much higher than the probability to intercept compact cloud heads. Taking into account this correction, the range of our predicted OVI column densities overlaps with the observations.

Our only result incompatible with the COS-Halos findings concerns the number gas density. Werk et al. (2014) found that it is very low ($n \sim 10^{-4}$ cm^{-3}) and inconsistent with its being in pressure equilibrium with the hot gas phase. This result is very puzzling because it is not clear how the cold material could survive in these conditions. Indeed, we found that clouds initially out of equilibrium reach pressure equilibrium in a few Myr. Moreover, despite the cold gas density can decrease once gas is stripped from the cloud, it remains at least an order of magnitude larger than cold gas density found by Werk et al. (2014). However, this latter remains quite uncertain due to uncertainty in EUVB radiation field used for the modelling of the HI column densities.

We can conclude that our results suggest that the existence and the ubiquity of large amount of cold/warm gas in the CGM is possible because large enough clouds, made compact by the effect of thermal conduction, are able to survive their interaction with the hot corona for several hundreds of Myr. This may have important implications for the gas accretion necessary to fuel star-formation in Milky Way galaxies (see Sec. 1.3). A recurrent question is, for instance, whether a massive structure like the MS can reach the disc of the Milky Way, feeding the star formation (e.g., Fox et al., 2014). We can speculate that the cloudlets composing the MS with mass $\sim 10^5$ M$_\odot$ can survive the journey through the Galactic corona and provide a significant amount of gas accretion.

Chapter 6

Concluding remarks

In this Thesis, we studied the multiphase gaseous haloes surrounding low-redshift disc galaxies. Through high-resolution hydrodynamical simulations, we investigated how various physical processes, such as gas radiative cooling, thermal conduction, gas photoionization by extragalactic sources, affect the interaction between the different gas phases in the galactic haloes. The final goal of this work is to shed light on the interplay between disc galaxies and their surrounding environments, a crucial issue in the context of galaxy evolution.

In this last Chapter, we summarize the results obtained in this Thesis (Sec. 6.1) and discuss their implications for the evolution of disc galaxies (Sec. 6.2).

6.1 Summary

We used two-dimensional hydrodynamical simulations as a research method throughout the Thesis. In particular, we performed different sets of simulations to study the evolution of a cloud of cold ($T = 10^4$ K) gas travelling through a less dense and hotter medium ($T \geq 10^6$ K), representing the galactic corona surrounding galactic discs. The initial parameters of each simulation varied according to the astrophysical problem to study and, for each problem, according to the physical conditions to explore.

Our simulations have shown that Kelvin-Helmholtz instabilities, due to the relative motion between cloud and corona, destroy the cloud's edges causing mixing between the stripped gas and the surrounding coronal material. When thermal conduction is included, the development of these instabilities and the subsequent cloud destruction may slow down considerably. If mixing efficiently starts, a turbulent wake at intermediate temperature ($10^4\,\mathrm{K} < T < 10^6\,\mathrm{K}$) forms behind the cloud. The gas in this mixture may evaporate in the surrounding hot medium or condense in cooler and smaller structures, depending on the physical properties of the cloud and the corona (e.g. density, metallicity, temperature, relative velocity and cloud radius) and the physical processes included in the simulations. Studying the fate of this gas was the main aim of our investigations. We modelled its evolution with local-scale simulations, due to the requirement of very high spatial resolution (~ 1 pc) needed to capture all the details of the mixing between the cold cloud and the hot coronal gas.

The main results of this Thesis can be summarized as follows:

1) **Origin of Complex C** (Chapter 2)
Complex C is the most prominent and metal-poor high-velocity cloud of the Milky Way. Its origin, as well as the origin of the other high-velocity complexes, has remained a mystery for fifty years. So far, two competing scenario have been proposed, suggesting either external or internal origin to the Milky Way's disc (e.g., Oort, 1970; Bregman, 1980). We combined a dynamical model of galactic fountain (Marasco, Fraternali & Binney, 2012) with hydrodynamical simulations (with the ECHO++ code, Del Zanna et al., 2007) of cold and metal-rich ($T = 10^4$ K, $Z = \mathrm{Z}_\odot$) clouds travelling through the hot and metal-poor ($T = 2 \times 10^6$ K, $Z = 0.1\ \mathrm{Z}_\odot$) coronal medium of the Milky Way. We demonstrated that Complex C can be the consequence of a giant supernova explosion ($\sim 10^4$ supernovae) that occurred in the Cygnus-Outer spiral arm 150 million years ago. The ejected material has travelled through the halo region, mixing with the hot gas from the Galactic corona and triggering its condensation. The main outcome of our work has been to reproduce the very low metallicity of Complex C, considered the main evidence for its extra-galactic origin. From our simulations, we indeed obtained metallicities in very good agreement with the observed metallicities for Complex C and the same weak anti-correlation between metallicities and HI column densities as seen in the data (Collins, Shull & Giroux, 2007).

2) **Gas cooling at the disc-corona interface** (Chapter 4)
As in the case of Complex C, in the region at the interface disc-corona, interaction between cold ($T \lesssim 10^4$ K) and metal-rich disc material ejected into the halo in the form of fountain clouds and the surrounding hot coronal material ($T \gtrsim 10^6$ K) can dramatically reduce the cooling time of a portion of the corona and produce its

condensation. This phenomenon can lead to accretion of cold gas from the lower and denser ($n = 10^{-3}$ cm^{-3}) corona onto the star-forming disc in Milky Way-like galaxies (Marinacci et al., 2010, 2011). In this Thesis, we studied the interaction between fountain clouds and the corona as a function of the coronal temperature, through parsec-scale hydrodynamical simulations, that include radiative cooling and thermal conduction, a key mechanism influencing gas condensation. The code used for these simulations is ATHENA (Stone et al., 2008). The main features of ATHENA and the details of our implementation of radiative processes and thermal conduction are presented in Chapter 3. Our simulations showed that the coronal gas condensation strongly depends on the coronal temperature, in particular it is less efficient for increasing temperature. The coronal temperature is expected to be close to the virial temperature of galaxy, which in turn correlates with the virial mass of the dark matter halo where the galaxy resides. Therefore, our results indicate that the coronal gas condensation decreases for increasing halo mass. In particular, its efficiency drops significantly for objects with virial masses larger than 8×10^{12} M$_\odot$. This result implies that the coronal gas cools down quickly in haloes with low-intermediate virial mass ($M_{\rm vir} \lesssim 3 \times 10^{12}$ M$_\odot$) but the ability to cool the lower corona decreases going from late-type to early-type disc galaxies, potentially leading to the switching off of accretion and the quenching of star formation in massive systems.

3) **Survival of gas clouds in the CGM** (Chapter 5)
Recent observations of the CGM around low-redshift galaxies have shown the presence of large amounts of cold and warm ionized gas out to more than 100 kpc from the central galaxies (COS-Halos survey, Tumlinson et al., 2013; Werk et al., 2013). We studied under what physical conditions cold gas ($T < 10^5$ K) can survive in the CGM of Milky Way-like galaxies. We assumed that the observed cold/warm ionized gas is associated to the interaction and mixing between a colder neutral phase and the hot coronal medium. To study this phenomenon, we performed a set of hydrodynamical simulations of cold ($T = 10^4$ K) neutral gas clouds travelling through a hot ($T = 2 \times 10^6$ K) and low-density ($n = 10^{-4}$ cm^{-3}) coronal medium, typical of Milky Way-like galaxies at large galactocentric distances ($\sim 50 - 150$ kpc). We explored the effects of different initial values of relative velocity and radius of the clouds. With respect to those simulations presented in Chapter 4, these simulations include photoionization from an uniform UV background (Haardt & Madau, 2012). Our main result is that large clouds (radii larger than 250 pc) may survive for very long time (at least 250 Myr): their mass decreases during their trajectory but at very low rates. We found that thermal conduction plays a significant role: its effect is to hinder the development of Kelvin-Helmholtz instabilities at the cloud-corona interface, keeping the cloud compact and therefore more difficult to destroy. The distribution of column densities in our simulations are compatible with those observed by the COS-Halos survey for low-temperature ions (e.g. SiII and SiIII) and

for high-ions (OVI).

6.2 Gas feeding in disc galaxies

Low-redshift disc galaxies are surrounded by extended haloes of multiphase gas. These haloes are the result of flows of material towards and away from galaxies, representing, then, both a tracer of the past stellar activity and the fuel for the future star formation. The study of the nature and the origin of these haloes constitutes a key step to our understanding of galaxy formation and evolution.

Here, we focus on a fundamental issue concerning the evolution of disc galaxies, that is how they accrete gas from the surrounding environment to grow and feed their star formation. As discussed in Sec. 1.3 and in Chapter 4, observational evidence indicates that, in these galaxies, the gas consumed by the process of star formation needs to be continuously replenished by gas accretion from the ambient medium. In the next sections, we discuss how the results of this Thesis can give clues to address this long standing puzzle. In Sec. 6.2.1, we focus on gas accretion at the disc-corona interface, while, in Sec. 6.2.2, we speculate on the fate of the cold gas in the CGM and its possible impact on gas feeding in disc galaxies.

6.2.1 Disc-corona interface

In Chapter 2 and 4, we showed that star-forming galaxies like the Milky Way can accrete material from the surrounding hot corona through the galactic fountain. Gas accretion is triggered by cold disc material ejected into the halo in the form of fountain clouds and by its mixing with the lower layers of the hot corona, close to the galactic disc (within a few kpc). This mixing significantly reduces the cooling rate of the coronal gas, triggering the condensation and accretion of a portion of corona onto the disc. It is evident that the accretion driven by galactic fountains is a self-regulating mechanism: it is triggered and regulated by stellar feedback and, in turn, regulates a new stellar cycle by supplying cold gas. Therefore, this phenomenon can not occur in galaxies lacking a cold star-forming disc.

Our fountain-driven accretion model presents clear observational validations. Accretion driven by galactic fountain succeeds to explain the kinematics, and in particular the slow rotation, of the extra-planar HI in nearby disc galaxies (Fraternali & Binney, 2008; Marinacci et al., 2011). Moreover, it is able to reproduce the HI kinematics of the extra-planar gas in our Galaxy (Marasco, Fraternali & Binney, 2012), returning a global accretion rate of $\sim 2\,M_\odot\,yr^{-1}$, in very good agreement with the accretion required to sustain the star formation in the Milky Way ($1 - 3\,M_\odot\,yr^{-1}$, Chomiuk & Povich, 2011). Finally, the fountain-driven accretion model reproduces the kinematics, distance and metallicity of Complex C, the most

prominent Milky-Way's HVCs, as demonstrated in Chapter 2. The last two results, concerning our Galaxy, show that both the seed of the IVCs and that of the HVCs can originate from the Galactic disc. In this picture, the HVCs are an extreme and rare phenomenon, caused by a powerful superbubble explosion.

In Chapter 4, we also found that the condensation of coronal gas via galactic fountain becomes less and less efficient with increasing virial temperature of the galaxy and completely ineffective for $T_{\rm vir} > 4 \times 10^6$ K. This finding can have important implications on both environment and mass quenching of the star formation. Indeed, in our model, the star-formation quenching only depends on the virial temperature, which is both an important feature of the environment surrounding the galaxy (e.g. field galaxy or galaxy cluster) and a measure of the virial mass of the galaxy. Therefore, our result suggests that both galaxies located in dense environments with high coronal temperature (e.g. galaxy clusters), and massive disc galaxies, characterized by high virial temperature, are not able to induce the condensation of the surrounding hot corona and they will experience the quenching of the star formation after consuming all of their disc gas reservoir.

We conclude that our model of gas accretion driven by galactic fountains provides a good solution to the problem of gas replenishment in Milky Way-like galaxies. In this way, we may explain how these galaxies sustain their own star formation after the turn-off of the *cold mode* accretion, when gas supply no longer comes from cosmological cold filaments but from shock-heated coronal gas. Moreover, our solution is well integrated in the overall picture of galaxy evolution, according to which massive disc galaxies ($M_{\rm vir} \gg 10^{12}\,{\rm M}_\odot$) have exhausted their own fuel for star formation and are moving towards or lie on the red sequence of the quiescent galaxies (e.g., Schawinski et al., 2014).

Future investigations of the kind performed in this Thesis may consider the inclusion of gas heating due to stellar radiation in hydrodynamical simulations. In this way, we can model condensation and accretion of coronal gas in galaxies at different levels of star formation, from nearly inactive to active star-forming galaxies. Our guess is that accretion driven by galactic fountain is inefficient in disc galaxies with high star formation, where the strong stellar radiation can not only prevent the condensation of coronal gas but also lead to the evaporation of fountain gas. In this case, supernova feedback would not longer represent *positive* feedback, that supplies cold coronal gas available for star formation to the disc, but it would become *negative* feedback, that dissipates cold disc material into the surrounding ambient.

Finally, for a more complete characterization of the phenomenon, one might consider to perform 3D hydrodynamical simulations of the overall galactic fountain cycle, starting from superbubble explosion, throughout portions of galactic disc. Static grid codes, like ATHENA, are unsuitable to model this configuration because of very long computational times involved. The solution consists in the use of Adap-

tive Mesh Refinement (AMR) codes. However, reproducing the results obtained so far by ATHENA with an AMR code, such as ENZO (Bryan & Norman, 1997), is not trivial. Our preliminary results (Marco Canducci, Master Thesis, University of Bologna) have shown that, when the resolution of the best-refined grids is equal to the typical resolution used with ATHENA (2pcx2pc), ENZO overestimates the amount of condensation with respect to ATHENA, independently of the refinement criterion. Further tests to match the results are required before carrying out our investigation with an AMR code.

6.2.2 Gas from the Circumgalactic Medium

A second line of study investigated in this Thesis concerns the survival of cold gas clouds at large distances from galaxies and, in particular, the possibility that they survive their journey through the galactic corona down to the star-forming disc.

HI observations in the local Universe indicate that cold gas accretion from minor mergers can account only for $\sim 10\%$ of the gas needed to sustain star formation of Milky Way-like galaxies at the current rate (Sancisi et al., 2008). However, detections of ionized gas through absorption line observations reveal that the mass of cold ionized gas can be more than one order of magnitude larger than the HI mass of the CGM around the Milky Way (e.g., Shull et al., 2009). Thus, cold ionized gas may represent a reservoir of gas available for star formation, provided that it survive its own journey out to the star-forming disc without being destroyed by the interaction with the hot corona. In Chapter 5, we demonstrated that only massive clouds ($M >$ few $10^4\,\mathrm{M}_\odot$) may survive for long times, at least 250 Myr. An important support for the survival of these clouds is supplied by thermal conduction.

Concerning our own Galaxy, the accretion rate due to the classical HVCs is merely $0.08\,\mathrm{M}_\odot\,\mathrm{yr}^{-1}$ (Putman, Peek & Joung, 2012). Larger amount of accreting gas may be contributed by the Magellanic Stream. Fox et al. (2014) have indeed found that the mass of cold (neutral + ionized) gas of the Magellaninc Stream is roughly $10^9(d\,/\,55\,\mathrm{kpc})^2\,\mathrm{M}_\odot$. If the Stream survives its journey through the Galactic corona, it will merge with the Galactic disc on a time-scale of $\sim 0.5 - 1$ Gyr for $d = 55 - 100$ kpc. We can speculate that the cold clouds within the Stream will lose part of their own gas and only the largest clouds ($M \gg 10^4\,\mathrm{M}_\odot$) will survive their journey through the Galactic corona, providing cold gas available for the star formation.

Knowing the fate of cold clouds in the CGM requires knowing their origin, in order to determine if this gas is effectively infalling onto the disc and contributing to the star formation. The presence of metals in the CMG suggests that most of this gas is composed by material synthesized by stellar evolution, ejected from galaxies through large-scale galactic outflows with highly supersonic speeds (e.g.,

Ford et al., 2013). In this context, the next step will be to perform hydrodynamical simulations of cold clouds travelling through the coronal medium with supersonic velocities ($500 - 1000\,\mathrm{km\,s^{-1}}$) in the presence of the vertical gravitational field of the galaxy. The main goal of these simulations will be to understand if the outflowing disc material is dispersed in the hot corona or comes back onto the disc, in order to constrain the physical processes than drive the gas cycle in galactic haloes and to improve our understanding of how galaxies evolve in their environment.

Bibliography

Anderson M. E., Bregman J. N., 2010, ApJ, 714, 320

Anderson M. E., Bregman J. N., 2011, ApJ, 737, 22

Anderson M. E., Churazov E., Bregman J. N., 2016, MNRAS, 455, 227

Armillotta L., Fraternali F., Marinacci F., 2016, MNRAS, 462, 4157

Armillotta L., Werk J. K., Prochaska J. X., Fraternali F., Marinacci F., 2016, ArXiv e-prints

Aumer M., Binney J. J., 2009, MNRAS, 397, 1286

Balbus S. A., 1986, ApJ, 304, 787

Barger K. A., Lehner N., Howk J. C., 2016, ApJ, 817, 91

Bauermeister A., Blitz L., Ma C.-P., 2010, ApJ, 717, 323

Begelman M. C., McKee C. F., 1990, ApJ, 358, 375

Behroozi P. S., Wechsler R. H., Conroy C., 2013, ApJ, 770, 57

Benson A. J., Bower R. G., Frenk C. S., Lacey C. G., Baugh C. M., Cole S., 2003, ApJ, 599, 38

Besla G., Kallivayalil N., Hernquist L., van der Marel R. P., Cox T. J., Kereš D., 2012, MNRAS, 421, 2109

Binney J., 1977, ApJ, 215, 483

Binney J., Nipoti C., Fraternali F., 2009, MNRAS, 397, 1804

Binney J., Tremaine S., 2008, Galactic Dynamics: Second Edition. Princeton University Press

Birnboim Y., Dekel A., 2003, MNRAS, 345, 349

Biskamp D., 2000, Magnetic Reconnection in Plasmas

Bland-Hawthorn J., Sutherland R., Agertz O., Moore B., 2007, ApJL, 670, L109

Bogdán Á. et al., 2013, ApJ, 772, 97

Bolatto A. D. et al., 2013, Nature, 499, 450

Boomsma R., Oosterloo T. A., Fraternali F., van der Hulst J. M., Sancisi R., 2008, A&A, 490, 555

Boselli A., Gavazzi G., Donas J., Scodeggio M., 2001, AJ, 121, 753

Bregman J. N., 1980, ApJ, 236, 577

Bregman J. N., 2007, ARA&A, 45, 221

Brinchmann J., Charlot S., White S. D. M., Tremonti C., Kauffmann G., Heckman T., Brinkmann J., 2004, MNRAS, 351, 1151

Brüns C. et al., 2005, A&A, 432, 45

Bryan G. L., Norman M. L., 1997, in Astronomical Society of the Pacific Conference Series, Vol. 123, Computational Astrophysics; 12th Kingston Meeting on Theoretical Astrophysics, Clarke D. A., West M. J., eds., p. 363

Bryan G. L., Norman M. L., 1998, ApJ, 495, 80

Catinella B. et al., 2010, MNRAS, 403, 683

Cavichia O., Mollá M., Costa R. D. D., Maciel W. J., 2014, MNRAS, 437, 3688

Chandran B. D. G., Cowley S. C., 1998, Physical Review Letters, 80, 3077

Chiappini C., Matteucci F., Romano D., 2001, ApJ, 554, 1044

Chomiuk L., Povich M. S., 2011, AJ, 142, 197

Colella P., Woodward P. R., 1984, Journal of Computational Physics, 54, 174

Collins J. A., Rand R. J., 2001, ApJ, 551, 57

Collins J. A., Shull J. M., Giroux M. L., 2003, ApJ, 585, 336

Collins J. A., Shull J. M., Giroux M. L., 2007, ApJ, 657, 271

Cowie L. L., McKee C. F., 1977, ApJ, 211, 135

Dai X., Anderson M. E., Bregman J. N., Miller J. M., 2012, ApJ, 755, 107

Dalton W. W., Balbus S. A., 1993, ApJ, 404, 625

Dekel A., Birnboim Y., 2006, MNRAS, 368, 2

Del Zanna L., Zanotti O., Bucciantini N., Londrillo P., 2007, A&A, 473, 11

Di Teodoro E. M., Fraternali F., 2014, A&A, 567, A68

Dubois Y., Devriendt J., Slyz A., Teyssier R., 2012, MNRAS, 420, 2662

Einfeldt B., Munz C. D., Roe P. L., Sjögreen B. J., 1991, Comp. Phys., 92, 273

Esteban C., Carigi L., Copetti M. V. F., García-Rojas J., Mesa-Delgado A., Castañeda H. O., Péquignot D., 2013, MNRAS, 433, 382

Faerman Y., Sternberg A., McKee C. F., 2016, ArXiv e-prints

Ferland G. J., Korista K. T., Verner D. A., Ferguson J. W., Kingdon J. B., Verner E. M., 1998, PASP, 110, 761

Ferland G. J. et al., 2013, RMxAA, 49, 137

Fernández X., Joung M. R., Putman M. E., 2012, ApJ, 749, 181

Field G. B., 1965, ApJ, 142, 531

Ford A. B., Oppenheimer B. D., Davé R., Katz N., Kollmeier J. A., Weinberg D. H., 2013, MNRAS, 432, 89

Ford H. A., Lockman F. J., McClure-Griffiths N. M., 2010, ApJ, 722, 367

Fox A. J. et al., 2016, ApJL, 816, L11

Fox A. J., Savage B. D., Wakker B. P., Richter P., Sembach K. R., Tripp T. M., 2004, ApJ, 602, 738

Fox A. J. et al., 2014, ApJ, 787, 147

Fox A. J., Wakker B. P., Smoker J. V., Richter P., Savage B. D., Sembach K. R., 2010, ApJ, 718, 1046

Fraternali F., Binney J. J., 2006, MNRAS, 366, 449

Fraternali F., Binney J. J., 2008, MNRAS, 386, 935

Fraternali F., Marasco A., Armillotta L., Marinacci F., 2015, MNRAS, 447, L70

Fraternali F., Marasco A., Marinacci F., Binney J., 2013, ApJL, 764, L21

Fraternali F., Oosterloo T., Sancisi R., 2004, A&A, 424, 485

Fraternali F., Oosterloo T., Sancisi R., van Moorsel G., 2001, ApJL, 562, L47

Fraternali F., Tomassetti M., 2012, MNRAS, 426, 2166

Fraternali F., van Moorsel G., Sancisi R., Oosterloo T., 2002, AJ, 123, 3124

Fromang S., Hennebelle P., Teyssier R., 2006, A&A, 457, 371

Fukugita M., Peebles P. J. E., 2006, ApJ, 639, 590

Gatto A., Fraternali F., Read J. I., Marinacci F., Lux H., Walch S., 2013, MNRAS, 433, 2749

Gerhard O., 2011, Memorie della Societa Astronomica Italiana Supplementi, 18, 185

Gibson B. K., Giroux M. L., Penton S. V., Stocke J. T., Shull J. M., Tumlinson J., 2001, AJ, 122, 3280

Gnat O., Sternberg A., 2007, ApJS, 168, 213

Godunov S. K., 1959, Math. Sbornik, 47, 271–306, translated US Joint Publ. Res. Service, JPRS 7226, 1969

Grcevich J., Putman M. E., 2009, ApJ, 696, 385

Grevesse N., Sauval A. J., 1998, Space Science Reviews, 85, 161

Haardt F., Madau P., 2012, ApJ, 746, 125

Harten A., 1983, Journal of Computational Physics, 49, 357

Heald G. H., Rand R. J., Benjamin R. A., Bershady M. A., 2006, ApJ, 647, 1018

Heald G. H., Rand R. J., Benjamin R. A., Bershady M. A., 2007, ApJ, 663, 933

Heitsch F., Putman M. E., 2009, ApJ, 698, 1485

Hobbs A., Read J., Power C., Cole D., 2013, MNRAS, 434, 1849

Hodges-Kluck E. J., Bregman J. N., 2013, ApJ, 762, 12

Hodges-Kluck E. J., Miller M. J., Bregman J. N., 2016, ApJ, 822, 21

Hoopes C. G., Walterbos R. A. M., Rand R. J., 1999, ApJ, 522, 669

Houck J. C., Bregman J. N., 1990, ApJ, 352, 506

Hsu W.-H., Putman M. E., Heitsch F., Stanimirović S., Peek J. E. G., Clark S. E., 2011, AJ, 141, 57

Hunter I. et al., 2009, A&A, 496, 841

Joung M. R., Putman M. E., Bryan G. L., Fernández X., Peek J. E. G., 2012, ApJ, 759, 137

Kalberla P. M. W., Burton W. B., Hartmann D., Arnal E. M., Bajaja E., Morras R., Pöppel W. G. L., 2005, A&A, 440, 775

Kalberla P. M. W., Haud U., 2006, A&A, 455, 481

Kannan R., Springel V., Pakmor R., Marinacci F., Vogelsberger M., 2016, MNRAS, 458, 410

Kaufmann T., Mayer L., Wadsley J., Stadel J., Moore B., 2006, MNRAS, 370, 1612

Kennicutt, Jr. R. C., 1983, ApJ, 272, 54

Kereš D., Katz N., Fardal M., Davé R., Weinberg D. H., 2009, MNRAS, 395, 160

Komatsu E. et al., 2009, ApJS, 180, 330

Kwak K., Henley D. B., Shelton R. L., 2011, ApJ, 739, 30

Lacey C., Cole S., 1993, MNRAS, 262, 627

Lehner N., Howk J. C., 2011, Science, 334, 955

Lehner N., Howk J. C., Thom C., Fox A. J., Tumlinson J., Tripp T. M., Meiring J. D., 2012, MNRAS, 424, 2896

Lewis G. F. et al., 2013, ApJ, 763, 4

Li Y.-S., White S. D. M., 2008, MNRAS, 384, 1459

Lockman F. J., 2002, ApJL, 580, L47

Lux H., Read J. I., Lake G., Johnston K. V., 2013, MNRAS, 436, 2386

Mac Low M.-M., McCray R., Norman M. L., 1989, ApJ, 337, 141

Maller A. H., Bullock J. S., 2004, MNRAS, 355, 694

Marasco A., Fraternali F., 2011, A&A, 525, A134

Marasco A., Fraternali F., 2016, ArXiv e-prints

Marasco A., Fraternali F., Binney J. J., 2012, MNRAS, 419, 1107

Marasco A., Marinacci F., Fraternali F., 2013, MNRAS, 433, 1634

Marinacci F., Binney J., Fraternali F., Nipoti C., Ciotti L., Londrillo P., 2010, MNRAS, 404, 1464

Marinacci F., Fraternali F., Nipoti C., Binney J., Ciotti L., Londrillo P., 2011, MNRAS, 415, 1534

Martin C. L., Shapley A. E., Coil A. L., Kornei K. A., Bundy K., Weiner B. J., Noeske K. G., Schiminovich D., 2012, ApJ, 760, 127

Mastropietro C., Moore B., Mayer L., Wadsley J., Stadel J., 2005, MNRAS, 363, 509

Matteucci F., 2012, Chemical Evolution of Galaxies

Matthews L. D., Wood K., 2003, ApJ, 593, 721

Mayer L., Mastropietro C., Wadsley J., Stadel J., Moore B., 2006, MNRAS, 369, 1021

Melioli C., Brighenti F., D'Ercole A., de Gouveia Dal Pino E. M., 2008, MNRAS, 388, 573

Melioli C., de Gouveia Dal Pino E. M., Geraissate F. G., 2013, MNRAS, 430, 3235

Mignone A., Bodo G., Massaglia S., Matsakos T., Tesileanu O., Zanni C., Ferrari A., 2007, ApJS, 170, 228

Miller M. J., Bregman J. N., 2015, ApJ, 800, 14

Moster B. P., Naab T., White S. D. M., 2013, MNRAS, 428, 3121

Muller C. A., Oort J. H., Raimond E., 1963, Academie des Sciences Paris Comptes Rendus, 257, 1661

Narayan R., Medvedev M. V., 2001, ApJL, 562, L129

Nelson D., Vogelsberger M., Genel S., Sijacki D., Kereš D., Springel V., Hernquist L., 2013, MNRAS, 429, 3353

Nipoti C., Posti L., 2013, MNRAS, 428, 815

Olano C. A., 2008, A&A, 485, 457

Oort J. H., 1970, A&A, 7, 381

Oosterloo T., Fraternali F., Sancisi R., 2007, AJ, 134, 1019

Pagel B. E. J., 2009, Nucleosynthesis and Chemical Evolution of Galaxies

Peeples M. S., Werk J. K., Tumlinson J., Oppenheimer B. D., Prochaska J. X., Katz N., Weinberg D. H., 2014, ApJ, 786, 54

Peng Y.-j. et al., 2010, ApJ, 721, 193

Pezzulli G., Fraternali F., 2016, MNRAS, 455, 2308

Pidopryhora Y., Lockman F. J., Shields J. C., 2007, ApJ, 656, 928

Pittard J. M., Parkin E. R., 2016, MNRAS, 457, 4470

Press W. H., Teukolsky S. A., Vetterling W. T., Flannery B. P., 2007, Numerical Recipes 3rd Edition: The Art of Scientific Computing, 3rd edn. Cambridge University Press, New York, NY, USA

Priest E., Forbes T., eds., 2000, Magnetic reconnection : MHD theory and applications

Prochaska J. X., Weiner B., Chen H.-W., Mulchaey J., Cooksey K., 2011, ApJ, 740, 91

Putman M. E., Peek J. E. G., Joung M. R., 2012, ARA&A, 50, 491

Putman M. E., Saul D. R., Mets E., 2011, MNRAS, 418, 1575

Putman M. E., Staveley-Smith L., Freeman K. C., Gibson B. K., Barnes D. G., 2003, ApJ, 586, 170

Reale F., 1995, Computer physics communications, 86, 13

Rechester A. B., Rosenbluth M. N., 1978, Physical Review Letters, 40, 38

Reid M. J. et al., 2009, ApJ, 700, 137

Reynolds R. J., 1991, ApJL, 372, L17

Richter P., Sembach K. R., Wakker B. P., Savage B. D., Tripp T. M., Murphy E. M., Kalberla P. M. W., Jenkins E. B., 2001, ApJ, 559, 318

Rossa J., Dettmar R.-J., 2003, A&A, 406, 505

Saintonge A. et al., 2013, ApJ, 778, 2

Salem M., Besla G., Bryan G., Putman M., van der Marel R. P., Tonnesen S., 2015, ApJ, 815, 77

Sancisi R., Fraternali F., Oosterloo T., van der Hulst T., 2008, A&AR, 15, 189

Saul D. R. et al., 2012, ApJ, 758, 44

Savage B. D. et al., 2003, ApJS, 146, 125

Scannapieco E., Brüggen M., 2015, ApJ, 805, 158

Schawinski K. et al., 2014, MNRAS, 440, 889

Schönrich R., Binney J., 2009, MNRAS, 396, 203

Sembach K. R. et al., 2003, ApJS, 146, 165

Shapiro P. R., Field G. B., 1976, ApJ, 205, 762

Shull J. M., Jones J. R., Danforth C. W., Collins J. A., 2009, ApJ, 699, 754

Shull J. M., Smith B. D., Danforth C. W., 2012, ApJ, 759, 23

Spitzer L., 1956, Physics of Fully Ionized Gases

Spitzer L., 1962, Physics of Fully Ionized Gases

Springel V., 2010, MNRAS, 401, 791

Steiman-Cameron T. Y., Wolfire M., Hollenbach D., 2010, ApJ, 722, 1460

Stinson G. S., Brook C., Macciò A. V., Wadsley J., Quinn T. R., Couchman H. M. P., 2013, MNRAS, 428, 129

Stinson G. S. et al., 2012, MNRAS, 425, 1270

Stone J. M., Gardiner T. A., Teuben P., Hawley J. F., Simon J. B., 2008, ApJS, 178, 137

Strickland D. K., Heckman T. M., 2007, ApJ, 658, 258

Strickland D. K., Heckman T. M., Colbert E. J. M., Hoopes C. G., Weaver K. A., 2004, ApJS, 151, 193

Sutherland R. S., Dopita M. A., 1993, ApJS, 88, 253

Swaters R. A., Sancisi R., van der Hulst J. M., 1997, ApJ, 491, 140

Tamburro D., Rix H.-W., Leroy A. K., Mac Low M.-M., Walter F., Kennicutt R. C., Brinks E., de Blok W. J. G., 2009, AJ, 137, 4424

Thilker D. A., Braun R., Walterbos R. A. M., Corbelli E., Lockman F. J., Murphy E., Maddalena R., 2004, ApJL, 601, L39

Thom C., Peek J. E. G., Putman M. E., Heiles C., Peek K. M. G., Wilhelm R., 2008, ApJ, 684, 364

Thom C. et al., 2012, ApJL, 758, L41

Tollerud E. J., Boylan-Kolchin M., Barton E. J., Bullock J. S., Trinh C. Q., 2011, ApJ, 738, 102

Tumlinson J. et al., 2013, ApJ, 777, 59

Tumlinson J. et al., 2011, Science, 334, 948

van Woerden H., Wakker B. P., Schwarz U. J., de Boer K. S., eds., 2004, Astrophysics and Space Science Library, Vol. 312, High Velocity Clouds

Vieser W., Hensler G., 2007a, A&A, 475, 251

Vieser W., Hensler G., 2007b, A&A, 472, 141

Wakker B. P., 1991, A&A, 250, 499

Wakker B. P., 2001, ApJS, 136, 463

Wakker B. P. et al., 1999, Nature, 402, 388

Wakker B. P., Savage B. D., 2009, ApJS, 182, 378

Wakker B. P., van Woerden H., 1997, ARA&A, 35, 217

Wakker B. P. et al., 2007, ApJL, 670, L113

Werk J. K. et al., 2016, ArXiv e-prints

Werk J. K., Prochaska J. X., Thom C., Tumlinson J., Tripp T. M., O'Meara J. M., Meiring J. D., 2012, ApJS, 198, 3

Werk J. K., Prochaska J. X., Thom C., Tumlinson J., Tripp T. M., O'Meara J. M., Peeples M. S., 2013, ApJS, 204, 17

Werk J. K. et al., 2014, ApJ, 792, 8

Westmeier T., Braun R., Thilker D., 2005, A&A, 436, 101

Westmeier T., Brüns C., Kerp J., 2008, MNRAS, 390, 1691

White S. D. M., Frenk C. S., 1991, ApJ, 379, 52

White S. D. M., Rees M. J., 1978, MNRAS, 183, 341

Zafar T., Péroux C., Popping A., Milliard B., Deharveng J.-M., Frank S., 2013, A&A, 556, A141

Zahid H. J., Dima G. I., Kewley L. J., Erb D. K., Davé R., 2012, ApJ, 757, 54

Zschaechner L. K., Rand R. J., Heald G. H., Gentile G., Kamphuis P., 2011, ApJ, 740, 35

List of Figures and Tables